IN-47-CR
20331
P102

FINAL REPORT FOR NASA GRANT NAG 5-1122

LINEAR AND NONLINEAR ASPECTS OF THE TROPICAL 30-60 DAY OSCILLATION; A MODELING STUDY

March 3, 1989 - February 28, 1991

Duane E. Stevens and Graeme L. Stephens
Prepared for NASA Goddard Space Flight Center

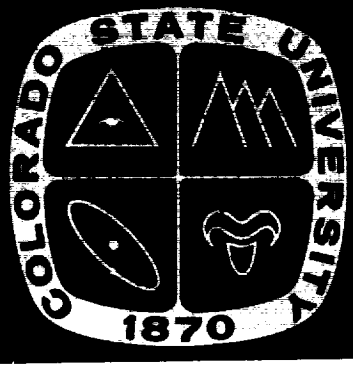

FINAL REPORT

of Research Sponsored Under NASA

NAG 5-1122

By

Duane E. Stevens* and Graeme L. Stephens+

* Department of Meteorology

University of Hawaii at Manoa

Honolulu, HI 96822

(808) 956-8775

+Department of Atmospheric Science

Colorado State University

Ft. Collins, CO 80523

(303) 491-8541

TABLE OF CONTENTS

1. The Scientific Problem

The scientific problem addressed in this research focused on a study of the tropical 30-60 day oscillation and explanations for this phenomenon.

1.1 The importance of low frequency oscillations

The intraseasonal (low-frequency) oscillations with time scales of more than a week have received few dynamical explanations in contrast to midlatitude features on daily weather charts, whose three dimensional structure is well documented by theoretical and observational interpretations. Part of the difficulty is that, in general, low-frequency oscillations, such as the 30-60 day oscillations or the Southern Oscillation, tend to be defined vaguely during some periods or tend to be obscured by the complex interaction of meteorological parameters with different time and space scales. These problems are exacerbated by the relative paucity of reliable observations (and, consequently, reliable analysis as well) in the tropical latitudes.

An important aspect of the variability under consideration is in relation to forcing at climatic changes as characterized by the interannual variability. A possible mechanism that may contribute significantly to such variability is the interaction between the intraseasonal oscillation and the Southern Oscillation (Lau and Chan, 1985). At the same time, the intraseasonal oscillations may be a part of a tropical-extratropical interaction mechanism. Knutson, *et al.* (1986) have noted the occurrence of global modes of oscillations with 30-60 day time scales. The 250 mb zonal winds in the Southern Hemispheres extratropics during Northern Hemisphere summers, were found to be strongly coherent with tropical OLR and zonal winds. This research stems from the belief that analysis of such oscillations and investigation of mechanisms that cause their development will lead to a better understanding of the causes and predictability of climate variability.

1.2 Suggested mechanisms for developing the tropical 30- 60 day oscillation

Theories that have been proposed to explain the intraseasonal oscillation can be divided into two categories. First of these include those theories based on excitation of low-frequency stationary circulations (i.e., nonzonal propagation) in the tropical atmosphere by an internal or external source. The second category includes those theories based on the eastward propagation of Kelvin and/or Rossby waves maintained by convective heating. Neither provides a full explanation to the origin and development of the 30-60 day oscillation and the mechanisms that produce its period.

2. Proposed Research and its Objectives

This research project aimed at studying the linear and nonlinear aspects of the 30-60 day oscillations. It was originally proposed to:

(i) develop and apply linear and nonlinear models of atmospheric circulation; the nonlinear model being a sigma-coordinate primitive equation model including a moisture budget, convective and nonconvective release of latent heat, and radiation processes. The effect of spectral horizontal resolution and the simulation of the diurnal cycles (see (iii) below) on the development of the modeled 30-60 day oscillation will be addressed;

(ii) investigate the nonlinear relationships between zonal asymmetries (especially wavenumber m=1) and the zonally symmetric mode (wavenumber m=0) in producing the energetics necessary for maintaining the oscillation. Such an investigation will also contribute to the possible interrelation between the Walker Circulation and the slow-moving patterns.

(iii) We will compare the model output in terms of simulated OLR and reflected solar radiation (RSR) to observed patterns of OLR and RSR. The observed

fields will be obtained from analysis of ISCCP B1 data (refer to 3.1 below) which will provide information not only on a high spatial resolution but also on the diurnal cycle which is superimposed on the 30-60 day oscillation.

(iv) We will evaluate the role of the Hadley circulation for developing the tropical low-frequency oscillation, which has been discussed by Anderson and Stevens (1987a). It is important that we reexamine the role of the Hadley cell in the linear versions of our relatively more complicated model. The phase and amplitude of the low-frequency oscillation as calculated in the linear case will be analyzed and compared with those calculated using the nonlinear version of the 5-level atmospheric model.

The research was originally proposed for a three year period but only supported for two years. Thus some of these objectives were not reached although the research has contiuned beyond the expiration of this grant.

3. Basic approach to research

The general strategy adopted in this research is to combine analysis of satellite data with model calculations. It was initially proposed to use ISCCP data extensively to diagnose tropical convection and the latent heating associated with this convection. As this research progressed, focus was placed on analysis of microwave data to identify the moisture content of the tropical atmosphere and its variability. It is proposed that the association of these data with cloud imagery provided by ISSCP provides a better relationship between moisture, cloudiness and latent heating. Much of the work during year 1 and year 2 focused on both developing methods for retrieving water vapor and the subsequent analysis of these data. This work has formed the basis of the M. S. thesis of Mr. Darren Jackson.

The modeling approach adopted in this study involved:

(i) Non-linear general circulation model

This model was developed by Dr. Hanna (report attached in appendix) and was a 5-level primitive equation model. The progress through the second year of this research is described in the attached report in Appendix B. The third year of this research would have seen the application of this model to the stated objectives of the research.

(ii) Thermodynamic model of the oscillation

A new and fundamentally different model of the oscillation evolved from the research conducted under this project. This model proposes that an intrinsic thermodynamic oscillation in the coupled ocean-atmosphere system exists that has features reminiscent of the observed 30-60 day oscillation. This model is described briefly below and represents a substantial portion of the Ph. D. thesis of Mr. Qi Hu.

4. Results

4.1 Satellite data analysis and retrieval development

In order to understand the properties of latent heating and factors that govern this heating, research was carried out using satellite measurements of microwave emission from which vertically integrated water vapor is derived. There were two aspects to this research.

(i) Analysis of SMMR water vapor and a study of its relation to sea surface temperature (Stephens, 1990). The results of this analysis are given in the paper attached in the Appendix A. This climatological study served the purpose of providing our understanding of the mean state of the atmosphere and for studying perturbations from this mean state.

(ii) The retrieval of water vapor from SSM/I observations. A new retrieval scheme has been developed (Tjemkes *et al.*, 1991) and analysis of SSM/I water vapor data is continuing. A discussion of the retrieval scheme and its performance is

given in the attached paper (Appendix A).

Several months of SSM/I data have been analyzed in conjunction with both OLR data and ECMWF wind data in an attempt to develop a better understanding between convection and moisture convergence. This analysis forms the bulk of Mr. Jackson's M. Sc. thesis and it is anticipated that this will be completed by the end of the summer of 1991. Fig 1 presents an example of water vapor anomalies and OLR fields, in the form of Houvmuller diagrams, for the period from September 1, 1987 to November 30, 1987 centered about the equator. Positive water vapor anomalies are hatched. Companion diagrams of zonal wind and OLR are also presented for comparison.

4.2 Thermodynamic model of the oscillation

A thermodynamic model of the low-frequency oscillation is proposed. The essential features of this thermodynamic cycle are highlighted in Fig. 2. The essence of the cycle lies in the evaporation of moisture from the warm ocean surface leading to increases in precipitable water and to a destabilization of the atmosphere through heating from below. This leads to an enhanced convective activity and to a decrease in water vapor. With more cloud, evaporation is decreased and the atmosphere stabilized itself leading to a cloud clearing and to a repeat in the cycle. Tests of this idea were conducted by Mr. Hu as part of his ongoing Ph. D. research. Mr. Hu began this research under the guidance of Prof. D. E. Stevens as part of this research project and continues this research under the direction of Prof. D. Randall.

4.3 The 5-level GCM

The model was developed and tested during the first two years of this research project and was to be run to produce a 5-year simulation for the third and final year of this research. A report on this modeling effort is attached.

5. Publications

The following publications list either wholly or partially supported NAG5- 1122.

Stephens, G. L., 1990: On the relationship between water vapor over the oceans and sea surface temperature. *J. Climate,***3,** 634-645.

Tjemkes, S. A., G. L. Stephens and D. L. Jackson: Space Borne Observation of Columnas Water Vapor: SSM/I Observation and Algorithm, *J. Geophys. Res.,* to appear.

Low Frequency Oscillations in Radiative-Convective Models, Q Hu and D. A. Randall, Reprint, 19th Conference on Hurricanes and Tropical Meteorology, May 6-10, 1991.

Stevens, D. E., Q, Hu, G. L. Stephens and D. A. Randall, 1989: The hydrolic cycle of the intraseasonal oscillation. Paper presented at the *Western Pacific International Meeting and Workshop on TOGA-CORE,* Noumea, New Caledonia, May 24-30, 1989.

6. Personnel

Professors G. L. Stephens and D. E. Stevens were supported under this research. Dr. A. Hanna was supported to provide the GCM modeling. Two student's thesis were supported by this grant. This includes the M. Sc. thesis of Mr. D. Jackson and the Ph. D. thesis of Mr. Q. Hu.

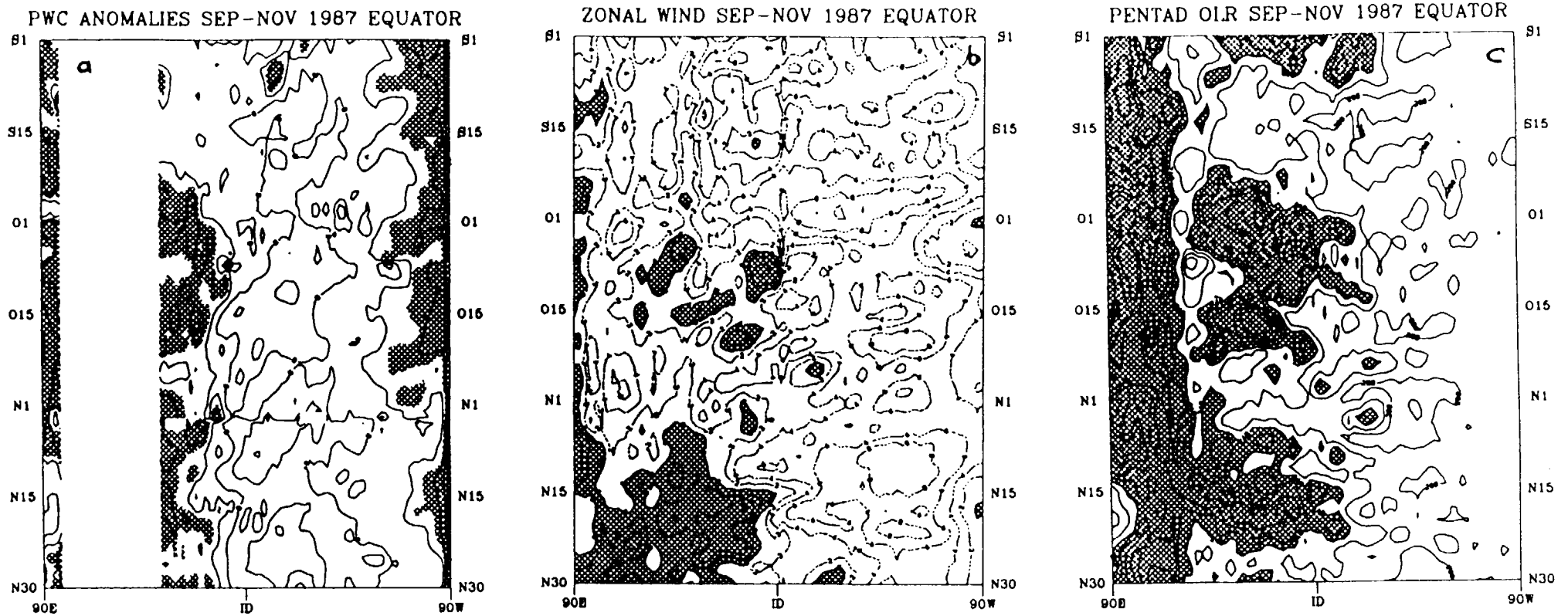

Figure 1: Time-longitude plots of (a) the precipitable water vapor anomalies, (b) the zonal wind and (c) the OLR for the period from 1 September 1987 to 30 November 1987.

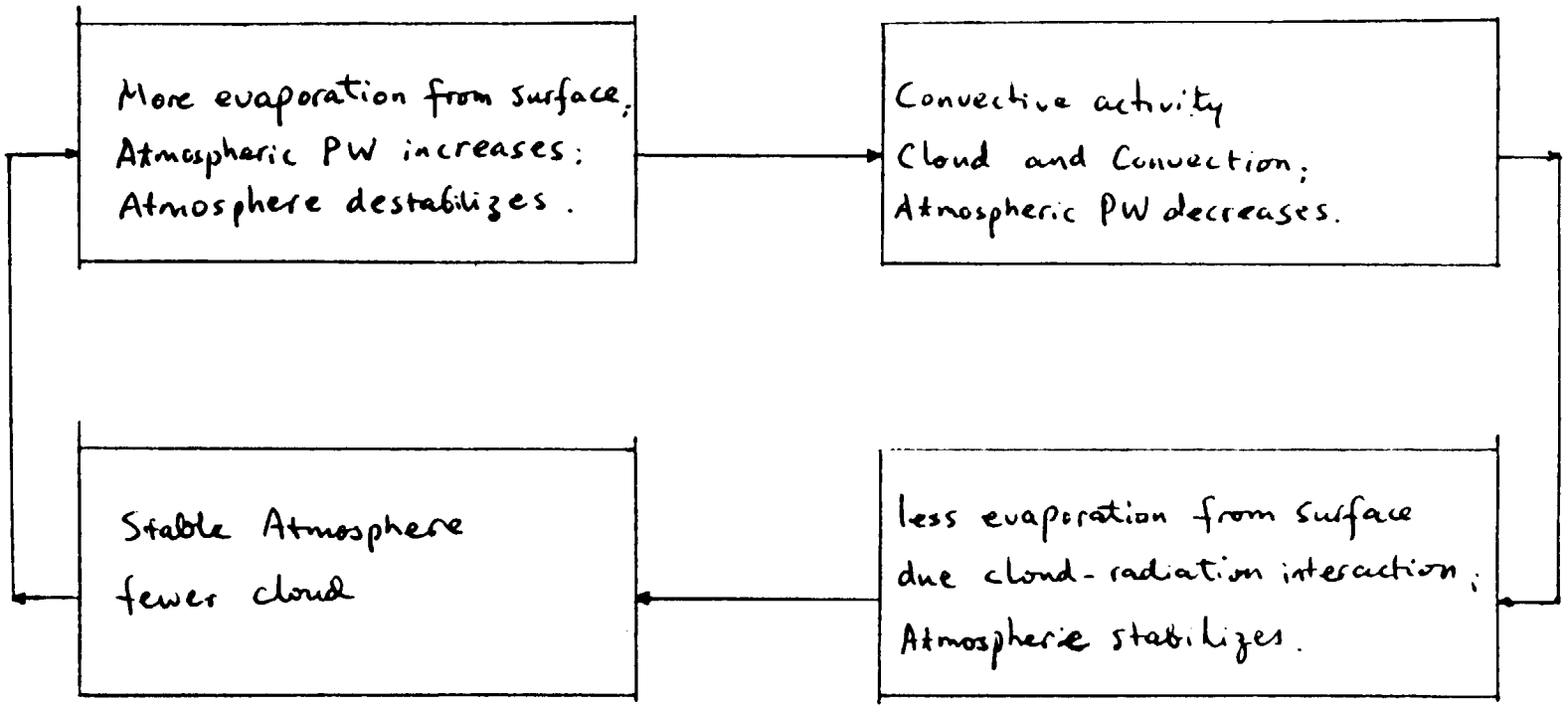

Figure 2: Schematic representation of a hypothetical thermodynamic cycle that is proposed as a possible explanation of the 30-60 day oscillation in the tropics.

APPENDIX A

Reprinted from JOURNAL OF CLIMATE, Vol. 3, No. 6, June 1990
American Meteorological Society

On the Relationship between Water Vapor over the Oceans and Sea Surface Temperature

GRAEME L. STEPHENS

Department of Atmospheric Science, Colorado State University, Fort Collins, Colorado

(Manuscript received 17 July 1989, in final form 30 January 1990)

ABSTRACT

Monthly mean precipitable water data obtained from passive microwave radiometry (SMMR) are correlated with NMC-blended sea surface temperature data. It is shown that the monthly mean water vapor content of the atmosphere above the oceans can generally be prescribed from the sea surface temperature with a standard deviation of 0.36 g cm^{-2}. The form of the relationship between precipitable water and sea surface temperature in the range $T_s > 15$°C also resembles that predicted from simple arguments based on the Clausius–Clapeyron relationship. The annual cycle of the mass of SMMR water vapor integrated over the global oceans is shown to differ from analyses of fully global water vapor data in both phase and amplitude, and these differences point to a significant influence of the continents on water vapor. Regional scale analyses of water vapor demonstrate that monthly averaged water vapor data, when contrasted with the bulk sea surface temperature relationship developed in this study, reflect various known characteristics of the time mean large-scale circulation over the oceans. A water vapor parameter is introduced to highlight the effects of large-scale motion on atmospheric water vapor. Based on the magnitude of this parameter, it is shown that the effects of large-scale flow on precipitable water vapor are regionally dependent, but for the most part, the influence of circulation is generally less than about ±20% of the seasonal mean.

1. Introduction

The role of water in the energy budget of the climate system is a topic of growing interest within the climate research community and has been proposed as the basic theme of GEWEX (the Global Energy and Water Cycle Experiment (GEWEX) is a component of the World Climate Research Program). At present, however, large uncertainties exist in the estimation of the various components of the global water budget and, consequently, in certain important components of the global atmospheric and oceanic energy budgets. We now recognize that the connections between global hydrology and the Earth's energy budget are crucial to the problem of climate change. For instance, the predicted global warming due to a CO_2 doubling with water vapor feedback is approximately twice the warming predicted without feedback (the so-called fixed relative humidity assumption of Manabe and Wetherald 1967). The distribution of water vapor, its transport, and divergence are also essential ingredients to our understanding of the distribution of solid and liquid water in the atmosphere and therefore crucial to the significant and perplexing problem of cloud feedback to climate change (e.g., Paltridge 1980; Somerville and Remer 1984; Roeckner et al. 1987; Stephens et al. 1990, among others).

Corresponding author address: Professor Graeme L. Stephens, Department of Atmospheric Science, Colorado State University, Fort Collins, CO 80523.

Water vapor is also important to other physical processes that occur in the atmosphere. Water vapor plays a decisive role in the transfer of radiation through the atmosphere and is important to the transport and release of latent heat. The distribution of latent heat release is a topic that has received considerable attention over the past decade especially with the burgeoning interest in the variability of the atmosphere on both inter- and intra-seasonal time scales. More specifically, several studies appear in the recent literature on the topic of intraseasonal variability and most focus on the explicit coupling between hydrology and atmospheric dynamics. The results of Gill's (1982) study on moist dynamics, for example, provide insight into the role of moist processes in the physics of low frequency variability. Webster (1983) also noted the importance played by hydrological processes in a modeling study of monsoonal low frequency oscillations. Lau and Peng (1988) developed a self-consistent theory to explain intraseasonal oscillations of the tropical atmosphere in which the effects of latent heating are parameterized directly as a function of the convergence of water vapor. In both that study and that of Gill (1982), explicit relationships between precipitable water vapor and sea surface temperature had to be assumed. Other studies (e.g., Emanuel 1987; Neelin et al. 1987) have also alluded to the importance of evaporation from the warm ocean as a mechanism for sustaining low frequency oscillations of the tropical atmosphere.

These problems underscore the growing need to understand, at the very least, the bulk characteristics of

the distribution of water vapor over the oceans, and in particular, its relationship to sea surface temperature. The importance of water vapor to a variety of atmospheric processes has been recognized for some time (e.g., Starr et al. 1969), but the poor coverage of conventional radiosonde data over the global oceans has both hindered our understanding of the distribution and transport of water vapor and at the same time highlighted the need for satellite-based measurements of water vapor. In response to this need, a number of different satellite approaches have been proposed over the past two decades to measure atmospheric water vapor. For instance, there have been several attempts to estimate water vapor using passive infrared techniques. Shen and Smith (1973) employed satellite infrared spectrometer radiation measurements (SIRS-B) taken from the Nimbus-4 satellite to estimate precipitable water. Retrieval of moisture fields from measurements made with the HIRS instrument on the Nimbus-6 and TIROS-N satellites have been made by Hillger and Vonder Haar (1981) and Hayden et al. (1981). Prabhakara et al. (1979) used the high resolution spectral measurements obtained from the IRIS instrument flown on the Nimbus 4 satellite to study the distribution of precipitable water over the ocean. Perhaps most promising are techniques based on passive microwave remote sensing. For example, studies such as those of Staelin et al. (1976), Chang and Wilheit (1979), Grody et al. (1980), Njoku and Swanson (1984), Prabhakara et al. (1982, 1985), and Wentz (1983) among others have demonstrated the viability of microwave sensing of precipitable water over the world's oceans.

The aim of this study is to examine the relationship between monthly averaged precipitable water and sea surface temperature. The basic idea of relating precipitable water to surface measurements is not new. For example, Reitan (1963), Smith (1966), and Viswanadham (1981) attempted to correlate precipitable water to surface due point temperature with ranging degrees of success. While these studies apply over land, Liu and Niiler (1984) and Liu (1986) considered the correlation of precipitable water to surface mixing ratio over the oceans in an attempt to derive an estimate of monthly mean latent heat flux at the ocean surface. In the present study, precipitable water is correlated to the sea surface temperature. In general, we expect this relationship to be complicated by the influence of both large-scale atmospheric circulation features on precipitable water as well as local processes that influence the relative difference between evaporation from and precipitation to the surface. Unlike the previously mentioned studies, the present study aims to provide some idea of the relative importance of large-scale processes versus local effects on the monthly averaged water vapor over the oceans. The data sources used in this study are described in section 2, and a simple theoretical relationship between precipitable water and sea surface temperature is developed in section 3. Comparisons between the observed relationships and the theoretical relationship are presented in section 4, and departures from the bulk relationship are shown to identify large-scale circulation influences on water vapor.

2. Data sources

The water vapor data used in the analyses described in this paper are derived from the algorithm developed by Prabhakara et al. (1982) based on the measured microwave brightness temperatures at 21 and 18 GHz obtained by the Scanning Multichannel Microwave Radiometer (SMMR) flown on Nimbus-7. An advantage of their retrieval scheme, and one especially relevant to the desired goals of the research described here, lies in the formulation of the retrieval in terms of the difference of brightness temperature between two adjacent frequencies. By differencing these temperatures, the radiometric effects of sea surface emission, and thus any significant sea surface temperature biases in the data, are therefore minimized. Similarly, the effects of cloud water droplets and precipitation on microwave emission and thus on the retrieved water vapor are largely mitigated by using the difference between two adjacent frequencies. In an assessment of their retrieval approach, Prabhakara et al. claim that the integrated water vapor content could be obtained with an rms error of about 0.25 g cm^{-2} based on comparison with radiosonde measurements of water vapor. This quoted error is similar to that estimated by Alishouse (1983) who used a different retrieval approach on SMMR measurements and is also comparable to the estimated error in precipitable water obtained from radiosonde data. The SMMR data used in this study are monthly averages and span a period of approximately five years[1] (January 1979 to September 1983) including the period of the much studied 1982–83 El Niño event. The data are grouped into rectangular areas 3° latitude by 5° longitude over the oceans from 75°N to 75°S. Figure 1 shows the 3 × 5 ocean grid on which the water vapor data are distributed. The data-void blackened areas cover approximately 55% of the total global surface area. Because of the one day on, one day off cycle and occasional missing or bad data, approximately 150 observations per month were obtained for each 3 × 5 grid box. Furthermore, the sun synchronous orbit of the Nimbus 7 provides for only two sets of observations each day that data are taken, and the possibility of a diurnal bias in the data due to an inadequate sampling of the diurnal cycle cannot be ruled out.

The monthly averaged sea surface temperature (SST) data used here are part of the 2.5° global gridded

[1] The reported comparison between radiosonde and retrieved water vapor was carried out systematically throughout the entire period. No appreciable effects of channel drift are evident in these comparisons (Prabhakara, personal communication).

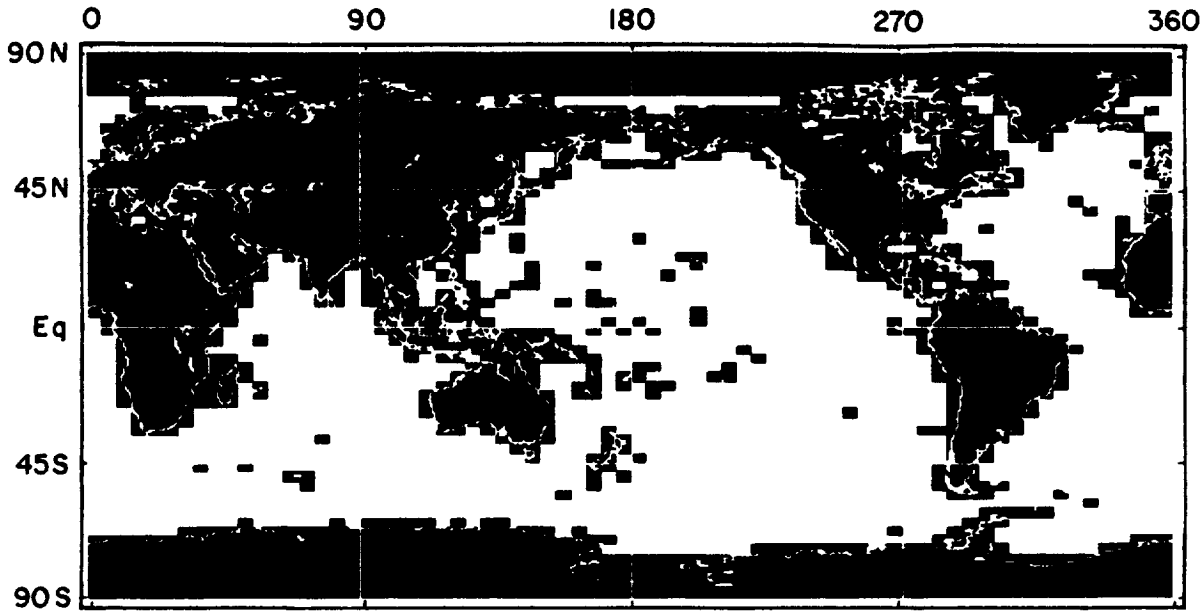

FIG. 1. Map portraying the ocean grid used in the analysis of SMMR water vapor data. The data void areas (blackened) lie over major land masses and islands.

SST dataset produced operationally by the National Meteorological Center (NMC) by "blending" in situ and satellite observations. The in situ data consist of ship and buoy observations, and the satellite observations are obtained using multichannel SST techniques based on the AVHRR observations on the NOAA polar orbiting satellites (e.g., McClain et al. 1985). Because the first available month of these data is May 1979, a total of 52 months of concurrent SST and water vapor data are available for the analyses presented in this paper. A problem of NMC's SST analysis concerns the best way to blend the satellite and ship datasets to maximize the information in each. The method adopted at NMC was to use two days of *in situ* and satellite data to form the blended product. These products were then averaged to produce the monthly mean SST data used in this study. Unfortunately the two-day period chosen for the blending left significant areas of ocean undersampled, and SST information for these areas tended to be weighted towards climatology. As a result, the dataset for the time period that coincides with the SMMR data suffers from a tendency to smooth over SST anomalies (Gemmil, private communication). Recognition of these problems helped prompt NMC to undertake a modified analysis of SST observations by blending data collected over a period longer than 2 days (e.g., Reynolds 1988). Unfortunately, these improved SST data are not available for the SMMR time frame. However, the impact of these limitations on the analyses described below are likely to be relatively small given the interest of this study on climatological relationships between SST and water vapor.

A detailed discussion of water vapor distribution has been provided in earlier studies of Chang et al. (1984) and Prabhakara et al. (1985). The seasonal climatologies of the SMMR water vapor are well described by Prabhakara et al. (1985). The seasonal climatologies of the SMMR water vapor are well described by Prabhakara et al. (1985), and two examples are shown in Figs. 2a and 3a for the periods December to February (DJF) and June to August (JJA) averaged over the three non-El Niño years. The respective climatologies of SST that match these global water vapor distributions are shown in Figs. 2b and 3b. A principal feature to note is the large area of atmospheric moisture greater than 5 g cm^{-2} over the equatorial Indian and western Pacific oceans (shaded area) which roughly corresponds to the pool of water warmer than about 29°C (referred to as the western Pacific warm pool). This is

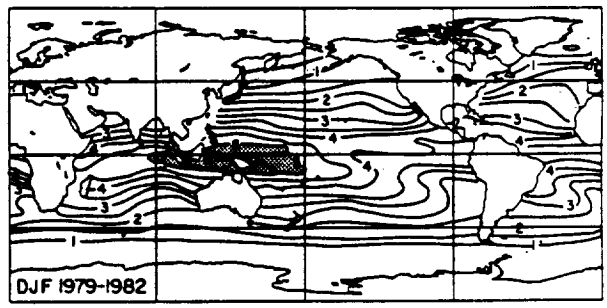

FIG. 2a. The climatological distribution of SMMR precipitable water obtained as an average of the three DJF seasons for the years indicated. Contours have units of g cm^{-2}.

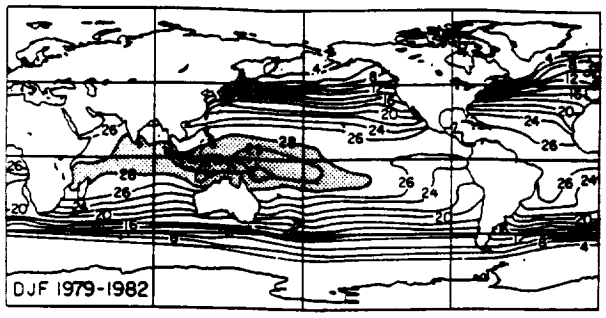

FIG. 2b. The climatological distribution of SST obtained as an average of the same DJF seasons used to obtain Fig. 2a. Contours have units of °C. The warm pool regions exceeding 28°C are highlighted.

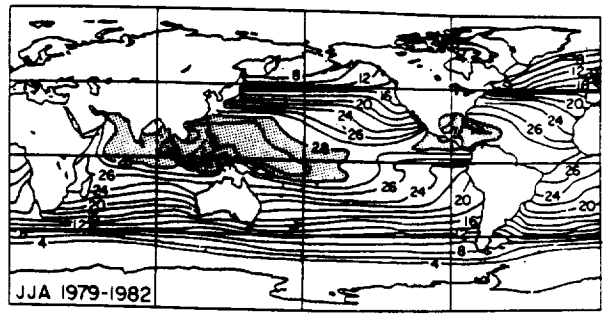

FIG. 3b. As in Fig. 2b but for JJA.

a persistent feature of both seasonal climatologies although the position and size of the moist air varies with season. Also of note are the regions of relatively low water vapor located over the eastern subtropical waters and associated with cold upwelling off the coasts of California, Chile, west Africa, and Angola.

In contrast to these climatologies, water vapor and SST anomalies during May 1983, defined relative to the average of the three May months during the period 1979 to 1981, are shown in Figs. 4a and 4b respectively. A distinct feature of the water vapor anomaly distribution is the large area of positive anomaly (in excess of 1.2 g cm^{-2}) in the equatorial east Pacific associated with a warm SST anomaly in this region. Another obvious feature is the band of dry air across the Pacific that branches out from the equatorial west Pacific eastward and northward into midlatitudes. A less extensive negative anomaly also occurs in the south Pacific off the coast of Chile.

The qualitative comparison of the anomaly fields provided by Figs. 4a and 4b reveals that a number of broadscale features of the water vapor anomaly are related to anomalies in SST. The negative water vapor anomalies just noted more or less match the negative SST anomalies. However, the correlation between water vapor and SST does not always hold. For instance, the area of negative SST anomaly in the equatorial west Pacific is not realized as a negative anomaly in water vapor. Furthermore, the area of positive SST anomaly in the eastern Pacific is less extensive than the positive water vapor anomaly in this region.

3. Analysis procedure

Despite the complicating influences of both dynamics and thermodynamics on water vapor distribution, it is generally believed that its vertical distribution assumes a simple and predictable character. With this in mind, it is proposed that the vertical profile of specific humidity q has the form used previously for example by Smith (1966) and Sellers (1973) among others, namely

$$q = q_o(p/p_o)^{\lambda} \tag{1}$$

where p is pressure and q_o, p_o are the respective surface values. The interpretation of λ is such that the scale height of water vapor is H/λ where H is the atmospheric scale height. If we take 7 km for a typical value of H and 2 km for the water vapor scale height, then a typical value of λ is 3.5.

It follows from the integration of (1) from $p = 0$ to $p = p_o$ that the precipitable water is

$$w = \frac{0.622}{g}\frac{e_o}{1+\lambda}. \tag{2}$$

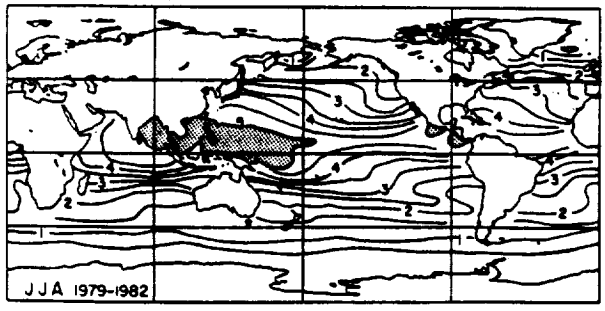

FIG. 3a. As Fig. 2a but for the three JJA seasons of the years indicated.

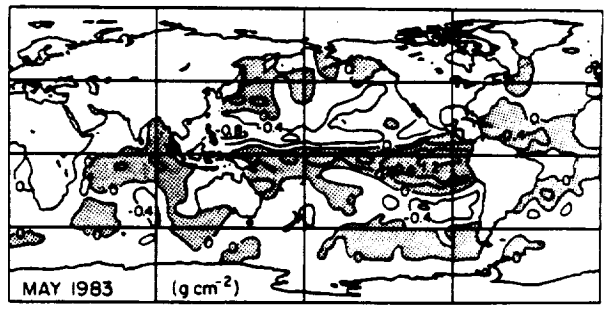

FIG. 4a. The May 1983 precipitable water anomaly distribution (contours have units of g cm^{-2}).

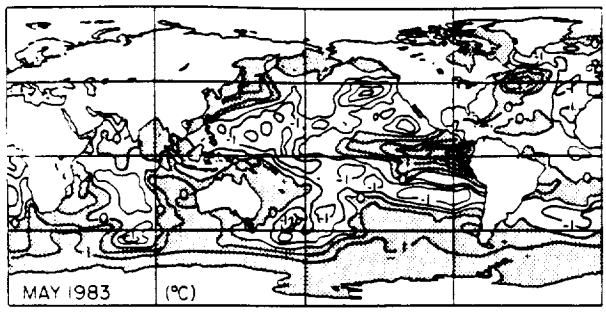

FIG. 4b. The May 1983 SST anomaly field (°C).

where e_o in this expression is the surface vapor pressure

$$e_o = \frac{p_o q_o}{0.622} = r e_o^* \tag{3}$$

and r is the surface value of relative humidity. In (3), e_o^* is the saturation vapor pressure (in mb) which is determined from an approximation to the Clausius–Clapeyron equation of the form

$$e_o^* = 17.044 e^{a(T_s - 288)} \tag{4}$$

where T_s is the SST (Kelvin) and $a \approx 0.064\ \mathrm{K}^{-1}$. From (2), (3), and (4), the relationship between precipitable water w (in g cm^{-2}) and SST then follows as

$$w = 10.82\left(\frac{r}{1+\lambda}\right) e^{a(T_s - 288)} \tag{5}$$

where the factor $r/(1 + \lambda)$ is deduced below by least squares fitting of SMMR derived values of w and the NMC SSTs to (5). The relationship expressed by (5) is provided only as a convenient point of reference for the analysis of the observations described below, and no claim is made that (5) actually represents the observed relationship between w and SST although it is shown that (5) fits the observations well for SSTs in excess of 15°C.

4. Results

a. Global relationships

Figures 5a and 5b provide graphical examples of the relationship between the seasonal means of SMMR derived precipitable water and SST averaged for the five June to August (JJA) seasons and the four December to February (DJF) seasons contained in the 52-month dataset (upper panels). The points represented by open circles are the average of all observations that fall within a 1°C temperature range centered about the given temperature. The extent of the shading above and below each of these average points represents the standard deviation for the data of each bin. Shown in the lower panel are the number of observations contained in the bin which were used to determine both the average and standard deviations. Apparent from both diagrams is the expected but dramatic increase in

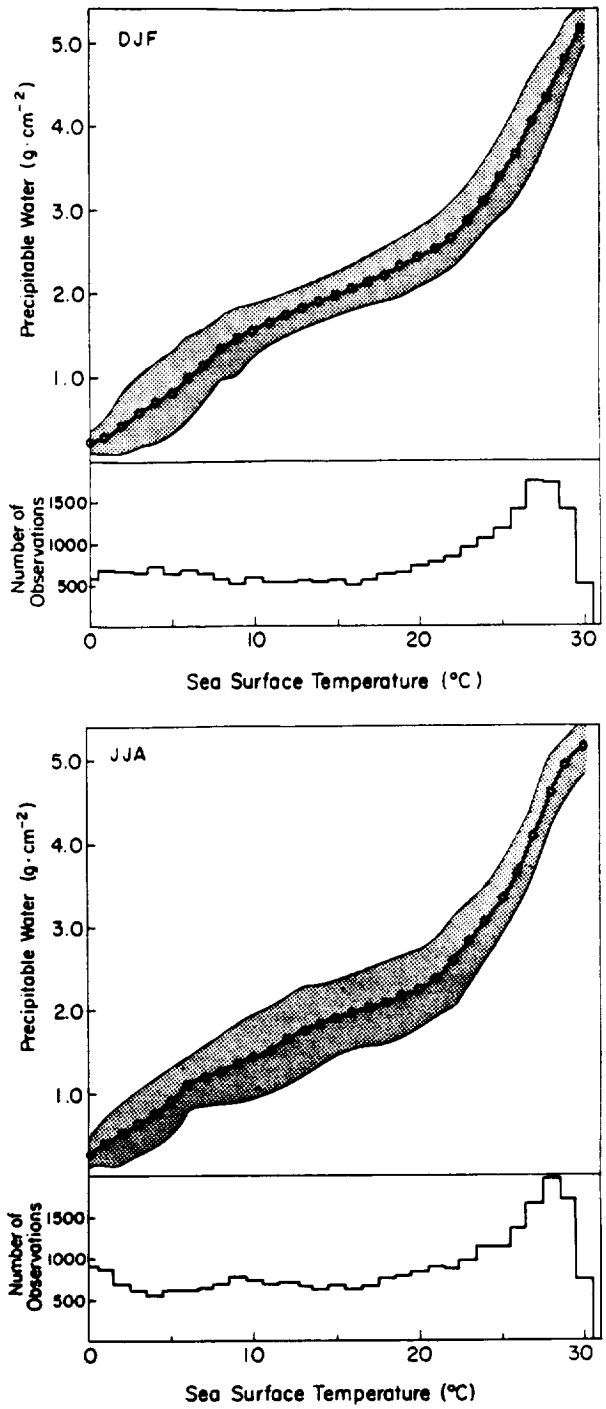

FIG. 5. Graphical representations of the relationship between precipitable water and SST (upper panels) obtained from the composite of all (a) DJF and (b) JJA seasons contained in the dataset. The shading above and below each point is one standard deviation above and below the averaged data point. The number of observations used to form this average and standard deviation are shown as histograms in the lower panel.

atmospheric water vapor as SST is increased above about 20°C. This feature is also apparent in Fig. 6 which shows the annually averaged relationship derived

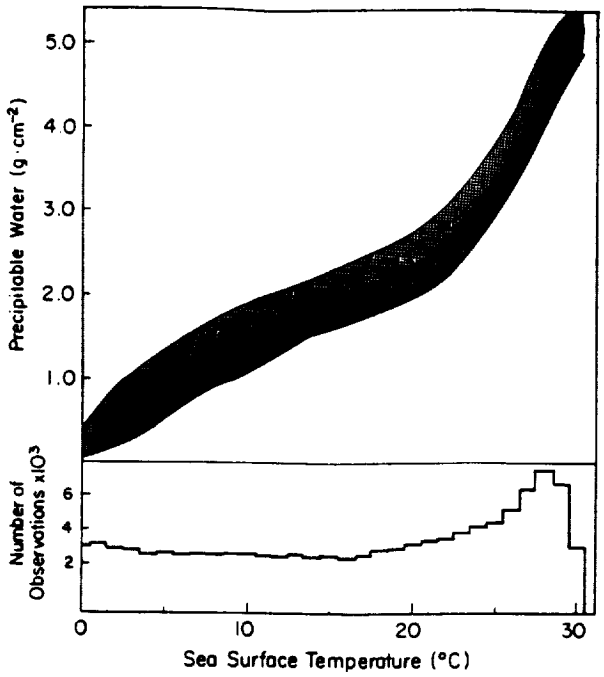

FIG. 6. As in Figs. 5a,b but for the annual mean.

from the composite of all 52 months of data. The standard deviation of precipitable water averaged over the range of SSTs indicated on this diagram is ±0.36 g cm^{-2}. The similarity of both seasons to the annually averaged relationship is further emphasized in Fig. 7. The mean DJF and JJA values are shown on this diagram together with the annual average relationship (solid curve). Also included for comparison are three examples of the relationship expressed by (5) with $r/(1+\lambda) = 0.1$, 0.2, and 0.3. The relationship between w and T_s, especially for $5 < T_s < 15$°C, is shown to differ from the simple expression derived from the Clausius–Clapeyron relationship using a single value of $r/(1+\lambda)$. The apparent increase of water vapor above that predicted from simple theory over this temperature range occurs at those latitudes marked by significant moisture convergence through meridional transports (e.g., Peixoto et al. 1978). However, for temperatures $T_s > 15$°C a value of $r/(1+\lambda) = 0.162$ and $a = 0.0686$ in (5) provides a least squares fit to the data with a standard error of 4.8%.

Figure 8 presents time series of the monthly mean water vapor integrated over the SMMR ocean grid from 75°N to 75°S (upper panel), over the Northern Hemisphere (middle panel), and Southern Hemisphere (lower panel). The quantity represented by the dashed curve is the total integrated water vapor (in kg) or, alternatively, averaged precipitable water (in g cm^{-2}), and the averaged SST is given by the solid curves. The mass of water vapor over the global oceans has a mean of 7.2×10^{15} kg which is 49% of the average mass of water vapor reported by Trenberth et al. (1987). The difference can largely be attributed to the reduced surface area coverage of the SMMR ocean grid compared to the full global data used by Trenberth et al. The annually averaged precipitable water derived from the SMMR data is 2.58 g cm^{-2} which compares well with the values of 2.53 and 2.57 g cm^{-2} reported by Rosen

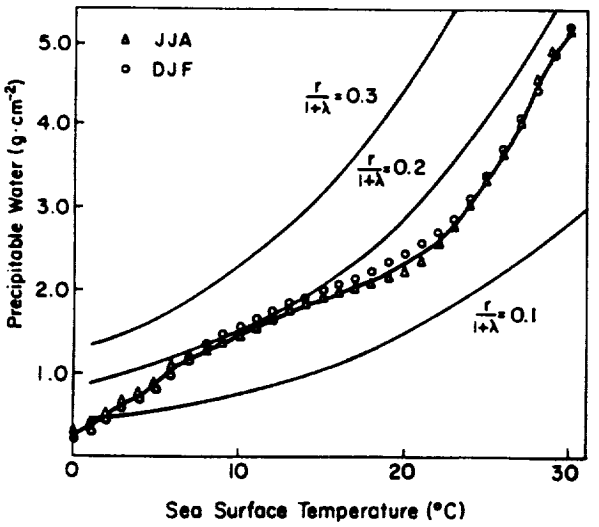

FIG. 7. The annually averaged relationship extracted from Fig. 6 (heavy solid line) compared to the DJF and JJA values from Figs. 5a,b (symbols). Three examples of the Clausius–Clapeyron expression (5) are also shown for the stated values of $r/(1+\lambda)$.

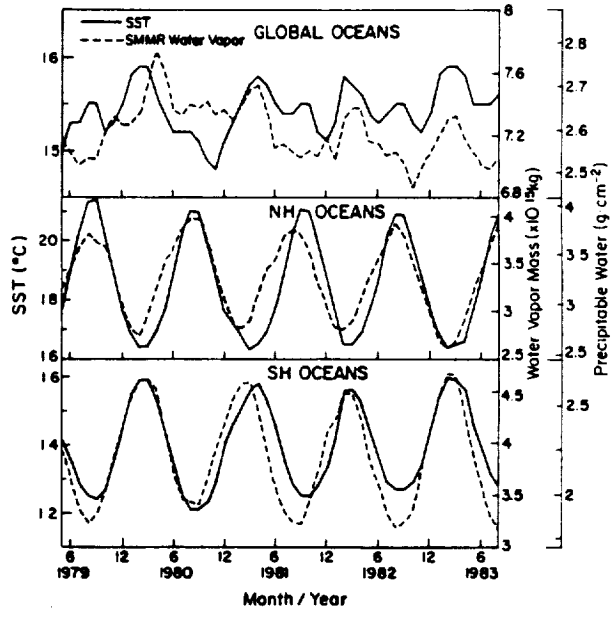

FIG. 8. Time series of SST (solid) and precipitable water (dashed) averaged over the ocean SMMR grid shown in Fig. 1. The upper panel applies to the average over the entire ocean grid, the middle panel to the NH and the lower panel to the SH. The water vapor is also expressed in units of total water vapor mass (kg and righthandmost scale).

et al. (1979) and Peixoto and Oort (1983) respectively but is less than the 2.86 g cm^{-2} quoted by Trenberth et al.[2] although those authors admit to the possibility of a slight high bias in their data.

Whereas the mean SMMR precipitable water reasonably agrees with previously determined amounts, the amplitude of the annual cycles derived over the oceans of each hemisphere disagrees with the hemispheric cycles deduced from global data. The amplitude of the annual cycle deduced from SMMR data is large and approximately 30% of the average value of the precipitable water over the respective oceans of both hemispheres. These cycles largely cancel to produce an annual cycle for water vapor over the global oceans that is significantly smaller in amplitude than for either hemisphere. These results are in direct contrast to those of Trenberth et al. who find an amplitude in both the global and hemispheric averaged water vapor that is approximately twice that shown in Fig. 8. The maximum of global SMMR precipitable water over the oceans peaks around April and is dominated by the annual cycle of water vapor over the southern oceans in contrast to the data of Trenberth et al., who find maxima in the middle of the year in phase with the solar cycle over the Northern Hemisphere. While it is possible to suspect the representativeness of the Trenberth et al. data over the oceans as a cause for these differences, the differences in the annual cycle of water vapor over the oceans compared to that derived over the globe are likely to be real and thus point to a significant influence of the continents on global water vapor.

The sea surface temperatures averaged over the SMMR water vapor grid show the World Ocean to be warmer in April, at the end of the solar heating period, than in October, at the end of the cooling period. This result is consistent with the oceanic temperature records of Levitus (1982) although the amplitude is somewhat more accentuated. The results suggest that the seasonal variation of water vapor over the world oceans reflects the seasonal changes in the global SST.

The SMMR measurements presented in Fig. 8 show a systematic decrease in water vapor over the 52 months analyzed despite the quality checks of Prabhakara which were performed throughout this period at certain fixed locations. It is known that the SMMR antenna temperatures from which the 21 GHz brightness temperatures are derived systematically drifted during this period (e.g., Milman and Wilheit 1985). This instrument drift perhaps explains the low frequency trend apparent in Fig. 8 which is deduced to be about 1% per year for the ocean averaged quantity. The drift, however, is considerably smaller than this on regional scales and generally much smaller than the intra-annual variability (shown in Fig. 10). While the longer term variations shown in Fig. 8 do not invalidate the conclusions drawn from this study, the results highlight the limitations associated with the use of SMMR measurements for studying either long-term variability or for inferring global scale changes of water vapor.

b. *Regional relationships*

While it is shown that the monthly mean water vapor over the oceans is, on the whole, a well-behaved function of SST, important deviations from this general relationship occur on the regional scale. A number of important phenomena might produce regional-scale departures in the gross relationship described above. For example, low-level moisture convergence such as occurs in the vicinity of the ITCZ will produce regions of above average moisture. Also advection of moist air into a relatively dry region can also act to enhance the precipitable water of that region. On the other hand, advection of dry, cold air produces a drier than average atmosphere as do regions of prevailing subsidence, such as within the trade wind regimes where dry air exists above an inversion. Thus significant deviations of precipitable water from that expected from the simple SST relationship reflect these large-scale processes.

To examine these excursions further, time series of water vapor and SST averaged over seven regions were studied. The regions chosen are labeled A through G in Fig. 9 for further reference. Figure 10 presents time series of monthly mean SMMR water vapor (solid curves) and SST (dashed curves) for each region. The comparisons reveal that the annual cycle of water vapor on a regional scale generally correlates with the annual cycle of SST except in the western Pacific (region B). There is also the suggestion that the annual cycle of water vapor in the equatorial and warm water regions (A, B, D, and F) leads the annual cycle of SST in those regions. Of special note is the significant drying that occurs in region B during the first few months of 1983 and the related moistening of the eastern Pacific (region D) during the same period. These deviations from the normal water vapor content occur during the El Niño–Southern Oscillation episode and are consistent with our present understanding of that phenomenon. The deep convection normally located over region B and associated with the ascending branch of the Walker circulation shifts to the eastern Pacific over the anomalous warm water in that region and is replaced by large-scale subsidence (e.g., Webster 1987). This subsidence produces a warming and drying of the middle troposphere above a lower, humid boundary layer thereby indicating a large-scale dynamical influence on atmospheric water vapor.

Figure 11 compares time series of the observed and predicted water vapor for the same seven regions and is presented to emphasize the differences between observed monthly mean water vapor and values predicted from the gross relationship between water vapor and

[2] The value derived from the ECMWF analyses has recently been revised to 2.55 g cm^{-2} (J. Christy, personal communication).

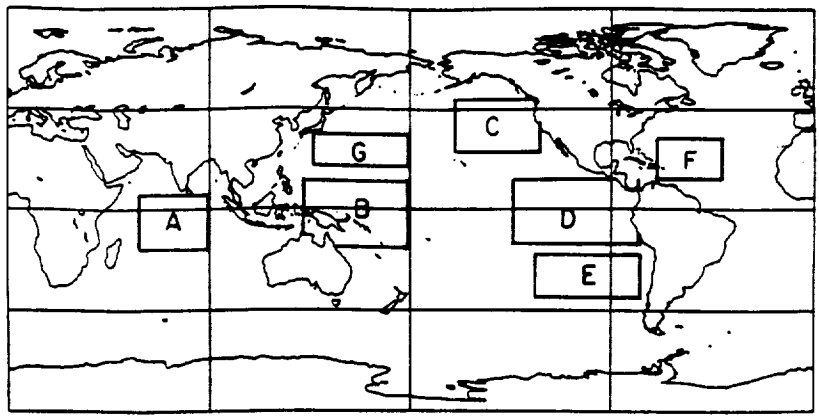

FIG. 9. The location of the seven regions (referenced by A through G) chosen to examine the regional scale relationships between water vapor and SST.

SST derived from Fig. 6. The solid, heavy curve is the time series of monthly mean SMMR observations shown in Fig. 10, and the thin line is the water vapor deduced from interpolation of the data contained in Fig. 6. The extent of the shading about this thin line represents one standard deviation of water vapor above and below this predicted amount and is again determined by interpolation from Fig. 6. The observed water vapor amounts generally fall within this range for the seven selected regions, and the predicted annual cycles of water vapor reasonably match those observed in regions A, F, and G. However, there are notable and important deviations that exist between the observed and predicted water vapor amounts which suggest an influence of large-scale processes. For example, the effects of moisture advection are seen in regions C and D. The systematic difference between the observed and predicted water vapor amounts in the east Pacific region (D) is due to the influence of low level advection of moisture from the Caribbean Sea into the equatorial eastern Pacific. The significant moistening of region C during the boreal summer season can be attributed to eastward advection of moist air that originates from the moister regions of the western Pacific associated with the warm Kuroshio Current and transported eastward along the northern flank of the subtropical high. The observed water vapor amounts in region B also tend to be larger than predicted during the boreal summer season especially during 1980 although this enhancement seems to undergo a marked interannual variability. The moistening of the western Pacific region can be related to the increased moisture convergence associated with the Asian monsoon. Other large-scale influences on water vapor distribution are evident in region E in which the enhanced wintertime drying relates to the large-scale subsidence associated with the accelerating equatorial flow along the eastern flank of the subtropical anticyclones. This explanation is also consistent with the vertical motion analysis of Oort (1983) who shows this subsidence to be strongest during the winter season in this region.

Following the work of Prabhakara et al. (1979), the parameter $(w - \bar{w})/w$ is introduced to highlight the effects of large-scale motion on atmospheric water vapor. In the definition of this parameter, w is the observed precipitable water and $\bar{w}$ is the value estimated given the SST and the relationship graphically portrayed in Fig. 6. Thus, regions influenced by moisture convergence and/or moist air advection are characterized by positive values of this parameter, whereas regions characterized by negative values suggest the influence of subsidence or dry air advection on water vapor. Because water vapor is concentrated in the first few kilometers above the ocean surface, the distribution of $(w - \bar{w})/w$ also indicates, in a gross way, the spatial configuration of the maritime boundary layer (Prabhakara et al. 1979) and the magnitude of this quantity also indicates the quantitative effects of large-scale circulation on precipitable water.

Figures 12a and 12b present the global distribution of $(w - \bar{w})/w$ derived for the DJF and JJA seasons. The values of this quantity, expressed in Figs. 12a and 12b as a percentage, vary from around -60% to $+20\%$ with large areas over the oceans ranging from $\pm 20\%$. Features that appear on these maps reflect various characteristics of the seasonal mean large-scale circulation over the oceans. For instance, the areas of large-scale subsidence associated both with regions of cold upwelling and of large scale subsidence along the eastern branches of the subtropical anticyclonic circulation over the North and South Pacific and Atlantic oceans are indicated by negative values of $(w - \bar{w})/w$. Positive values of this factor are found in the equatorial regions where moisture convergence associated with the ITCZ prevails. Some other outstanding features of these maps are the regions of almost continuous negative values of $(w - \bar{w})/w$ found during JJA in the Southern Hemisphere west of the date line between 20° and 30°S. The location of this region broadly agrees with the vertical motion fields calculated by Oort (1983) and is associated with the descending branch of the Hadley circulation. The relatively moist air over the North Pacific

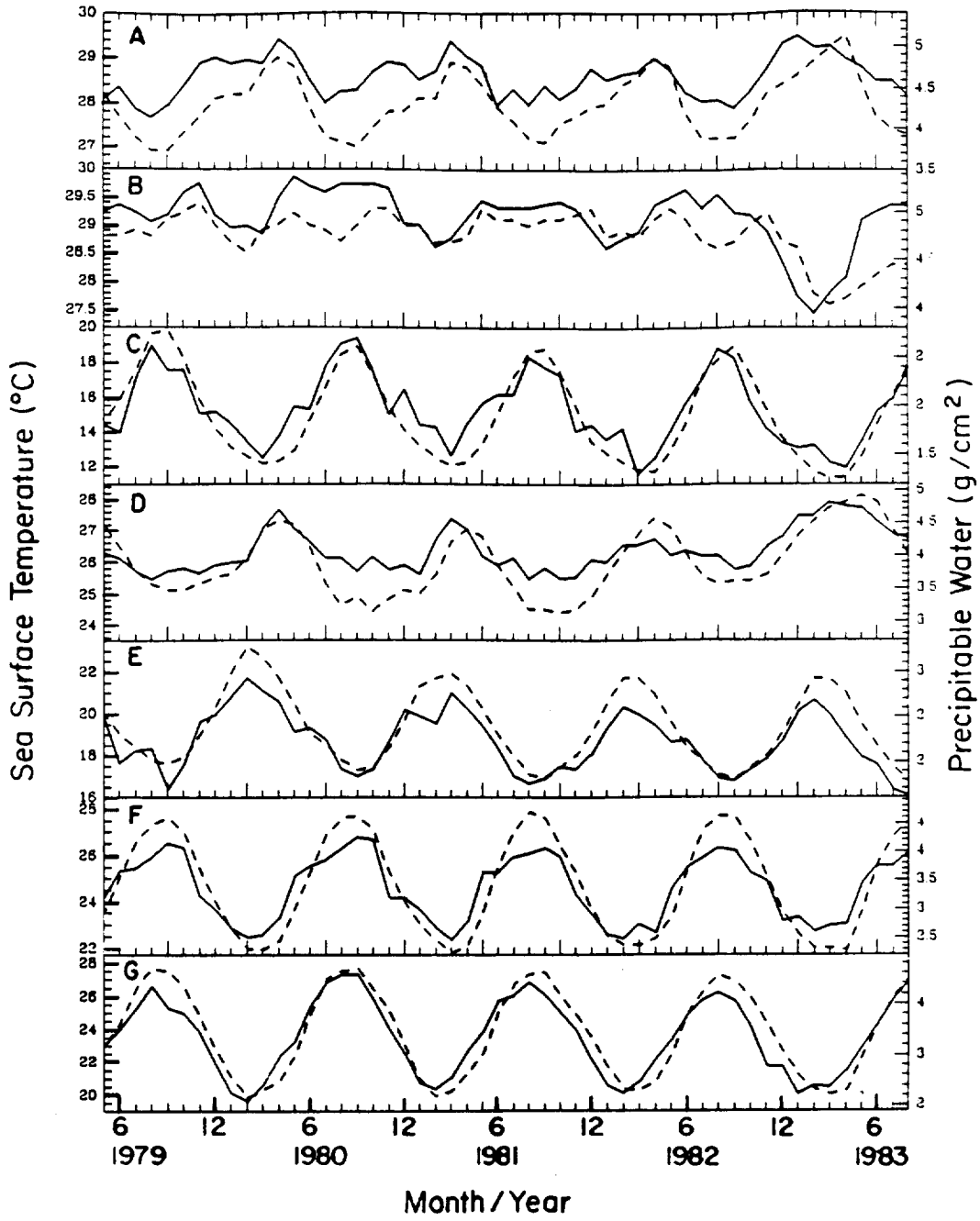

FIG. 10. Time series of SST (dashed) and SMMR precipitable water (solid) averaged over the seven regions highlighted on Fig. 9.

in JJA is also consistent with the large northward flux of moisture by transient eddies, which is thought to occur in this region. A dominant feature of the DJF map is the dry air east of Japan and a similar but weaker dry feature east of the North American continent. These features are respectively associated with the climatological strong high pressure system located in the higher middle latitudes over the cold Eurasian continent and a weaker, less extensive high pressure system over North America. The dry air perhaps results from a combination of strong descent over the eastern portions of these pressure systems which extends eastwards over the Pacific and Atlantic oceans and the advection of dry air from the cold land mass over the warmer waters of these oceans. The existence of these dry areas is also consistent with the large latent and sensible heat releases that are perceived to occur in these regions (Budyko 1982). Both the seasonal and regional variability of $(w - \bar{w})/w$, evident for example off the east coasts of the Asian and North American continents,

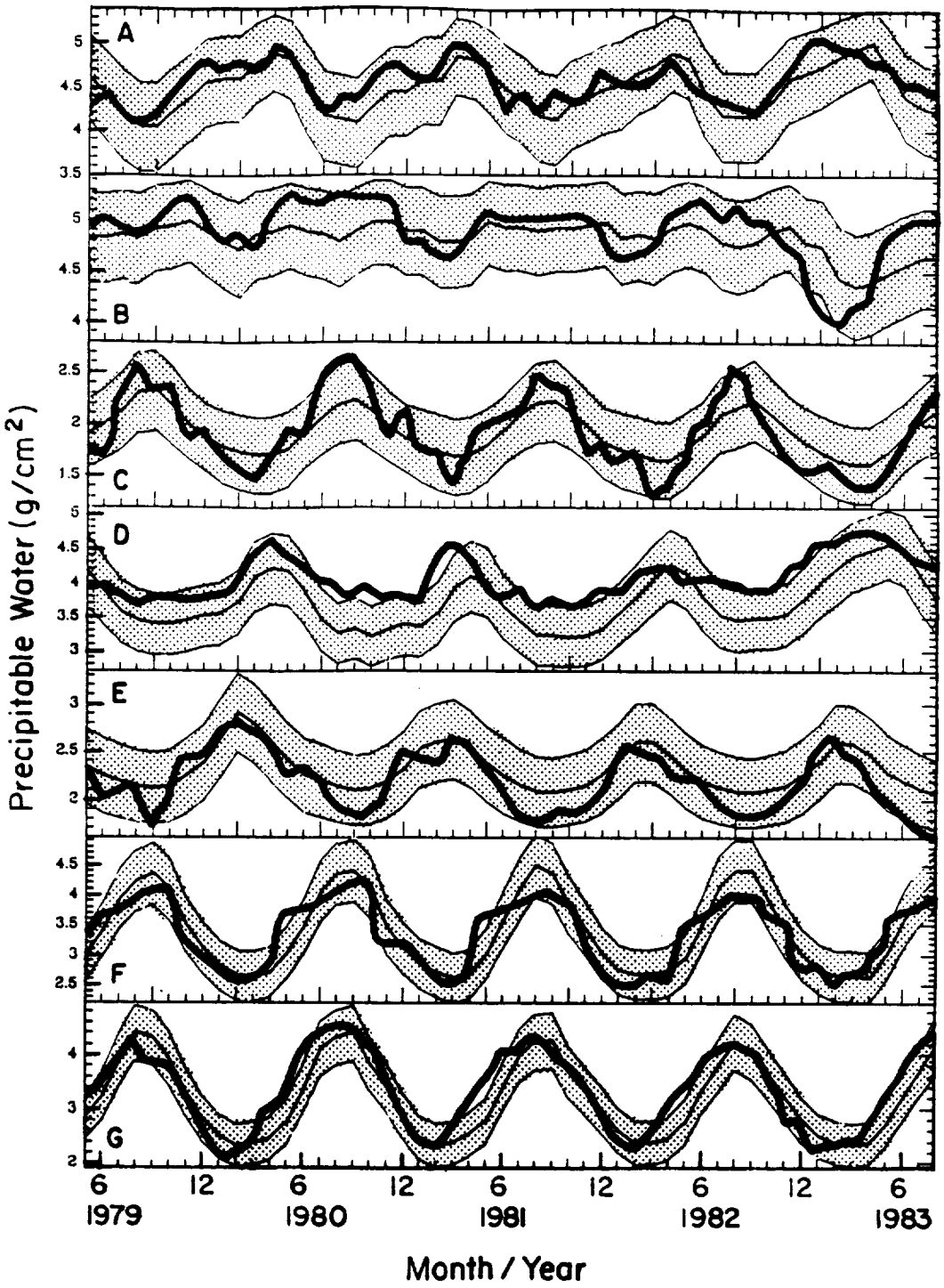

FIG. 11. Time series of SMMR precipitable water (heavy solid) and the precipitable water predicted from the annually averaged relationship presented in Fig. 6 (thin solid line, middle curve) for the seven selected regions. The shading within the two outer thin lines represents the extent of a standard deviation above and below the predicted water vapor.

may perhaps explain why other studies that attempt to correlate precipitable water to surface parameters show varying degrees of success (e.g., Viswanadham 1981).

5. Summary and conclusions

A bulk relationship between monthly mean atmospheric precipitable water and sea surface temperature

was established using 52 months of SMMR microwave water vapor data and monthly averaged NMC blended SST analyses. It was shown that a composite relationship between precipitable water and SST resembled that derived using simple thermodynamical arguments when the sea surface temperature exceeds about 15°C. It was also demonstrated that the annually averaged mass of water vapor integrated over the global oceans deduced from the SMMR observations is in reasonable agreement with certain previous estimates. However, both the phase and amplitude of the annual cycle of water vapor derived from SMMR, when integrated either over the global oceans or individually over the oceans of the Southern or Northern Hemisphere, deviate significantly from some previous findings for the globe as a whole. The study of Trenberth et al. (1987), for example, determined the amplitude of both the global and hemispheric averaged water vapor to be approximately twice that found in the SMMR oceanic data. The maximum in the annual cycle of global SMMR water vapor over the oceans peaks around April and is dominated by the annual cycle over the southern oceans in contrast to the data of Trenberth et al. which yield a maximum in the middle of the year in phase with the solar cycle over the Northern Hemisphere.

Analyses of the SMMR water vapor on a regional scale show that the local departures of observed precipitable water from that predicted from SST could be used as a tracer of large-scale circulation. Regions of large-scale subsidence associated with the mean meridional circulation and with the circulation about the subtropical anticyclones are clearly evident, as are regions of moisture convergence associated with the ITCZ and transient eddy activity in the midlatitudes.

The basic conclusions that can be drawn from this study are as follows:

(i) The monthly mean water vapor content in the atmosphere above the oceans can generally be prescribed from the SST with an averaged standard deviation of 0.36 g cm^{-2}. The form of the relationship between precipitable water and SST in the range T_s > 15°C also resembles that predicted from simple arguments based on the Clausius–Clapeyron relationship. For these temperatures a value of $r/(1 + \lambda) = 0.162$ and $a = 0.0686$ in (5) provides a least squares fit to the data with a standard error of 4.8%.

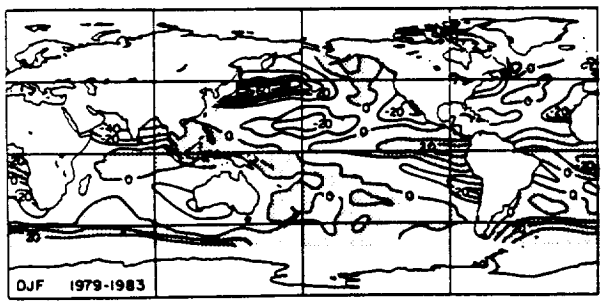

FIG. 12a. The DJF climatological distribution of $(w - \bar{w})/w$ over the SMMR ocean grid. All DJF seasons of the dataset were used in deriving this climatology. Contours are unitless but when multiplied by 100 are the percentage deviation of the predicted water vapor from that observed.

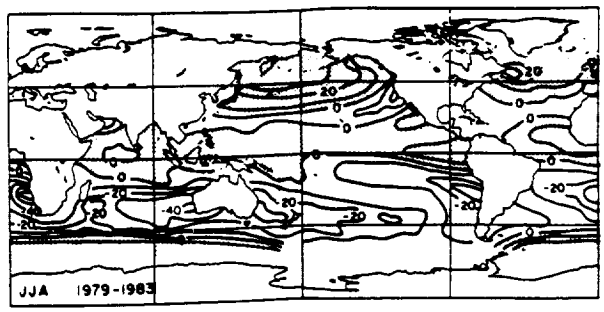

FIG. 12b. As in Fig. 12b but for JJA averaged.

(ii) The annual cycle of the globally integrated mass of water vapor from SMMR over the oceans differs from other analyses in both phase and amplitude. It is possible that these differences are real and perhaps point to ocean–land differences in water vapor with a possible significant influence of the continents on global water vapor.

(iii) Monthly averaged water vapor data (denoted as w), when contrasted with the bulk SST relationship developed in this study (denoted as $\bar{w}$), were shown to reflect various known characteristics of the time mean large-scale circulation over the oceans. The parameter $(w - \bar{w})/w$ was introduced both to highlight the effects of large-scale motion on water vapor and to provide some quantitative measure of these effects on the seasonal mean water vapor. Based on the magnitude of this parameter, it was shown that the effects of large-scale flow on precipitable water vapor over the oceans is regionally dependent but, for the most part, the influence of circulation is generally less than about ±20% of the seasonal mean.

The analyses contained in this paper, both in terms of the bulk relationship between atmospheric water vapor and SST and the relationship between water vapor and the large-scale circulation of the atmosphere, will hopefully provide a useful framework for comparisons between observed water vapor and that predicted by atmospheric general circulation models. For instance, it would be useful in the context of water vapor feedback in climate simulations to compare the correlation between modeled precipitable water and SST with the correlation found in this study. It is further hoped that comparisons of this type might provide insight into the behavior of water vapor in the atmosphere and point to improvements in our ability to model this behavior.

Acknowledgments. I gratefully acknowledge the kindness of C. Prabakhara for supplying me with the SMMR data. I also acknowledge the programming and

graphics work of T. Greenwald. This work was partially supported by NASA Grant NAG 5-1122.

REFERENCES

Alihouse, J. C., 1983: Total precipitable water and rainfall determinations from the SEASAT scanning multichannel microwave radiometer. *J. Geophys. Res.*, **88**, 1929–1935.

Budyko, M. I., 1982: *The Earth's Climate: Past and Future.* Academic Press, 307 pp.

Chang, A. T. C., and T. T. Wilheit, 1979: Remote sensing of atmospheric water vapor, liquid water and wind speed at the ocean surface by passive microwave techniques from Nimbus 5 satellite. *Radio Sci.*, **14**, 793–803.

Emanuel, K. A., 1987: An air–sea interaction model of intraseasonal oscillations in the tropics. *J. Atmos. Sci.*, **44**, 2324–2340.

Gill, A. E., 1982: Studies of moisture effects in simple atmospheric models: Stable case. *Geophys. Astrophys. Fluid Dyn.*, **19**, 119–152.

Grody, N. C., 1976: Remote sensing of atmospheric water content from satellites using microwave radiometry. *IEEE Trans. Antennas. Propag.*, **AP-24**, 155–162.

Hayden, C. M., W. L. Smith and H. M. Woolf, 1981: Determination of moisture from NOAA polar orbiting satellite sounding radiances. *J. Appl. Meteor.*, **20**, 450–466.

Hillger, D. W., and T. H. Vonder Haar, 1981: Retrieval and of high resolution moisture and stability fields from Nimbus 6 HIRS radiances in pre-convective situations. *Mon. Wea. Rev.*, **109**, 1788–1806.

Levitus, S., 1982: Climatological Atlas of the World Oceans. NOAA Prof. Paper No. 13, U.S. Govt. Printing Office, 173 pp. [NTIS PB83-184093]

Liu, W. T., 1986: Statistical relation between monthly mean precipitable water and surface level humidity over global oceans. *Mon. Wea. Rev.*, **114**, 1591–1602.

——, and P. P. Niiler, 1984: Determination of monthly mean humidity in the atmospheric surface layer over oceans from satellite data. *J. Phys. Oceanogr.*, **14**, 1451–1457.

Manabe, S., and R. T. Wetherald, 1967: Thermal equilibrium of the atmosphere with a given distribution of relative humidity. *J. Atmos. Sci.*, **24**, 241–259.

McClain, E. P., W. G. Pichel and C. C. Walton, 1985: Comparative performance of AVHRR-based multichannel sea surface temperature. *J. Geophys. Res.*, **90**, 11 587–11 601.

Milman, A. S., and T. T. Wilheit, 1985: Sea surface temperatures from the scanning multichannel microwave radiometer on Nimbus 7. *J. Geophys. Res.*, **90**, 11631–11641.

Neelin, J. D., I. M. Held and K. H. Cook, 1987: Evaporation-wind feedback and low frequency variability in the tropical atmosphere. *J. Atmos. Sci.*, **44**, 2341–2348.

Njoku, E. G., and L. Swanson, 1983: Global measurements of sea surface temperature, wind speed and atmospheric water content from Satellite Microwave Radiometer. *Mon. Wea. Rev.*, **111**, 1977–1987.

Oort, A. H., 1983: Global Atmospheric Circulation Statistics, 1958–1973. NOAA Prof. Paper No. 14, 180 pp. [NTIS PB84-129717]

Paltridge, G. W., 1980: Cloud-radiation feedback to climate. *Quart. J. Roy. Meter. Soc.*, **106**, 895–899.

Peixoto, J. P., and A. H. Oort, 1983: The atmospheric branch of the hydrological cycle and climate. *Variations in the Global Water Budget*, D. Riedel, 5–65.

——, R. D. Rosen and D. A. Salstein, 1978: Seasonal variability in the Pole to Pole modes of water vapor during IGY. *Arch. Meteor. Geophys. Bioklim.*, Ser. A, **27**, 233–255.

Prabhakara, C., H. D. Chang and A. T. C. Chang, 1982: Remote sensing of precipitable water over the oceans from NIMBUS 7 microwave measurements. *J. Appl. Meteor.*, **21**, 59–68.

——, D. A. Short and B. E. Vollmer, 1985: El Niño and atmospheric water vapor: Observations from Nimbus 7 SMMR. *J. Climate Appl. Meteor.*, **24**, 1311–1324.

——, G. Dalu, R. C. Lo and N. R. Nath, 1979: Remote sensing of seasonal distribution of precipitable water vapor over the oceans and the inference of boundary layer structure. *Mon. Wea. Rev.*, **107**, 1388–1401.

Reitan, G. H., 1963: Surface dew-point and water vapor aloft. *J. Appl. Meteor.*, **2**, 776–779.

Reynolds, R. W., 1988: A real-time global sea surface temperature analysis. *J. Climate*, **1**, 75–86.

Roeckner, E., U. Schlese, J. Biercamp and P. Loewe, 1987: Cloud optical depth feedback and climate modeling. *Nature*, **329**, 138–140.

Rosen, R. D., D. A. Salstein and J. P. Peixoto, 1979: Variability in the annual fields of large-scale atmospheric water vapor transport. *Mon. Wea. Rev.*, **107**, 26–37.

Sellers, W. D., 1973: A new global climatic model. *J. Appl. Meteor.*, **12**, 241–254.

Shen, W. C., and W. L. Smith, 1973: Statistical estimation of precipitable water with SIRS-B water vapor radiation measurements. *Mon. Wea. Rev.*, **101**, 24–32.

Smith, W. L., 1966: Note on the Relationship between total precipitable water and surface dew point. *J. Appl. Meteor.*, **5**, 726–727.

Somerville, R. C., and L. A. Remer, 1984: Cloud optical thickness feedbacks in the CO_2 Climate Problem. *J. Geophys. Res.*, **89**, 9668–9672.

Staelin, D. H., K. F. Kunzi, R. L. Pettyjohn, R. K. L. Poon, R. W. Wilcox and J. W. Waters, 1976: Remote sensing of atmospheric water vapor and liquid water with the NIMBUS 5 microwave spectrometer, *J. Appl. Meteor.*, **15**, 1204–1214.

Starr, V. P., Peixoto, J. P. and R. G. McKean, 1969: Pole-to-pole moisture conditions for the IGY. *Pure Appl. Geophys.*, **75**, 300–331.

Stephens, G. L., P. W. Stackhouse, Jr. and P. J. Flatau, 1990: The relevance of the microphysical and radiative properties of cirrus clouds to climate and climatic feedback. *J. Atmos. Sci.*, in press

Trenberth, K. E., J. R. Christy and J. G. Olsen, 1987: Global atmospheric mass, surface pressure, and water vapor variations *J. Geophys. Res.*, **92**, 14815–14826.

Viswanadham, V., 1981: The relationship between total precipitable water and surface dew point. *J. Appl. Meteor.*, **20**, 3–8.

Webster, P. J., 1983: Mechanisms of monsoon low-frequency variability: Surface hydrological effects. *J. Atmos. Sci.*, **40**, 2110–2124.

——, 1987: The variable and interactive monsoon. *Monsoon*, Fein Stephens, Eds. Wiley and Sons, 269–330.

Wentz, F. J., 1983: A model function for ocean brightness temperatures. *J. Geophys. Res.*, **88**, 1892–1906.

Space Borne Observation Of Columnar Water Vapor: SSM/I Observations And Algorithm

Stephen A. Tjemkes, Graeme L. Stephens and Darren L. Jackson

Department of Atmospheric Science, Colorado State University

Fort Collins, CO. 80523

1.0 Introduction

Since relatively small changes in the mass of water vapor on all scales produce significant changes of cloudiness, an adequate description of water vapor and its variability is essential for understanding the hydrological cycle of the atmosphere and hence the energy balance of the earth's climate system. Water vapor is the predominant greenhouse gas and provides a major positive feedback mechanism that influences a carbon dioxide induced climate warming (Manabe and Wetherald 1967; Ravel and Ramanathan 1989). Despite its fundamental importance, the global distribution and seasonal variability of both water vapor and its transport are largely uncertain and water vapor prediction by climate models, including the strength of the water vapor feedback are untested.

These uncertainties in our understanding are primarily due to the current undersampling of the present day routine observing network which is biased to the large northern hemisphere land masses. This bias underscores the need for a reliable satellite-based approach to the measurement of the global distribution of water vapor. A number of different satellite methods have been proposed over the past decades. For instance, there have been several attempts to estimate water vapor using passive infrared techniques. Shen and Smith (1973) employed satellite infrared spectrometer radiation measurements (SIRS-B) taken from the Nimbus 4 satellite to estimate columnar water vapor. Prabhakara *et al.* (1979) applied the high resolution spectral measurements obtained from the IRIS instrument flown on the Nimbus 4 satellite to the study of the distribution of columnar water vapor over the ocean. Retrieval of moisture fields from measurements made with the HIRS instrument on the Nimbus 6 and TIROS N satellites have also been made by Hillger and Vonder Haar (1981) and Hayden *et al.* (1981) and comparison of water vapor retrieved from operational sounders with more conventional data is described by Gruber and Watkins (1981), Illari (1989) and others.

Perhaps most promising are techniques based on passive microwave remote sensing for

measuring the vertically integrated water vapor amount (the columnar water vapor, CWV). For example, studies such as those of Chang and Wilheit (1979), Njoku and Swanson (1983), Prabhakara *et al.* (1982, 1985), and Wentz (1983) using data collected from the Scanning Multichannel Microwave Radiometer (SMMR) flown on Nimbus 7 have demonstrated the viability of microwave sensing of columnar water vapor over the world's oceans.

The principal aim of this study is to provide a method for the retrieval of CWV based on the microwave observations of the Special Sensor Microwave Imager (SSM/I) which was launched in July 1987 as part of the Defense Military Satellite Program on a sun synchronous satellite. The SSM/I is a passive microwave radiometer which measures the upwelling microwave radiation at four different frequencies 19.35, 22.235, 37.0 and 85.5 GHz. Measurements of both horizontal and vertical polarization are made at 19.35, 37.0 and 85.5 GHz. At 22.235 GHz measurements are made in the vertical polarization state only. Of particular interest to the present study are the observations at 19.35 GHz. At this frequency the instrument has a spatial resolution at the earth surface of 70 x 45 km (3 dB range) and a rms error in the brightness temperature of approximately 0.4 K (at 300 K). A complete description of the instrument is given by Hollinger *et al.* (1987). The SSM/I is planned as an integral part of the DMSP effort was well as NASA's Tropical Rainfall Measurement Mission (TRMM) planned for the 1990's (Simpson *et al.* 1988). Thus the development of retrievals using these measurements are likely to play a key role in establishing future satellite derived water vapor climatologies. Specific advantages of the SSM/I over other microwave instruments, notably the SSMR, are the improved design and better calibration of the radiometer. Futhermore, the higher temporal resolution and the larger swath width of the SSM/I relative to the SMMR makes the SSM/I observations more suitable for short term water vapor variability studies.

In this paper we develop a new water vapor retrieval scheme that is validated against independent radiosonde observations and also compared to existing microwave retrieval methods. One rationale for the development of a new approach concerns the desire to compare different types of retrieval schemes so as to gain some appreciation of the uncertainty associated with the specific retrieval method itself. In this regard, we compare the CWV retrieved by the new scheme to that

obtained from Wentz (1983), Prabhakara *et al.* (1982) and Chang and Wilheit (1979). Another motivation for the development of the scheme presented here concerns the limitations of applying techniques developed for other data sets, specifically for the SMMR, to SSM/I data. These issues are examined in section 2 of the paper in which the basic radiative transfer theory is outlined. It is demonstrated theoretically how a retrieval approach using the 22.235 GHz and the 19.35 GHz channels of the SSM/I leads to ambiguous retrieval estimated of CWV greater the about 40 kgm^{-2}. The radiative transfer description is then followed by an assessment of the accuracy of the approach provided in section 3. Comparison of the method with rawindsonde observations is given in section 4 followed by presentation of water vapor retrieval for a three month period in 1987.

2.0 Microwave radiative transfer through a cloud free atmosphere

a) Detailed radiative transfer model

In the microwave region between 10 - 40 GHz, the absorption and emission of electromagnetic radiation is dominated by water vapor and molecular oxygen. The absorption and emission of microwave radiation by liquid water is also important at these frequencies but is neglected here although it is a subject of further study. Water vapor exhibits a weak spectral line centered at 22.235 GHz and a set of oxygen spectral lines are present at 60 GHz. The upwelling microwave radiation at the top of the atmosphere follows from the solution of the transfer equation for electromagnetic radiation through a cloud free plane parallel atmosphere at a single frequency which is given by (Chandrasekhar 1960)

$$\frac{1}{\kappa(z)\, sec\theta}\frac{dI(z)}{dz} = S(z) - I(z), \tag{1}$$

where I represents the specific intensity ($Wm^{-2}Hz^{-1}sr^{-1}$) and S the source function. The frequency dependence is hereafter understood. All other symbols are defined in Appendix A. The source function S describes the gain of radiative energy due to interaction with atmospheric water vapor and oxygen, whereas the second term in the right hand side of (1) represents the loss of radiative energy. Assuming an atmosphere in local thermodynamical equilibrium (LTE), the source function is given by the Planck function which can readily be approximated by the Rayleigh-Jeans approximation for the range of microwave frequencies considered here. The radiation received by the satellite is expressed in terms of brightness temperature (T_b) and is given by the integral solution of (1) written as

$$T_b^{h,v}(z_t) = T_b^{h,v}(z_0)\,\tau(z_0, z_t) + \int_{z_0}^{z_t} T(z')\frac{d\tau(z', z_t)}{dz'}dz', \tag{2}$$

where τ the total transmission function defined as the product of the transmission due to oxygen (τ_{ox}) and water vapor (τ_{h_2o}),

$$\tau(z_0, z') = \tau_{ox}\tau_{h_2o} = \exp - \int_{z_0}^{z'} (\kappa_{h_2o}\rho_{h_2o} + \kappa_{ox}\rho_{ox})\, dz'. \tag{3}$$

The first term of the rhs of (2) describes the microwave emission for the lower boundary given by

$$T_b^{h,v}(z_0) = T_s e_s^{h,v} + (1 - e_s^{h,v}) \int_{z'}^{z_0} T(z') \frac{d\tau(z_0, z')}{dz'} dz' \tag{4}$$

with e_s the surface emissivity, a function of near surface windspeed, sea surface temperature (SST) and polarization. The second term in (2) describes the contribution from the atmosphere. Given the vertical distribution of water vapor and oxygen, and the frequency dependance of the absorption coefficient, the brightness temperature at the top of the atmosphere is shown to involve three height integrals which we evaluate using the trapezoidal rule. The absorption coefficients of water vapor and oxygen are deducted from the Gross line shape (Waters 1976). The emissivity of a specular sea surface is given by the Fresnel equations (Jackson 1975) using the dielectric constants of Klein and Swift (1977). The changes of the surface emissivity due to surface wind speed are calculated with the empirical model proposed by Pandey and Kakar (1982).

We use this microwave radiative transfer model to study two existing retrieval methods. The first one is that of Prabhakara *et al.* (1982) which exploits the difference between the SMMR measurements at 18 and 21 GHz to retrieve CWV. This method has the advantage that the retrieved CWV is relatively insensitive to the exact value of the surface emissivity (Appendix B). A disadvantage of this method is that for values of CWV > 50 kgm^{-2}, the brightness temperature difference exhibits a saturation with respect to precipitable water. This is shown in Fig. 1 where we present the difference in the 21 and 18 GHz brightness temperatures as a function of CWV calculated with the detailed microwave radiative transfer model using 78 different observed atmospheric temper-

ature and humidity profiles. The results for these calculation are represented by the solid dots. For small values of CWV, the absorption of microwaves at 18 as well as at 21 GHz, depends linearly on CWV, and the brightness temperature difference between the two frequencies is also linear in CWV. For CWV > 50 kgm^{-2} the emission at 18 GHz remains is a linear function of CWV, whereas the emission at 21 GHz is not. As a result, the brightness temperature increases no longer a monotonically with increasing CWV, and the retrieval method of Prabhakara *et al.* becomes ambiguous for CWV > 50 kgm^{-2}. The saturation effect becomes even more pronounced for brightness temperature differences formed using the SSM/I channels one at the center of the weak water vapor line at 22.235 GHz and the second one at an adjacent frequency such as at 19.35 GHz. Calculations of this brightness temperature difference for the 78 observed profiles mentioned above demonstrate that the retrieval of CWV from these measurements using the brightness temperature difference method like that of Prabhakara *et al.* (1982), provides unambiguous results when CWV< 40 kgm^{-2} (Fig. 1).

The second retrieval method published in the litterature is the work of Chang and Wilheit (1979). Their retrieval of atmospheric parameters from passive microwave observations makes use of brightness temperature ratios of the form

$$R = \frac{T^{v}_{22.235} - T_s}{T^{v}_{19.35} - T_s}. \tag{5}$$

This approach of Chang and Wilheit has the same advantage as the method used by Prabhakara *et al.* (1982) since (5) is also insensitive to the actual value of the surface emission (Appendix B). However, it can be shown using the theoretical model that (5) exhibits a similar saturation effect as that shown for the Prabhakara *et al.* scheme. Figure 2 shows R for the SSM/I frequencies as a function of CWV and highlights the reduced sensitivity of R when CWV exceeds 40 kgm^{-2}.

The analyse of both these methods shows clearly the limitations of using the observations at 22.235 GHz for retrieving the CWV especially when CWV > 40 kgm^{-2}. Thus an alternate method is needed to retrieve CWV in the moist tropical atmosphere. We propose here a method based

on the polarization difference at 19.35 GHz. In general $e^h \neq e^v$ and the microwave radiation field at the top of the atmosphere is polarized. The absorption of the radiation by atmospheric water vapor tends to depolarize the radiation field received by the satellite. If the polarization state of the radiation field at the surface is known, the difference between the horizontal and vertical polarization state of the radiation field at the top of the atmosphere provides a measure of the absorption in the atmosphere and thus related to CWV. Figure 3 shows the difference between the brightness temperature in the horizontal and in the vertical polarization state as a function of CWV calculated with our microwave radiative transfer model. This relation exhibit no saturation effect at high CWV as experienced by the previous two methods. However, this new scheme suffers from its own drawbacks such as an increased sensitivity to the surface emission. In order to invert the relation shown in Fig. 3 we developed the simplified microwave radiative transfer model that is now described.

b) Approximate radiative transfer model

The height integrals in (2) and (4) can be evaluated analytically if we assume a specific simple expression for the vertical distributions of temperature and water vapor. Assuming $T(z)= T_s +\gamma z$, the integral of (2) becomes

$$T_b z_t = T_s(1 - (1 - e_s)\tau^2) + \gamma(z^+ + (1 - e_s)z^-\tau), \tag{6}$$

with

$$z^+ = \int_{z_0}^{z_t} z' \frac{\partial}{\partial z'}\tau(z', z_t)\, dz', \tag{7}$$

$$z^- = \int_{z_t}^{z_0} z' \frac{\partial}{\partial z'} \tau (z_0, z')\, dz'. \tag{8}$$

To obtain an estimate of the magnitude of z^+ and z^-, we assume that the transmission due to oxygen is constant, and use a Taylor expansion for the water vapor transmission to obtain

$$z^+ = \tau_{ox} \int_{z_0}^{z_t} z' \kappa_{h_2o} (z')\, \rho (z')\, sec\theta \sum_{n=0}^{\infty} \frac{(-)^n}{n!} \left(\int_{z'}^{z_t} \kappa_{h_2o} (z'')\, \rho (z'')\, dz''\, sec\theta \right)^n dz'. \tag{9}$$

We can simplify (9) by assuming that the water vapor absorption coefficient is independent of pressure and temperature and further that the vertical distribution of water vapor is exponential. Thus (9) becomes

$$z^+ = \sum_{n=0}^{\infty} (-1)^n a_n \int_{z_0}^{z_t} z' \exp\left(\frac{-z'}{z_\rho}\right) \left(\int_{z'}^{z_t} \exp\left(\frac{-z''}{z_\rho}\right) dz'' \right)^n dz',$$

$$= \sum_{n=0}^{\infty} (-)^n a_n z_\rho^n \int_{z_0}^{z_t} z' \exp\left(\frac{-z}{z_\rho}\right) \left(\exp\left(\frac{-z}{z_\rho}\right) - \exp\left(\frac{-z_t}{z_\rho}\right) \right)^n dz', \tag{10}$$

where

$$a_n = \frac{\kappa_{h_2o}^{n+1} \rho_0^{n+1} (sec\theta)^{n+1}}{n!}. \tag{11}$$

Use of the binomial theorem gives

$$z^+ = \sum_{n=0}^{\infty} (-1)^n a_n z_\rho^n \sum_{k=0}^{n} b_n^k \int_{z_0}^{z_t} z' \exp\left(\frac{(-(n-k+1))\, z'}{z_\rho}\right) dz' \tag{12}$$

with

$$b_n^k = (-)^n \binom{n}{k} \exp\left(\frac{-kz_t}{z_\rho}\right).$$

Since n-k+1 > 0 the integral in (12) can be evaluated yielding

$$z^+ = \sum_{n=0}^{\infty} (-)^n a_n \sum_{k=0}^{n} b_n^k \frac{z_\rho^{n+2}}{(n-k+1)^2} \left(1 - \exp\left[\frac{-(n-k+1) z_t}{z_\rho} \right] [1 + (n-k+1) z_t / z_\rho] \right) \quad (13)$$

which can be simplified since $z_\rho / z_t \gg 1$ such that $b_n^0 = 1 \gg b_n^k$ for $\forall (k \geq 1)$. As a result of this simplification,

$$z^+ = \sum_{n=0}^{\infty} z_\rho^{n+2} (-)^n \frac{a_n}{(n+1)^2} \quad (14)$$

Given that $a_0 \gg a_n$ for $n > 1$ which follows from the substitution of a maximum anticipated value for the CWV of 80 kgm^{-2} and an absorption coefficient at 19.35 GHz of approximately 2.5×10^{-3} $m^2 kg^{-1}$, then

$$z^+ \approx \tau_{ox} z_\rho \kappa_{h_2o} \rho_0 z_\rho sec\theta \approx \tau_{ox} z_\rho (1 - \tau_{h_2o}) \quad (15)$$

where we took the first two Taylor expansion terms to approximate the water vapor transmission. A similar expression for z^- can be derived. At a single frequency the multiplicative rule for transmission holds, that is

$$\tau(z_0, z_t) = \tau(z_0, z') \tau(z', z_t)$$

such that $z_t - z_0 = (z_t - z') + (z' - z_0)$ with z' is at some intermediate level. Then z^- can be expressed as

$$z^- = \tau(z_0, z_t) \sum_{n=0}^{\infty} a_n \int_{z_0}^{z_t} z' \exp\left(\frac{-z}{z_\rho}\right) \left(\int_{z'}^{z_t} \exp\left(\frac{-z''}{z_\rho}\right) dz'' \right)^n dz' \quad (16)$$

with a_n given by (11). Using arguments similar to those for z^+, it follows that

$$z^- = \tau \sum_{n=0}^{\infty} z_\rho^{n+2} \frac{a_n}{(n+1)^2}, \quad (17)$$

and after some simplifications,

$$z^{-} \approx \tau z_\rho \kappa_{h_2o} \rho_0 z_\rho \sec\theta \approx \tau z_\rho (1 - \tau_{h_2o}) , \tag{18}$$

at 19.35 GHz. Thus substitution of (15) and (18) into (6) yields the expression for the brightness temperature at the top of the atmosphere at 19.35 GHz as

$$T_b^{h,v}(z_t) = T_s [1 - (1 - e_s^{h,v}) \tau^2] + \gamma z_\rho (1 - \tau_{h_2o}) [\tau_{ox} + (1 - e_s^{h,v}) \tau^2] . \tag{19}$$

The first term on the rhs of (19) describes the contribution of the lower boundary to the radiation field at the top of the atmosphere, whereas the second term describes the atmospheric emission contribution. Equation (19) shows that for a complete transparent atmosphere (τ=1) the brightness temperature observed by the satellite is equal to the surface emission. For a completely opaque atmosphere, τ=0 and the brightness temperature is given by $T_s + \gamma z_\rho \approx T_s$, where we assume that the water vapor is concentrated in the lower parts of the atmosphere and the temperature there is close to the sea surface temperature. This shows that by increasing the CWV of the atmosphere, the shielding of the surface by water vapor represented by the first term on the rhs of (19), is far more important than the increase of the effective emission height, represented by the second term on the rhs of (19).

From these equations it can be seen that for an isothermal atmosphere (γ=0) or for a weakly absorbing atmosphere ($\tau \approx 1$), the second term in the rhs of (6) vanishes and the radiation received by the satellite is given by

$$T_b(z_t) = T_s (1 - (1 - e_s) \tau^2) \tag{20}$$

which is the formula used by both Prabhakara *et al.* (1982) and Chang and Wilheit (1979). However, the atmosphere is not isothermal, and especially in tropical regions, the transmission at 22.235 GHz is not close to unity.

c) Physical retrieval scheme

Let Δ represent the difference between the horizontally and vertically polarized brightness temperature. According to (19), Δ and τ are related through a cubic relation

$$\Delta = T_b^h - T_b^v = \frac{\gamma z_\rho r^v}{\tau_{ox}}\left(1 - \frac{r^h}{r^v}\right)\tau^3 + (T_s - \gamma z_\rho)\, r^v \left(1 - \frac{r^h}{r^v}\right)\tau^2. \tag{21}$$

where $r^{h,v} = 1 - e^{h,v}$. Equation (21) can be solved using standard techniques (cf. Bronshtein and Semendyayev 1979) yielding three different complex solutions for τ from which CWV has to be derived and the physical solution decided on. Rather than proceed in this fashion we choose to simplify this cubic equation in the following way. Let $\hat{T}$ represent the reduced temperature defined by

$$\hat{T} = T_s - \frac{\gamma z_\rho}{\tau_{ox}}(1 - \tau),$$

and replace this reduced temperature with a climatological SST (T_c). Thus (21) transforms into an explicit relation between CWV and Δ, namely

$$\mathrm{CWV} = -\left(log \frac{\sqrt{\Delta / (T_c r^v (1 - r^h/r^v))}}{\tau_{ox}}\right) / (\kappa_{h_2o} sec\theta). \tag{22}$$

We demonstrate below that the theoretical error associated with the simplification of (21) in this way is smaller than approximately 2.0 kgm^{-2}. We considere this acceptable given the benefits of simplicity and computational efficiency.

The ratio r^h / r^v in (22) follows from (19) as

$$F = \frac{T_b^h - \bar{T}}{T_b^v - \bar{T}} \approx \frac{r^h}{r^v}, \tag{23}$$

with

$$\bar{T} = T_s + \frac{\gamma z_\rho}{\tau_{ox}} (1 - \tau) . \tag{24}$$

Wilheit (1979) showed that the sensitivity of F with respect to T_s (i.e. $dF/d\bar{T}$) is relatively weak such that $\bar{T}$ can be readily approximated by T_c. The latter is taken from the sea surface temperature data of Reynolds (1988) archived at the National Center for Atmospheric Research. These data are a blend of *in situ* ship measurements and satellite observations. According to Wilheit (1979) and Wentz (1983), F is related to the near surface windspeed by $F = g_0 + g_1 V$, with g_0 calculated using the Fresnel equations and g_1 taken from the surface emissivity model of Padey and Kakar (1982). This linear relation between F and V provides a way of retrieving the near surface windspeed needed for calculating the surface emissivity.

The final two parameters needed in the estimation of CWV are the water vapor absorption coefficient (κ_{h_2o}) and the transmission function for oxygen (τ_{ox}) at 19.35 GHz. The value of these two parameters were obtained from a regression of the total atmospheric transmission calculated with the more detailed radiative transfer model described in the previous section and the CWV for the 78 observed rawindsonde profiles (Fig. 4). The values used in this study are $4.1533 \times 10^{-3} \times \left(\frac{T_0}{T_c}\right)^{0.47733}$ m^2kg^{-1} and $1.004 \times 10^{-2} \times \left(\frac{T_0}{T_c}\right)^{0.68643}$ m^2kg^{-1} with T_0 equals 300 K for κ_{h_2o} at 19.35 and 22.235 GHz respectively and 0.9807 for τ_{ox} at 19.35 GHz.

3.0 Error analysis and sensitivity study

In general, the CWV retrieved by such an algorithm is a function of T_s and the near surface wind velocity (V). The variation of the CWV with respect to SST (i.e. $dCWV / dT_s$) can be written as

$$\frac{dCWV}{dT_s} = \left(\frac{d\Delta}{dCWV}\right)^{-1} \frac{d\Delta}{dT_s}, \tag{25}$$

while dCWV / dV follows from

$$\frac{dCWV}{dV} = \left(\frac{dT_b^v}{dCWV}\right)^{-1} \frac{dT_b^v}{dT_s}. \tag{26}$$

The sensitivity of the brightness temperature at the top of the atmosphere with respect to uncertainties in T_s ($dT_b / dSST$), CWV ($dT_b / dCWV$) and with respect to uncertainties in V (dT_b / dV) were estimated from calculations using the detailed microwave radiative transfer model described in section 2. The calculations were made for the three standard atmospheres of McClatchey *et al.* (1972) with V equals 10 ms^{-1}. The results included in Table 1 list values of $dCWV / dT_s$ between -0.469 and -0.014 $kgm^{-2}K^{-1}$ which corresponds to the results reported by Prabhakara *et al.* (1983). This low sensitivity means that the error in CWV will vary between -2.0 and -0.05 kgm^{-2} (an approximate 3% effect) when the difference between the reduced temperature and the climatological T_s is about 4 K.

The sensitivity of the retrieved CWV with respect to the near surface wind speed is given in Table 1 as 0.5 $kgm^{-3}s$. Thus the retrieved CWV is also insensitive to the actual value of V and only a rough estimate of V within 4 ms^{-1} is sufficient to calculate CWV within 2.0 kgm^{-2}. This estimate is provided from the linear relation between F and V proposed by Wilheit (1979) and Wentz (1983) discussed in the previous section.

To study the error in the retrieved CWV due to uncertainties in the brightness temperature

measurements, some additional calculations were performed using the 78 rawind profiles mentioned before. For this sample of observations the radiometric sensitivity with respect to CWV

$$RS_{cwv} = \frac{d}{dCWV}(T_b^h - T_b^v) / (T_s r^v (1 - r^h/r^v)) \tag{27}$$

$$\approx \frac{1}{T_s r^v (1 - r^h/r^v)} \frac{\Delta (T_b^h - T_b^v)}{\Delta CWV} \tag{28}$$

is evaluated as a function of the CWV. A threshold value of 0.004 m^2kg^{-1} for RS_{CWV} derives from $\Delta CWV \approx 1$ kgm^{-2}, $\Delta (T_b^h - T_b^v) \approx 0.4K$ (cf. section 2) and a typical value of 100 K for $T_s r^v (1 - r^h/r^v)$. The importance of this threshold value becomes clear if we look at a RS_{CWV} at a particular value of CWV. If this RS_{CWV} exceeds the threshold, the resolution in the retrieved CWV is better than 1 kgm^{-2} whereas if RS_{CWV} is smaller than the threshold, the resolution of the retrieved CWV will be lower than 1 kgm^{-2}.

The sensitivity of the Chang and Wilheit retrieval method in this study adapted to SSM/I channels is

$$RS_{CWV}^{cw} = \frac{d}{dCWV}((T_{22.235}^v - T_s) / (T_{19.35}^v - T_s)) \tag{29}$$

whereas the sensitivity of the adapted Prabhakara *et al.* scheme is

$$RS_{CWV}^{cp} = \frac{d}{dCWV}((T_{22.235}^v - T_{19.35}^v) / (T_s \bar{r})) . \tag{30}$$

We normalize these sensitivities according to

$$\| RS_{CWV} \| = \frac{RS_{CWV} - Thres}{Max - Thres}, \tag{31}$$

where *max* and *Thres* refers to the maximum RS_{CWV} value and the threshold for the particular retrieval scheme under consideration (these values are listed in Table 2). Figure 5 shows the normal-

ized sensitivities as a function of CWV for the 78 observed profiles mentioned above. For all three methods, the normalized RS_{CWV} decreases with increasing CWV. This means that all methods are most sensitive at low CWV values and least sensitive at high CWV values. For the present retrieval scheme the decrease in sensitivity for high CWV values is less than for the other two schemes as expected. Because the methods proposed by both Chang and Wilheit and Prabhakara *et al.* use the observations from the same pair of channels, the normalized RS_{CWV} 's change sign around 40 kgm^{-2}. For these two schemes, CWV values up to 40 kgm^{-2} have uncertainties less than 1 kgm^{-1} due to uncertainties in the brightness temperatures and greater than 1 kgm^{-2} for CWV values in excess of 40 kgm^{-2}. For a realistic range of values of CWV, the normalized RS_{CWV} for the present retrieval scheme is always positive and thus has an uncertainty less than 1 kgm^{-2} for uncertainties of 0.4 K in the measured brightness temperature.

The error in the retrieval which we can associate with liquid water contamination is however more severe than the other errors mentioned above. In the present retrieval scheme no distinction between liquid or precipitable water is made. Model calculations of Prabhakara *et al.* (1983) show that the error in the CWV due to a cloud with a typical water content of 0.25 kgm^{-2} may be as large as 5 kgm^{-2}. The retrieval of liquid content, in addition to CWV, is therefore required to avoid this larger error in the CWV. This is a topic of future research but is to be expected that liquid water contamination will only be a source of error in the instantaneous retrieved CWV. When averaged over a long period (e.g a month), the error in the CWV associated with this cloud contamination is likely to be small except in areas of persistent thick clouds where it will introduce a bias in the CWV distribution.

4.0 Results

a) Comparison with rawsindsonde observations

The retrieval scheme described in the previous section is applied to the SSM/I observations of a three month period beginning September 1987. Before discussing the results, we provide a comparison between CWV's retrieved from SSM/I observations and those derived from rawindsonde observations.

For this comparison only those rawindsonde observations which occurred within a 1^{o} radius and within the same day of the SSM/I observation were extracted from the NCAR meteorological archive. Only rawindsonde observations over the global oceans were used and a simple quality control was applied to each of the rawindsonde profile. In total, 1139 observations different than the 78 profiles mentioned above, were used.

Figure 6 shows the scatter diagram of CWV retrieved from the SSM/I and derived from the rawindsonde ascents. In general the correlation between the two independent values of CWV is good, with a rms difference is 6.42 kgm^{-2} (Table (3)). This rms difference consists of two parts, one which describes the systematic difference, the other the unsystematic (Wilmott 1982). The systematic rms represents the bias and could be removed if the appropriate model parameters were chosen properly, the Unsystematic rms represents the spread around the linear relation between the two datasets. From a linear regression analysis the value for the systematic rms is 4.56 kgm^{-2} while for the unsystematic rms it is 4.51 kgm^{-2}. The value for the rms is somewhat larger than reported for previous microwave CWV retrieval methods (e.g. Prabhakara *et al.* 1982; Chang and Wilheit 1979) probably in part due to bad rawindsonde measurements, due to the erroneous interpretation of cloud liquid water as CWV, due to the low sensitivity of the present retrieval method to changes in CWV in the dry atmosphere and due to errors in the modeling of the surface emission (e.g. SSM/I retrievals over land, errors in the surface wind speed retrieval). Test retrievals with the cubic re-

lation (21) showed that the simplification of that relation produces no significant errors in the CWV retrieval.

The uncertainties in the surface emission are related to errors in the retrieval of the surface wind speed and to errors in the surface emission model. As mentioned above, the constants used in the near surface windspeed retrieval are based on calculations performed by the surface emissivity model proposed by Pandey and Kakar (1982) and there is some doubt about the constant used in the relationship between $T^{h,v}$ and V. In particular, the value of the slope here is -8.159 $10^{-3}sm^{-1}$ (at 291 K) which deviated from the value of -9.310 10^{-3} (at 291 K) reported by Wilheit (1979). A comparison between the retrieved wind speed and independent observation is therefore needed in order to retune these parameters. However, the retrieved CWV is only weakly dependent on the retrieved near surface wind speed and such tuning is likely only to alter this rms error slightly. Such comparisons were considered beyond the scope of the present paper. Uncertainties in the surface emission model itself are probably more severe. Unfortunately there are not enough accurate observations to improve the model.

From the quantitative measures listed in Table (3), we notice that the present retrieval method systematically overestimates the CWV for CWV < 20 kgm^{-2}. This overestimation is probably due to the exclusive use of the 19.35 GHz which results in a low sensitivity of the present retrieval method to changes in the CWV in the dry atmosphere. The low sensitivity could be overcome by using observations at 22.235 GHz, where the water vapor absorption coefficient is large The results of a similar comparison for the adopted Chang and Wilheit applied to the SSM/I observations at 19.35 and 22.235 GHz are shown in Fig 7 and Table 3. Apparently this particular scheme correlates much better with the rawindsonde observations below 35 kgm^{-2} than the present method. Since this method is independent of the actual surface emission (cf. Appendix B) the better correlations suggests that the large scatter shown in Fig. 6 is probably due to uncertainties in the surface emission. The bias at the low end of the diagram shown in Fig. 6 is removed, but the Chang and Wilheit method is unable to retrieve CWV in the moist atmosphere. This is in agreement with the results presented in section 2. No retrievals are performed with the Prabhakara *et al.* method because of the

significant ambiguity in their method adapted to the SSM/I frequencies at large values of the CWV (cf. Fig. 1)

b) Horizontal distribution of CWV for September October November 1987

Daily CWV maps were obtained after gridding the retrieved CWV for each observation into 1^{o}x 1^{o} latitude - longitude grid boxes. These daily maps were then averaged to obtain the season mean distribution and its standard deviation as shown in Fig 8. As noted by Stephens (1990), the seasonal mean distribution of CWV also largely resembles the seasonal mean SST distribution (not shown). For instance the tongue of low CWV just south of the equator in the East Pacific matches the tongue of relatively low SST in that region and the extension of the high CWV region in the Western equatorial Pacific is also visible in the seasonal mean SST distribution. This agrees with the previously reported results of Prabhakara *et al.* (1982) and Chang *et al.* (1984). The notable exception is the region of high CWV in the North-Eastern part of the Pacific. This particular region is associated with the anticyclonic air motion around a persistent zone of high pressure off the coast of Oregon transferring moisture from low-into the mid-latitudes.

The storm tracks in the northern Alantic show more clearly in the map of standard deviation than in the CWV map itself. (Fig 8 lower panel). The standard deviation map highlights regions of high temporal variability, such as found in the storm tracks in the mid-latitude, and within the intertropical convection zone (ITCZ) and the South Pacific convection zone (SPCZ). It is to be expected that these regions of high temporal variation are also regions of large horizontal water vapor transfer means of transient eddies and the variance maps shown in the lower panel of Fig. 8 perhaps provide an indication of where these transports are greatest.

When integrated over the ocean grid adopted in this study (approximately 62.7% of the total earth surface), an average of 27.63 kgm^{-2} (8.86 10^{15} kg) of columnar water vapor is retrieved. For the analysed season, most of this precipitable water can be found in the Northern Hemisphere

where the SST is somewhat higher than in the Southern Hemisphere. In total 29.71 kgm^{-2} (4.39 10^{15} kg) is found over the Northern hemisphere oceans compared to 25.84 kgm^{-2} (4.47 10^{15} kg) over the Southern Hemisphere oceans. These values correspond well with the values of 7.2 10^{15} kg reported by Stephens (1990) as derived from SMMR observations over a smaller area, but is larger than the global mean values of 25.3 kgm^{-2} (12.9 10^{15} kg) and 25.7 kgm^{-2} (13.1 10^{15} kg) reported by Rosen *et al.* (1979) and by Peixoto and Oort (1983) respectively derived from rawindsonde observations. This difference may be due to lower CWV's over land areas as suggested in Stephens (1990).

The monthly mean distribution of CWV and SST are highly correlated as already mentioned. To study the relation between the SST and CWV in more detail, the SST's derived from the Reynolds dataset were correlated with the CWV derived from the SSM/I observations for September 1987 in a manner developed by Stephens (1990). The results of such a correlation are compared to that obtained by Stephens (1990) for SMMR observations and are shown in Fig. 9. Apparently, the CWV SST correlation for the present dataset does not differ significantly from the results reported by Stephens. Both relations show an increasing CWV with increasing SST as expected. For low values of SST, the CWV of the SSM/I appears about 10 kgm^{-2} higher than the SMMR CWV values in agreement with the results found from the comparison with rawindsonde observations. For intermediate and high SST values the difference between the two relation is small. Some of this difference can probably be attributed to the limited size of the present dataset. While the SMMR relation is derived from 52 months of observations, the present dataset covers only three months.

b. Intercomparison with other microwave retrievals

The horizontal distribution of columnar water vapor derived from SSM/I observations using the adopted Chang and Wilheit scheme for the analysed season is presented in Fig. 10. This

diagram exhibits the same general features shown in Fig. 8, although the CWV's retrieved in the tropical regionsare significantly lower than those shown in Fig. 8. This underestimation is also clear from the SST-CWV correlation as shown in Fig. 9. Integrated, over the global oceans with the adapted Chang and Wilheit method retrieves an average of 23.22 kgm^{-2} (7.45 10^{15} kg) from these SSM/I observations, which is significant smaller than the values reported above.

In the present retrieval scheme, LWC is erroneously interpreted as CWV, hence it is anticipated that the CWV values derived from the SSM/I observations using the present retrieval scheme might be too high in certain locations. This is likely to be true for instantaneous retrievals of CWV, but not for the monthly and seasonal mean values, since it is likely that only persistently thick clouds contribute significantly to this bias. This conclusion is supported from the comparison with the monthly mean CWV derived from the SSM/I observations using a method described by Wentz (1983). The Wentz method uses a closed form of the transfer equation, similar to our simplified microwave radiative transfer model described in section 2, to calculate the microwave radiation received by the satellite. The CWV of the atmosphere follows from an iterative technique that matches the calculated radiation field to the observed field. Errors in the Wentz values of CWV due to LWC contamination should be significantly reduced since LWC is also retrieved from the SSM/I observations. Moreover, the CWV for regions with moderated or heavy rain are excluded in the Wentz retrieval.

The results of this method for September 1987 is correlated with the sea surface temperature for that period and compared to the SST-CWV correlation derived from SSM/I observations for the same period using the present method. The results of this comparison are presented in Fig. 11. In the tropical regions, the CWV values in the Wentz data are higher than the present estimates. This difference directly contrasts what would be expected from significant LWC contamination in the present scheme. Whether these differences in performance are due to our scheme or to inaccuracies in the Wentz retrieval algorithm is not clear. It appears that the Wentz method retrieves too much CWV in the tropical regions. Integrated over the global oceans, the Wentz data produces 1.03 10^{16} kg (= 31.76 kgm^{-2}) of water vapor over the global oceans, whereas the present method re-

trieves 9.23 10^{15} kg (= 29.38 kgm^{-2}) for the same period.A global mean approximately 25.5 kgm^{-2} is reported by Rosen *et al.* (1979) and Peixoto and Oort (1983) from rawind sonde observations (mainly over land. To obtain the mean CWV value given by the Wentz retrieval method the CWV a mean value of 13.87 kgm^{-2} is required over land.

8.0 Summary and Conclusion

An algorithm to retrieve precipitable water content (CWV) over the global oceans from SSM/I observations at 19.35 GHz has been described. The basic philosophy is to utilize measurements of the polarization state or the radiation field at the top of the atmosphere given the polarization state at the sea surface, a function of near surface wind speed and SST. It is shown that the radiation field at 19.35 GHz is only weakly dependent on the actual SST and near surface wind speed in correspondence with results reported by Prabhakara *et al.* (1983). A radiative transfer analysis is presented and shows the significant limitations of the 22.235 GHz water vapor channel for remote sensing water vapor in the moist atmosphere with CWV's in excess of 40 kgm^{-2}. It is because of this limitation that the present method is developed, but it is not ideal as it suffers from its own sensitivities summarized below. The limitations of the SSM/I for sensing tropical water vapor should be a concern addressed in NASA's TRMM program.

To estimate the polarization state at the sea surface only rough estimations for SST (within 4 K) and the near surface wind speed (within 4 ms^{-1}) are sufficient to retrieve CWV within 2 kgm^{-2}. The SST information is taken from Reynolds (1988), which is a monthly mean data set based on a blending of *in situ* and bouy observations and satellite observations. The near surface wind speed is found from an algorithm proposed by Wilheit (1979) and Wentz (1983). It is concluded that the present retrieval scheme is in good agreement with the independent observations provided by rawindsondes. The rawind soundings used for this comparison study were selected to be within 1^{o} and within the same day of the SSM/I observation. The standard deviation between the two datasets was found to be 6 kgm^{-2}, which is somewhat larger than previous reported results. Since the present retrieval scheme does not distinguish between liquid and precipitable water, large errors in the instantaneous retrieved CWV especially in the tropical regions (up to 5 kgm^{-2}) can be expected due to liquid water contamination in the present retrievals scheme. However, when integrated over one month, the error associated with LWC contamination is probably small, since only thick persistent

clouds contribute significantly to this error. This conclusion is supported by a comparison between monthly mean maps of CWV derived from SSM/I observations using the present method with the same map derived from the same observations over the same period of time but using a different retrieval scheme which distinguishes between LWC as described by Wentz (1983). From this comparison it is found that in general the two methods yields the same results except in the tropics where the Wentz method retrieves about 10 kgm^{-2} more CWV than the present. This is contrary to what would be expected from LWC contamination. In a future study, the authors plan to couple the present scheme into a method for the retrieval of cloud liquid water content.

Acknowledgments

Acknowledgment is made to the National Center for Atmospheric Research, which is sponsored by the National Science Foundation, for the computing time used in this research. This study is sponsored in part by grants from NASA (NAG 5-112) , NSF (ATM - 8907414) and NOAA (NA90AA-D-AC822).

Appendix A. Variables and constants

$e_s^{h,v}$	Surface emissivity in the horizontal (h) and vertical (v) polarization state	
g_0		
g_1	Constants in the linear relation between the surface reflectivity ratio (3.4) and the near surface wind speed	$[sm^{-1}]$
I	Specific intensity	$[Wm^{-2}Hz^{-1}sr^{1}]$
CWV	Columnar water vapor	$[kgm^{-2}]$
$r_s^{h,v}$	Surface reflectivity in the horizontal (h) and vertical (v) polarization state	
S	Source function	$[Wm^{-2}Hz^{-1}sr^{1}]$
T_b	Brightness temperature	[K]
T_c	Climatological SST	[K]
T_s	Sea surface temperature (SST)	[K]
$\bar{T}$	Reduced temperature	[K]
$\hat{T}$	Enhanced temperature	[K]
V	Near surface wind speed	$[ms^{-1}]$
z_p	e-Folding depth of water vapor	[m]
z_t	Top of the atmosphere	[m]
z_0	Surface	[m]
γ	Temperature lapse rate	$[Km^{-1}]$

κ	Mass absorption coefficient	$[m^2kg^{-1}]$
θ	Angle between vertical and propagation direction	
ρ	Density	$[kgm^{-2}]$
r_{h_2o}	As ρ but for water vapor	$[kgm^{-2}]$
ρ_{ox}	As ρ but for oxygen	$[kgm^{-2}]$
τ	Total transmission	
τ_{h_2o}	as τ but for water vapor	
τ_{ox}	as τ but for oxygen	

Constants

$\tau_{ox}(19.35\ GHz) = 0.9806$

$\gamma = -6.5\ 10^{-3}\ [Km^{-1}]$

$z_\rho = 2.00\ 10^3\ [m]$

$\kappa \sec\theta = 4.4516\ 10^{-3}\ (300/T_s)^{0.47733}$ at 19.35 GHz

$\kappa \sec\theta = 1.0129\ 10^{-2}\ (300/T_s)^{1.3}$ at 22.235 GHz

g_0 calculated from the Fresnel equations

$$g_1 = -89391\times10^{-3} + 8.104\times10^{-5}(T_s - 275) - 2.0184\times10^{-6}(T_s - 275)^2\ [sm^{-1}]$$

Appendix B. Alternative retrieval methods

Let the brighness temperature at the top of the atmosphere be given by (20), then the brightness temperature difference between two adjacent frequencies can be written as

$$T_b(\upsilon_1) - T_b(\upsilon_2) = T_s(1 - r_1\tau_1^2) - T_s(1 - r_2\tau_2^2) \tag{B.1}$$

$$= T_s\bar{r}(\tau_2^2 - \tau_1^2) \tag{B.2}$$

assuming that $r_1 \approx r_2 = \bar{r}$

Wentz (1983) showed that for the SMMR frequencies $\bar{r} = O(\frac{1}{T_s})$

such that $T_s\bar{r}$ is approximately independent of the surface temperature. Furthermore, if this difference is evaluated for the brightness temperature in the vertical polarization state then this difference is also insensitive to the actual wind speed, because $dT^v/dw_s \approx 0$. (cf. Table 1)

From (20) it is also clear that

$$R = \frac{T_b(\upsilon_1) - T_s}{T_b(\upsilon_2) - T_s} = \frac{r_1}{r_2}\left(\frac{\tau_1}{\tau_2}\right)^2 \approx \left(\frac{\tau_1}{\tau_2}\right)^2 \tag{B.3}$$

again assuming that $r_1 \approx r_2 = \bar{r}$. From we see that R as defined by eq. (5) is independent of the actual state of the surface emission.

References

Bronshtein, I.N. and K.A. Semendyayev, 1979: *Handbook of mathematics.* Van Nostrand Reinhold co. 118-122.

Chandrasekhar S., 1960: *Radiative transfer.* Dover Publications, Inc. 1-52.

Chang A.T.C. and Wilheit T.T., 1979: *Remote sensing of atmospheric water vapor, liquid water and wind speed at the ocean surface by passive microwave techniques from the Nimbus 5 satellite.* Radio Sci., **15 5**, 793 - 802

Chang H.D., Hwang P.H. Wilheit T.T., Chang A.T.C., Staelin D.H. and Rozenkranz P.W., 1984: *Monthly distributions of precipitable water from the NIMBUS 7 SMMR data.* J. Geophys. Res. 89 D4, 5328 - 5334.

Gruber, A. and Watkins C.D., 1981: *Preliminary evaluation of moisture from NOAA polar orbiting satellite sounding radiances.* J. Appl. Meteor., **20**, 450 - 466

Hayden D.M., Smith W.L. and Woolf, 1981: *Determination of moisture from NOAA polar orbiting satellite sounding system.* Amer. Water. Res. Ass., 115 - 466.

Hillger D.W. and Vonder Haar T.H., 1981: *Retrieval and use of high resolution moisture and stability fields from NIMBUS 6 HIRS radiances in pre- convective situations.* Mon. Wea. Rev., **109**, 1788 - 1806.

Hollinger J.P., 1971: *Passive microwave measurements of sea surface roughness.* IEEE Trans. Geosci. Electron., **GE-9 3**, 165 - 169.

Hollinger J.P., Lo R., Poe G., Savage R., and Pierce J., 1987: *Special sensor microwave/imager user's guide.* Naval research laboratory.

Illari L., 1989: *The quality of satellite precipitable water content data and their impact on analyzed moisture fields.* Tellus, **41A**, 319 - 337.

Jackson J.D., 1975: *Classical Electrodynamics.* John Wiley & Sons. 821 - 822.

Klein L.A. and Swift C.T., 1977: *An improved model for the dielectric constant of sea water at microwave frequencies.* IEEE J. Oceanic. Eng., **OE-2 1**, 104 - 111.

Manabe S. and Wetherald R.T, 1967: *Thermal equilibrium of the atmosphere with a given distribution of relative humidity.* J. Atmos. Sci., **24 3**, 241 - 259.

McClatchey R.A., Fenn R.W., Selby J.E.A., Volz F.E., and Garing J.S., 1972: *Optical properties of the atmosphere.* AFCRL-72-0497.

Njoku E.G. and Swanson L., 1983: *Global measurements of sea surface temperature, windspeed and atmospheric water content from satellite microwave radiometer.* Mon. Wea. Rev., **111**, 1977 - 1987.

Pandey P.C. and Kakar R.K., 1982: *An empirical microwave emissivity model for a foam covered sea.* IEEE J. Oceanic. Eng., **OE-7 3**, 135 - 140.

Peixoto J.R. and Oort A.H., 1983: *The atmospheric branch of the hydrological cycle and climate.* in Variations on the Global Water Budget, D. Riedel, 5 - 65, Hingham, Mass.

Prabhakara C., Chang H.D. and Chang A.T.C., 1982: *Remote sensing of precipitable water over the oceans from Nimbus-7 microwave measurements.* J. Appl. Meteor., **21**, 59 - 68.

Prabhakara C., Dalu G., Lo R.C. and Nath N.R., 1979: *Remote sensing of seasonal distribution of precipitable water vapor over the oceans and the interference of boundary layer structure.* Mon. Wea. Rev., **107**, 1388 - 1401.

Prabhakara C., Short D.A., Wiscombe W., and Fraser R.S., 1986: *Rainfall over oceans inferred from Nimbus-7 SMMR: Application to 1982-833 El Nino.* J. Climate Appl. Meteor., **25**, 1464 - 1474.

Prabhakara C., Wang I., Chang A.T.C. and Gloersen P., 1983: *A statistical examination of Nimbus-7 SMMR data and remote sensing of sea surface temperature, liquid water content in the atmosphere and surface wind speed.* J. Climat. Appl. Meteor., **22**, 2023 - 2037.

Ravel A. and Ramanathan V., 1989: *Observational determination of the greenhouse effect.* Nature, **342**, 758 - 761.

Reynolds R.W., 1988: *A real time global sea surface temperature analysis*. J. Climate, **1**, 75 - 86.

Rosen R.T., Salstein D.A. and Peixoto J.P., 1979: *Variability in the annual fields of large-scale atmospheric water vapor transport*. Mon. Wea. Rev., **107**, 26-37.

Shen W.C. and Smith W.L., 1973: *Statistical estimation of precipitable water with SIRS-B water vapor radiation measurements*. Mon. Wea. Rev., **101**, 24 - 32.

Simpson J., Adler R.F. and North G.R., 1988: *A proposed tropical rainfall measuring mission (TRMM) satellite*. Bull. Amer. Meteor. Soc., **69**, 278 - 295.

Stephens G.L., 1990: *On the relationship between vapor over the ocean and sea surface temperature*. J. Climate, **3**, 634 - 645.

Waters J.W., 1976: *Absorption and emission of microwave radiation by atmospheric gases*. In: Methods of experimental physics, M.L.Meeks ed. Academic Press Section 2.3.

Wentz F.J., 1983: *A model function for ocean microwave brightness temperature*. J. Geophys. Res., **88 C3**, 1892 - 1908.

Wetherald R.T. and Manabe S., 1988: *Cloud feedback processes in a general circulation model*. J. Atmos. Sci., **45**, 1397- 1415.

Wilheit T.T., 1979: *The effect of wind on the microwave emission from the ocean's surface at 37 GHz*. J. Geophys. Res., **84 C8**, 4921 - 4926.

Wilmott C.J., 1982: *Some comments on the evaluation of model performance*. Bull. Amer. Meteor. Soc., **63**, 1309 - 1313.

Figure and Table Captions

Fig. 1: Relation between the monochromatic brightness temperature difference at the top of the atmosphere between two adjacent frequencies as a function of columnar water vapor calculated for 78 different rawindsonde ascents using our detailed microwave radiative transfer model. The solid points represent the calculated difference between the brightness temperatures at 21 and 18 GHz whereas the open points represents the brightness temperature difference at 22.235 and 19.35 GHz

Fig. 2: Relation between R defined by (5) in the text and CWVcalculated for 78 different rawindsonde ascents.

Fig. 3: The calculated difference between the horizontal and vertical polarized brightness temperature at the top of the atmosphere as a function of CWV

Fig. 4: Correlation between the transmission function evaluated by a microwave radiative transfer model at 19.35 GHz (solid points) and at 22.235 GHz (open points) for 78 different rawindsonde ascents as a function of columnar water vapor.

Fig. 5: Comparison of the normalized sensitivity of three retrieval methods as a funcion of CWV

Fig. 6: Comparison of columnar water vapor derived from SSM/I observations over the global oceans for September, October and November 1987 using the present retrieval method, with columnar water vapor derived from quasi-coincident rawindsonde observations

Fig. 7: As Fig. 6 but now for the Chang and Wilheit retrieval method asapted for SSM/I observations.

Fig. 8(a): Horizontal distribution of the seasonal mean columnar water vapor derived from SSM/I observations over the global oceans for September, October and November 1987 using the present retrieval method.

Fig 8(b): The standard deviation in CWV indicating departures of instantaneous observations from the seasonal mean. These deviations are averaged to produce seasonal mean values for SON 87.

Fig. 9: Correlation between sea surface temperature and columnar water vapor as derived from SSM/I using the present retrieval method (open circles), using the adopted Chang and Wilheit method (triangles). As shown is the correlation as derived from SMMR observations (closed circles)

Fig. 10: As Fig. 8 but for the adopted Chang and Wilheit retrieval method

Fig. 11. Correlation between sea surface temperature and columnar water vapor as derived from SSM/I observations for September 1987 using the present retrieval method (open circles), and according to the Wentz dataset (closed circles)

Table 1: Theoretical radiometric metric sensitivities at 19.35 GHz for a standard tropical (TRP), midlatitude summer (MLS) and midlatitude winter (MLW) atmosphere.

Table 2: Values for the maximum and threshold radiometric sensitivities of the retrieved CWV with respect to observational errors in the brightness temperature

Table 3: Quantitative measures of a linear regression analysis between SSM/I retrieved CWV and quasi-coincident rawindsonde observed CWV.

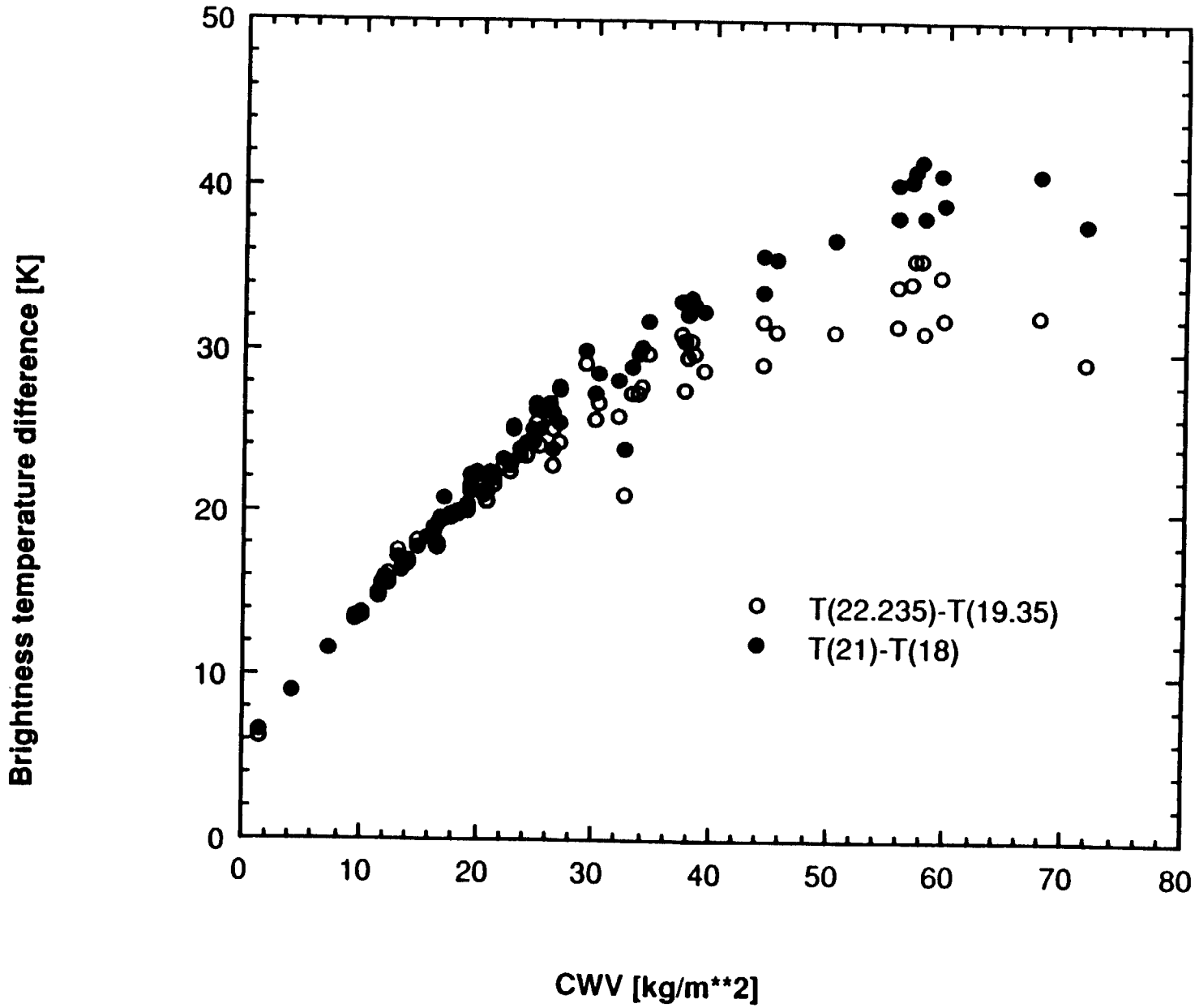
Brightness temperature difference [K]
CWV [kg/m**2]
T(22.235)-T(19.35)
T(21)-T(18)
0
10
20
30
40
50
60
70
80

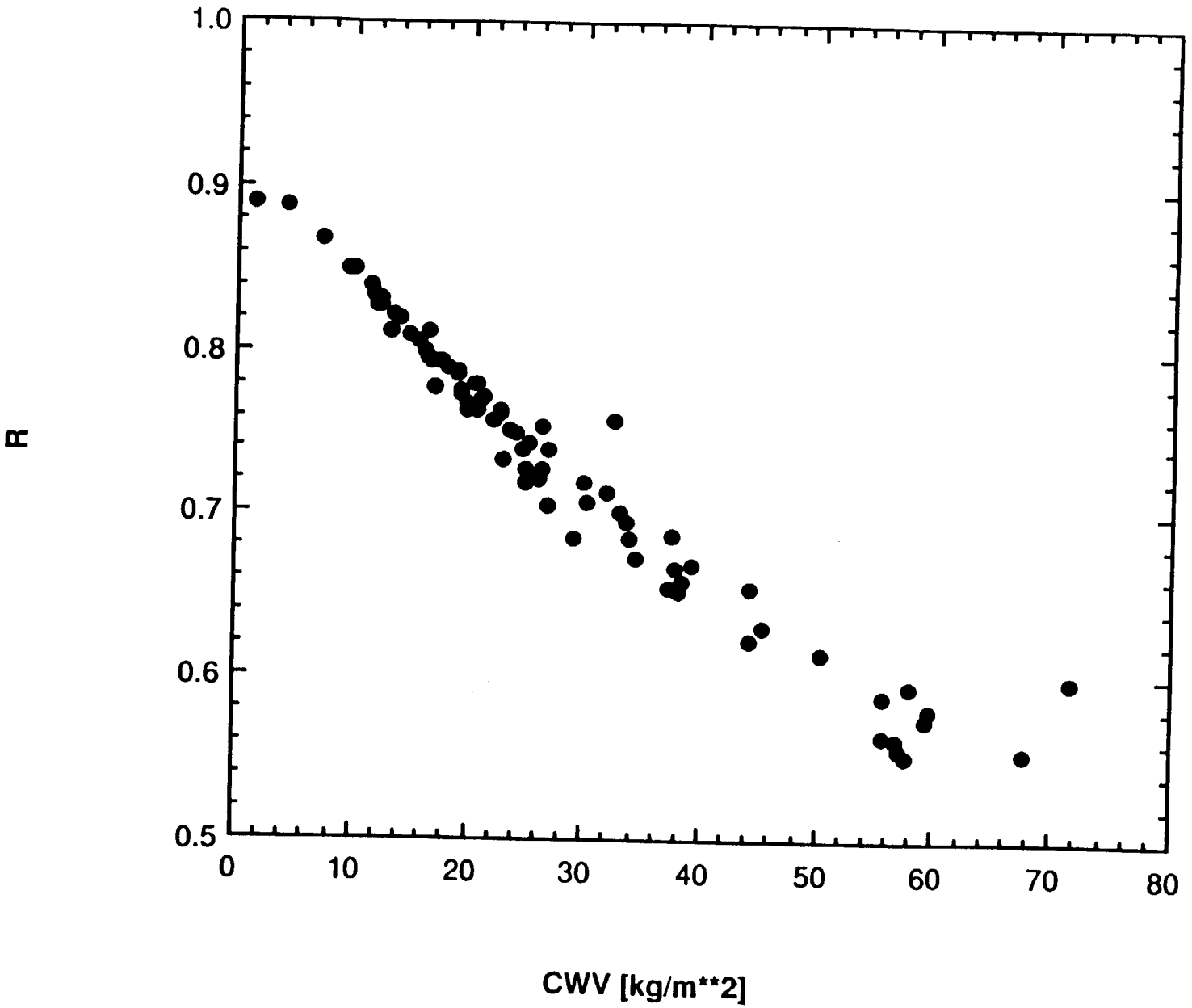
1.0
0.9
0.8
0.7
0.6
0.5
R
0
10
20
30
40
50
60
70
80
CWV [kg/m**2]

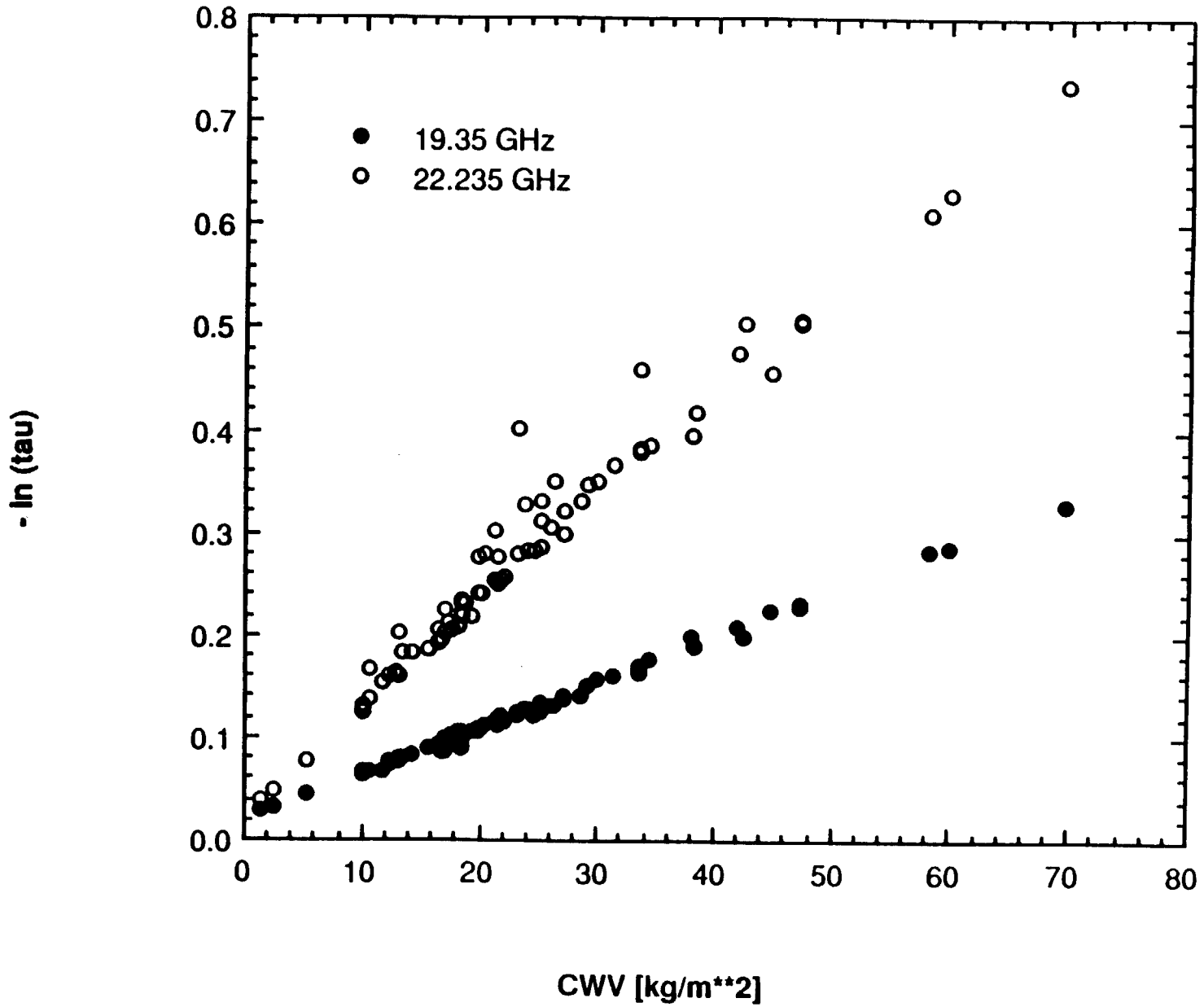
0.8
0.7
0.6
0.5
0.4
0.3
0.2
0.1
0.0
- ln (tau)
19.35 GHz
22.235 GHz
0
10
20
30
40
50
60
70
80
CWV [kg/m**2]

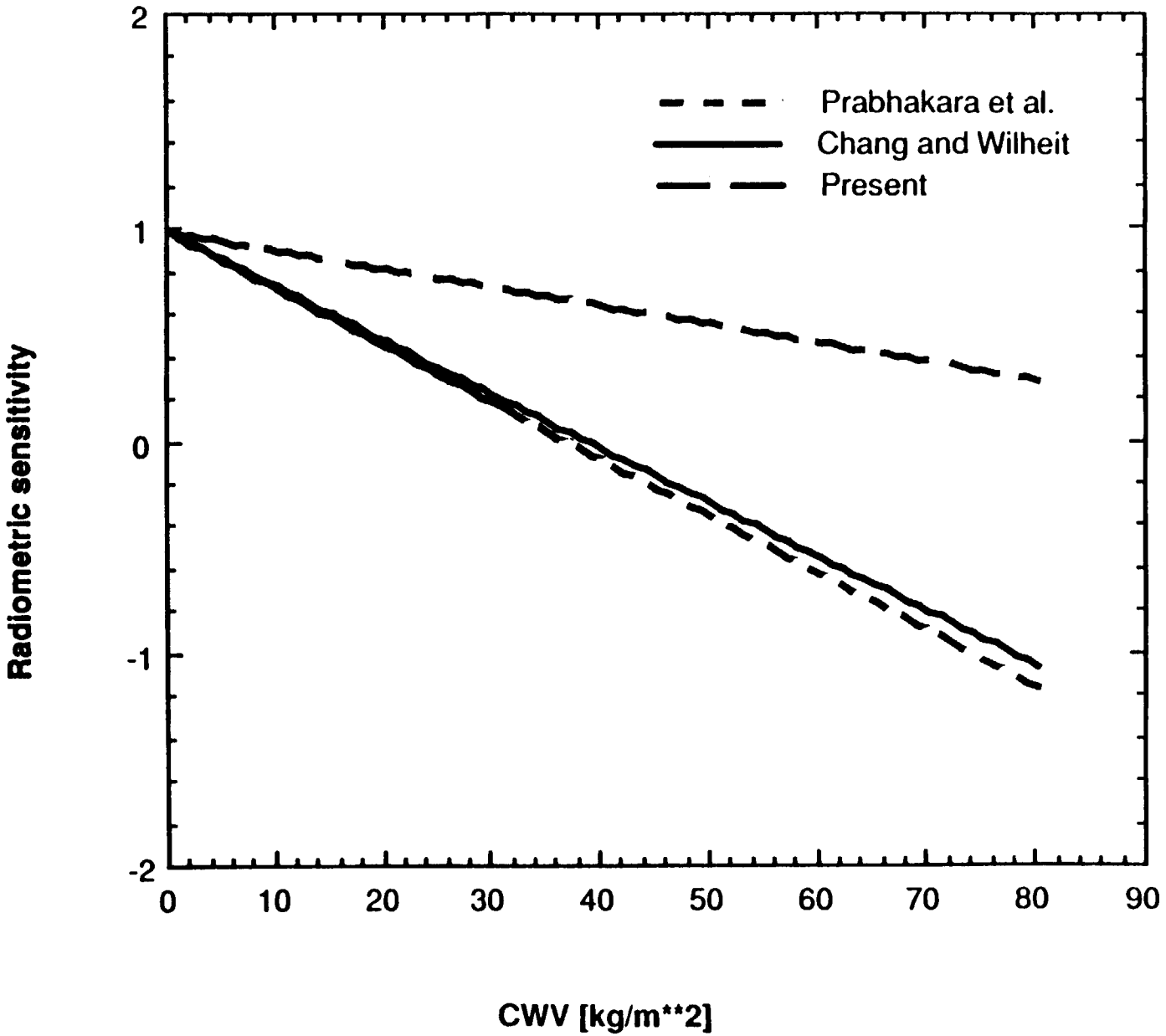
Prabhakara et al.
Chang and Wilheit
Present
Radiometric sensitivity
CWV [kg/m**2]
2
1
0
-1
-2
0
10
20
30
40
50
60
70
80
90

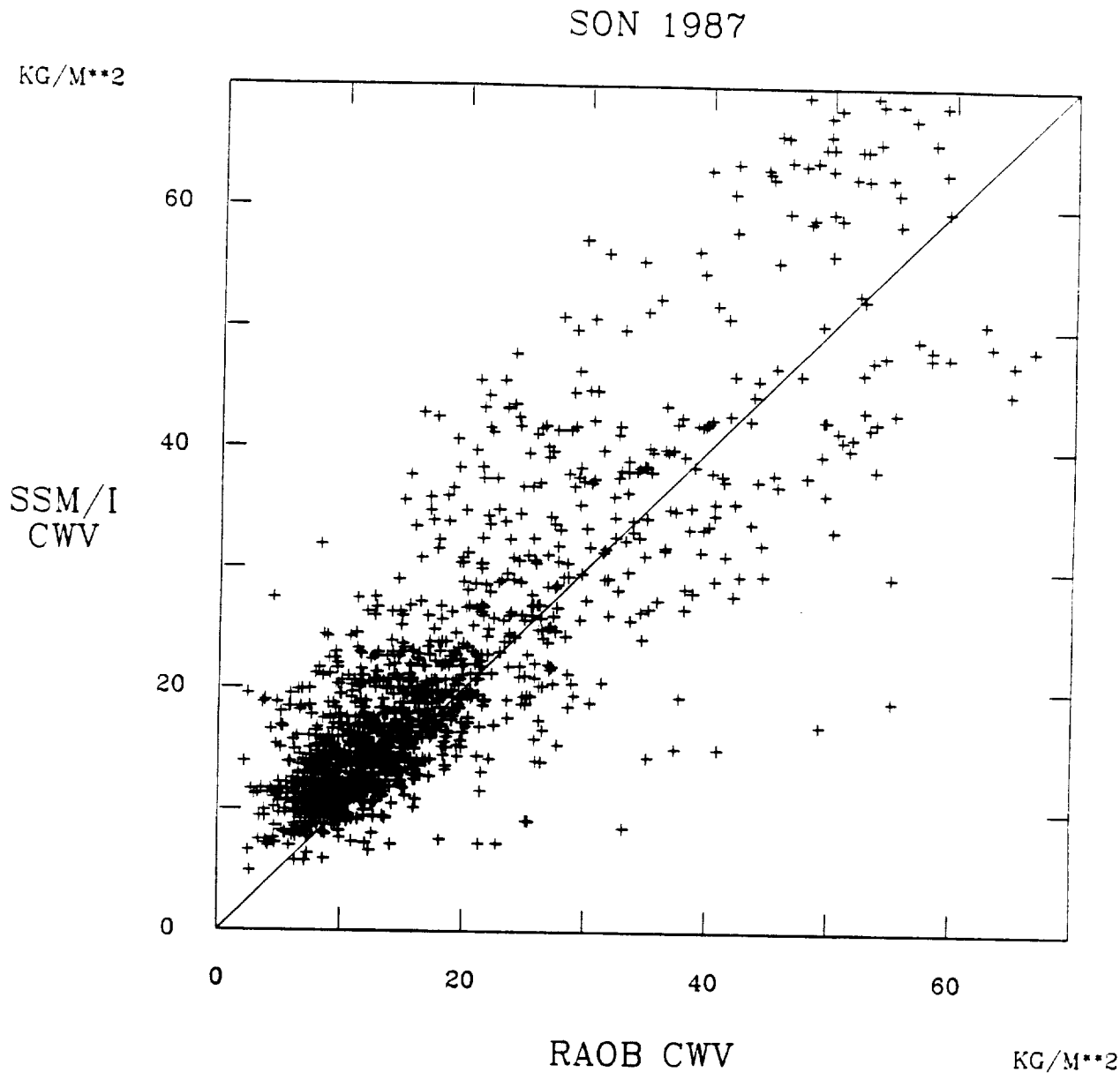
SON 1987
KG/M**2
60
40
20
0
SSM/I
CWV
0
20
40
60
RAOB CWV
KG/M**2

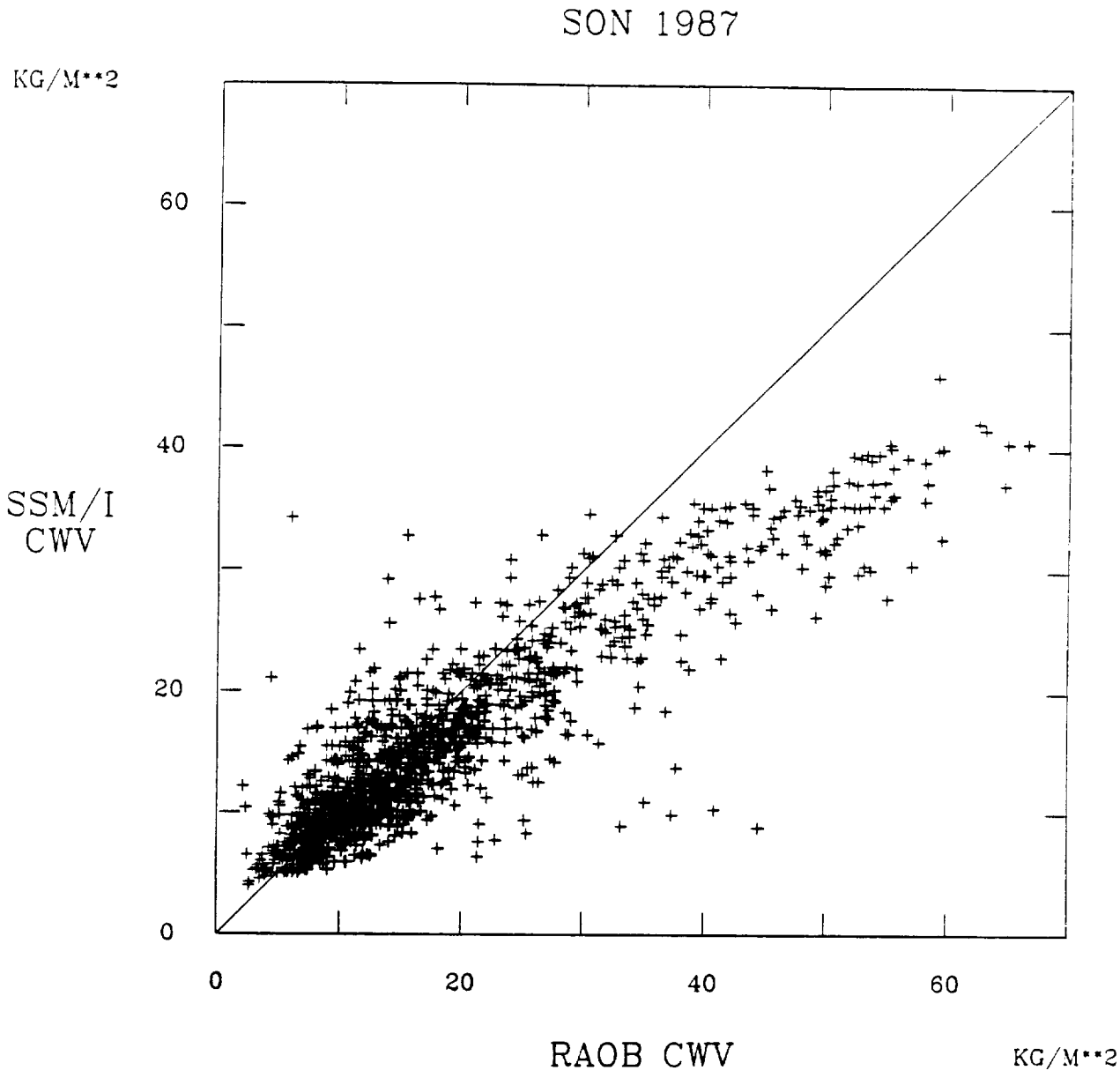
SON 1987
KG/M**2
60
40
SSM/I
CWV
20
0
0
20
40
60
RAOB CWV
KG/M**2

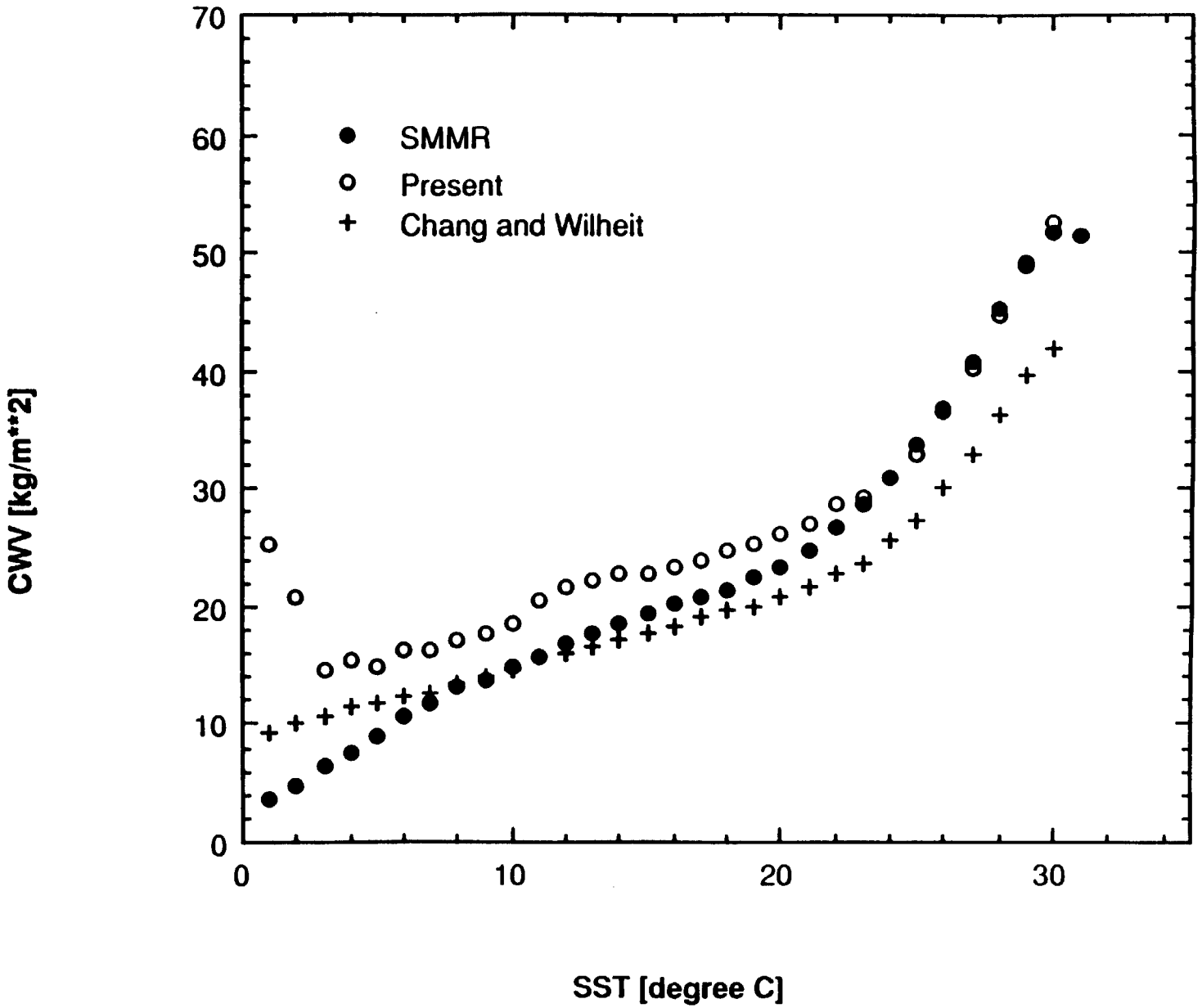
70
60
50
40
30
20
10
0
0
10
20
30
SMMR
Present
Chang and Wilheit
CWV [kg/m**2]
SST [degree C]

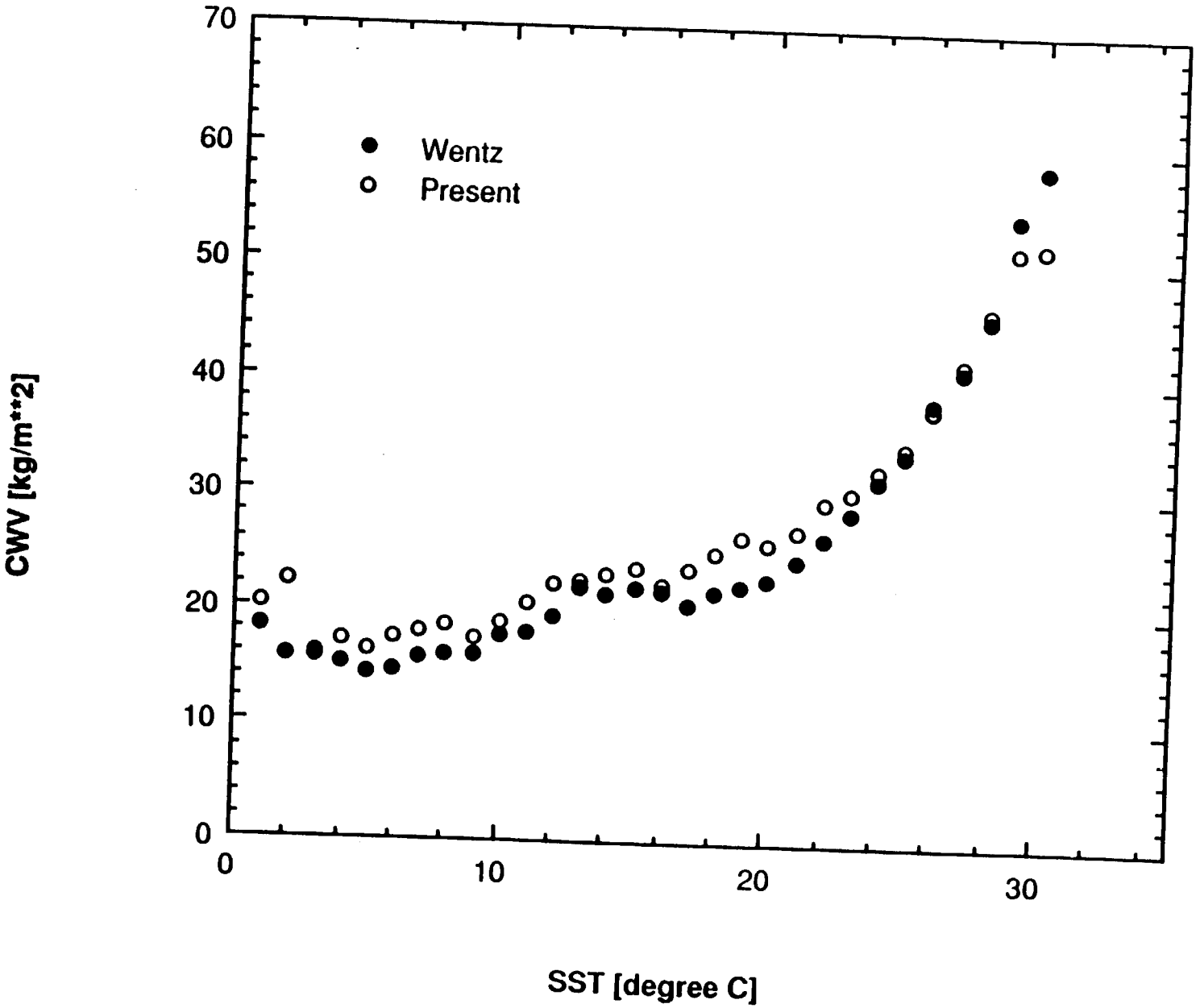
70
60
50
40
30
20
10
0
0
10
20
30
Wentz
Present
CWV [kg/m**2]
SST [degree C]

Table 1

Atmospheric profile	TRP	MLS	MLW
CWV [kgm^{-2}]	57.18	40.96	10.16
T_S [K]	300.0	294.0	273.0
dT^v/dT_s [K/K]	0.311	0.264	-0.291
dT^h/dT_s [K/K]	0.135	0.099	-0.298
$dT^v/dCWV$ [K/kgm^{-2}]	0.568	0.628	0.658
$dT^h/dCWV$ [K/kgm^{-2}]	0.943	1.044	1.176
dT^v/dw_s [K/ms^{-1}]	0.248	0.295	0.361
$dCWV/dT_s$ [kgm^{-2}/K]	-0.469	-0.397	-0.014
$dCWV/dw_s$ [kgm^{-2}/ms^{-1}]	2.160	2.168	2.135

Table 2

Retrieval Algorithm	Maximum Sensitivity $[m^2kg^{-1}]$	Threshold sensitivity $[m^2kg^{-1}]$
Chang and Wilheit (1979)	$-9.0732\ 10^{-3}$	0.005
Prabhakara *et al.* (1982)	$6.3994\ 10^{-3}$	-0.005
Present	$-7.9964\ 10^{-3}$	0.002

Table 3

Variable	Raobs	Present	ACW
Number of observations	1188		
Mean [kgm^{-2}]	16.93		17.61
Standard deviation [kgm^{-2}]	11.20		9.36
Offset [kgm^{-2}]			5.44
Slope			0.670
Mean absolute error [kgm^{-2}]			3.824
Root mean square error [kgm^{-2}]			5.995
Systematic rms [kgm^{-2}]			4.122
Unsystematic rms [kgm^{-2}]			4.353

Preprint, 19th Conf. on
Hurricanes and Tropical
Meteorology, May 6-10, 1991.

N15

Low Frequency Oscillations in Radiative-Convective Models

Qi Hu and David A. Randall

Department of Atmospheric Science
Colorado State University
Fort Collins, CO. 80523

1. INTRODUCTION

Although eastward propagation is usually regarded as an essential feature of the low frequency Madden-Julian oscillation observed in the tropical atmosphere (e.g., Chang, 1977, Lau and Peng, 1987, and Wang and Chen, 1989), many observations indicate that there is an important stationary or quasi-stationary component of the oscillation. Yasunari (1979), for example, investigated the stationary 30-60 day variation in upper tropospheric cloudiness in the Asian summer monsoon region. In a case study of the 30-60 day oscillation, Hsu et al. (1990) found that a case may not complete the global circle while its phase cycle has been complete. Some of their cases show a strong stationary oscillation of the divergence, outgoing longwave radiation (OLR) and other fields. A recent observational study by Weickmann and Khalsa (1990) offers further evidence that the Madden-Julian oscillation has an important stationary component.

In this paper, we present evidence that intraseasonal oscillations can be produced by local radiative and convective processes. This suggests that the observed propagating "Madden-Julian wave" is produced by interactions between these local processes and the large scale motion field, and is not essential for the existence of the observed oscillation. We show that the interactions between radiative and convective processes over the warm tropical oceans can lead to low frequency oscillations.

2. THE MODELS

Two different models have been used to describe, with different degrees of physical detail, the local interactions among radiation, boundary-layer processes, and convection.

In a highly simplified model (thereafter Model 1) the radiation process is approximated by cooling to space (Rodgers and Walshaw, 1966) and convection is included through the adjustment scheme of Manabe et al. (1965).

In a more sophisticated model (Model 2), which is essentially a single-column version of the Colorado State University (CSU) general circulation model (GCM) described by Randall et al. (1991) and references therein, we use a full parameterization of solar and infrared radiative transfer (Harshvardhan et al., 1987), and the Arakawa-Schubert cumulus parameterization (Arakawa and Schubert, 1974).

A fixed sea surface temperature (SST) is imposed as the lower boundary condition in both models. The latent and sensible heat fluxes from the ocean surface are determined using the bulk aerodynamic formula with a prescribed surface wind speed.

Both models reach a quasi-equilibrium state after a few hundred simulated days. The results for the last 500 days of 2000-day integrations are presented in the following section.

3. RESULTS

Fig. 1 shows the variation of precipitation amount from Model 1, with SST=301.5 K and a surface wind speed of 5 m s^{-1}.

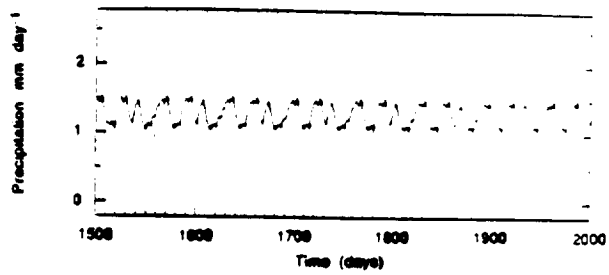

Figure 1: Time hisory of the precipitation rate from Model 1.

An oscillation with a period near 34 days is evident (Fig. 2).

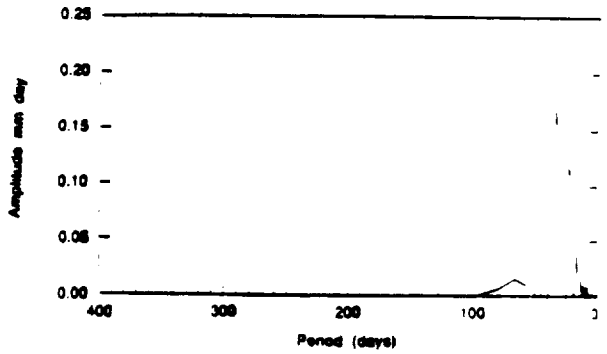

Figure 2: The spectrum of the precipitation data shown in Fig. 1.

The fluctuations of atmospheric temperature and moisture during the first 100 days of this 500 day segment are plotted in the panels of Fig. 3.

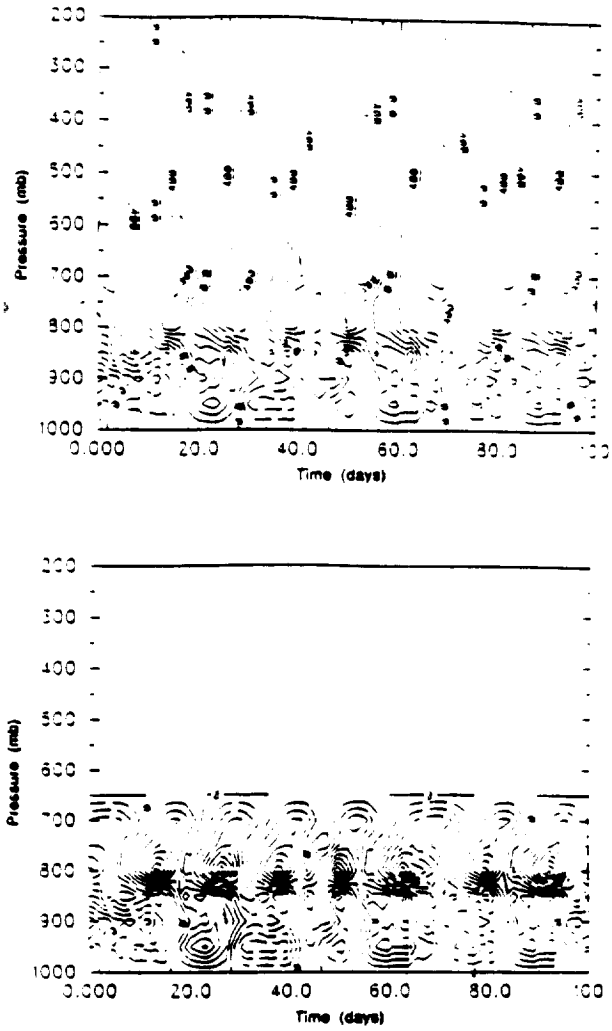

Figure 3: a) The fluctuations of atmospheric temperature during a 100 day segment of the simulation with Model 1. The contour interval is 0.1 K. b) The fluctuations of atmospheric moisture during a 100 day segment of the simulation with Model. The contour interval is 0.1 g kg^{-1}.

The temperature variations in the middle and upper troposphere are out of phase with those in the lower levels; warming in the lower levels is accompanied by a cooling in the upper levels and vice versa. Intense convection occurs while the upper levels are warming/moistening and the lower levels are cooling/drying. Weaker convection occurs while the upper levels are cooling/drying and the lower levels are warming moistening. The variations shown in Fig. 3 illustrate a thermal destabilization as moisture and heat accumulate in the lower levels and radiative cooling occurs aloft, and a thermal stabilization as convection transports both moisture and sensible heat from lower levels to the upper levels.

The results from Model 2 are shown in Figs. 4 - 6.

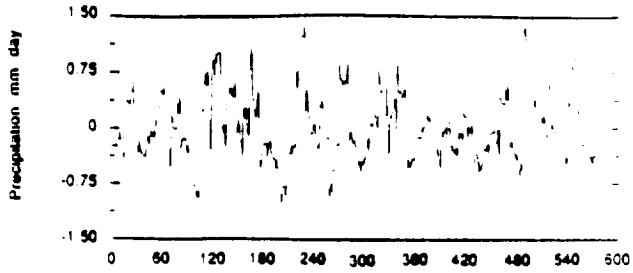

Figure 4: The time-history of the precipitation rate (minus its time average) from Model 2.

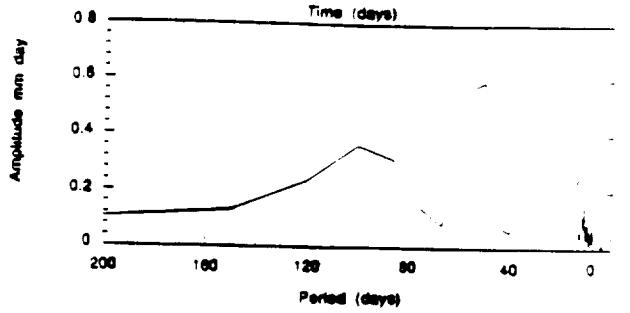

Figure 5: The spectrum of the precipitation data shown in Fig. 4.

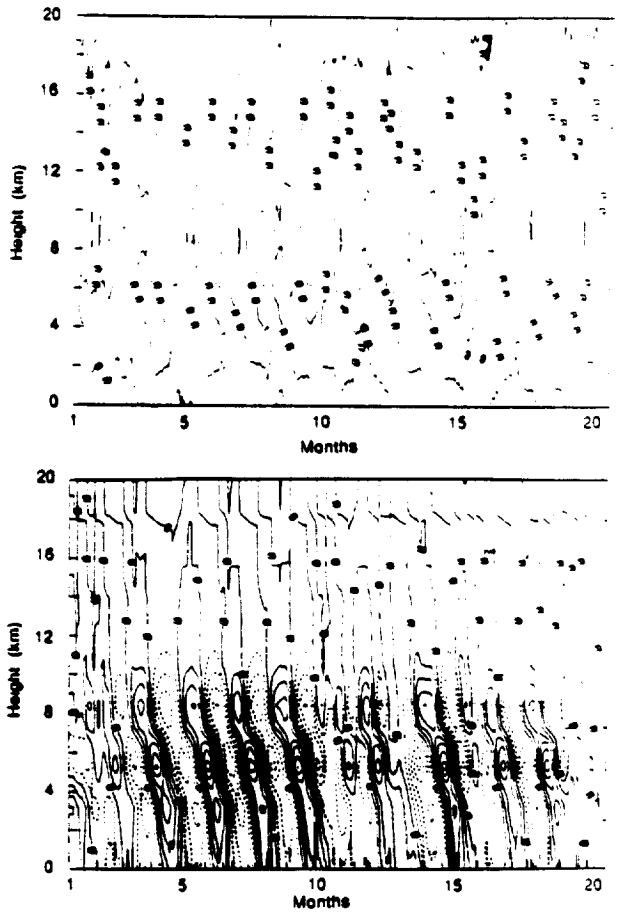

Figure 6: a) The fluctuations of atmospheric temperature during a 100 day segment of the simulation with Model 2. The contour interval is 0.1 K. b) The fluctuations of atmospheric moisture during a 100 day segment of the simulation with Model 2. The contour interval is 0.1 g kg^{-1}.

In these runs we used an SST of 300.0 K and a surface wind speed of 5 m s^{-1}. Model 2 produces oscillations of temperature and moisture that are quite similar to those of Model 1. *This is remarkable given the drastic differences in the formulations of the two models.* As seen in the figures, sensible heat and moisture accumulate in the lower levels; this is followed by an episode in which moisture is transported upward by more intense convection. Again a cycle of thermal destabilization and stabilization occurs with a period of 53 days.

Deep convection intensifies when moistening is a maximum, the upper levels are cool, and the lower levels are warm. Through both radiative and latent heating, more intense convection leads to a warming of the upper troposphere. It also moistens the upper troposphere through cumulus detrainment. The warming of the upper levels represents a thermal stabilization of the column, which suppresses convection and allows an accumulation of sensible heat and moisture in the lower levels. This accumulation is followed by a new round of more intense convection.

Similar low frequency oscillations occur, with varying intensities, for a wide range of SSTs and surface wind speeds. More intense oscillations are associated with warmer SSTs.

4. DISCUSSION AND CONCLUSIONS

Our strategy now is to simplify Model 2, in a step-by-step process, to identify which physical processes are important for the oscillation and which are not. The fact that the oscillation does occur in the much simpler Model 1 can guide this process. We have already determined, through experiments with Model 2, that the process does not depend in any important way on the radiative effects of the clouds or on the variability of the planetary boundary layer depth. Additional experiments are in progress.

We offer the following tentative explanation for our results: Conditional instability can be generated, in our 1-D models, by radiation and boundary-layer processes. Both moist convective adjustment and the Arakawa-Schubert scheme instantaneously release conditional instability, i.e., they force the models to occupy moist neutral states. In both models, the existence of moist instability depends on the temperature lapse rate and also on the amount and distribution of water vapor. The oscillations produced by the models may be due to the existence of two "attracting" moist-neutral states: the first with a stronger temperature lapse rate and a lower moisture content, and the second with a weaker lapse rate and more moisture. The convective and radiative tendencies associated with the first state drive the system towards the second, and vice versa. The period of the oscillation is that associated with the radiative cooling, and perhaps also by the time needed for moisture to accumulate in the column.

Our results show that a low frequency oscillation can be excited through radiative-convective interactions in the presence of energy exchange at the sea surface. This oscillation may well be responsible for the observed stationary low frequency fluctuations in the tropics. It may also provide a foundation for studies in which a pre-specified oscillatory forcing is driving the tropical dynamic process (e.g., Gill, 1980).

5. ACKNOWLEDGMENTS

Prof. Duane Stevens of the University of Hawaii instigated an earlier phase of this study, as reported by Stevens et al. (1989).

This research has been sponsored by NASA Grant NAG 5-1058 to Colorado State University, and by the U.S. Department of Energy under Grant DE-FG02-89ER69027 to Colorado State University.

6. REFERENCES

Arakawa, A., and W. H. Schubert, 1974: The interaction of a cumulus ensemble with the large scale environment, Part I. *J. Atmos. Sci.*, **31**, 647-701.

Chang, C.P., 1977: Viscous internal gravity waves and low-frequency oscillations in the tropics. *J. Atmos. Sci.*, **34**, 901-910.

Gill, A.E., 1980: Some simple solutions for heat-induced tropical circulation. *Quart. J. Roy. Meteor. Soc.*, **106**, 447-462.

Harshvardhan, R. Davies, D.A. Randall, and T.G. Corsetti, 1987: A fast radiation parameterization for atmosphere circulation models, *J. Geophys. Res.*, **92**, 1009-1016.

Hsu, H.H., B.J. Hoskins, and F. Jin, 1990: The 1985/86 intraseasonal oscillation and the role of the extratropics. *J. Atmos. Sci.*, **47**, 823-839.

Lau, K.M., and L. Peng, 1987: Origin of low frequency (intraseasonal) oscillation in the tropical atmosphere, Part I: Basic theory. *J. Atmos. Sci.*, **44**, 950-972.

Manabe, S., and J. Smagorinsky and R.F. Strickler, 1965: Simulated climatology of general circulation with a hydrological cycle. *Mon. Wea. Rev.*, **93**, 769-798.

Randall, D. A., Harshvardhan, and D. A. Dazlich, 1991: Diurnal variability of the hydrologic cycle in a general circulation model. J. *Atmos. Sci.* (to appear).

Rodgers, C.D., and C.D. Walshaw, 1966: The computation of infra-red cooling rate in planetary atmosphere. *Quart. J. Roy. Meteor. Soc.*, **92**, 67-92.

Stevens, D. E., Q. Hu, G. Stephens, and D. Randall, 1989: The hydrologic cycle of the intraseasonal oscillation. Paper presented at the *Western Pacific International Meeting and Workshop on TOGA-COARE*, Noumea, New Caledonia, May 24-30, 1989.

Wang, B., and J. Chen, 1989: On the zonal-scale selection and vertical structure of equatorial intraseasonal waves. *Quart. J. Roy. Meteor. Soc.*, **115**, 1301-1323.

Weickmann, K.M., and S.J.S. Khalsa, 1990: The shift of convection from the Indian Ocean to the western Pacific Ocean during a 30-60 day oscillation. *Mon. Wea. Rev.*, **118**, 964-978.

Yasunari, T., 1979: Cloudiness fluctuations associated with the northern hemisphere summer monsoon. *J. Meteor. Soc. Japan*, **57**, 227-242.

THE HYDROLOGIC CYCLE OF THE INTRASEASONAL OSCILLATION

Duane E. Stevens, Qi Hu, Graeme Stevens
and
David Randall

Department of Atmospheric Science
Colorado State University
Fort Collins, CO 80523

1. INTRODUCTION

Since better understanding of 30-60 day oscillation can lead to improvements in medium and long range weather prediction, this phenomenon has attracted considerable attention. The 30-60 day oscillation was identified by Madden and Julian (1971, 1972) as the eastward propagation of a wavenumber 1 disturbance in tropical, tropospheric zonal wind and surface pressure fields. The range of the period of this disturbance corresponds to a zonal phase speed of 10 to 15 ms^{-1}. Other observational studies have documented disturbances with a similar period of 30 to 60 days in other physical fields. These findings include the oscillations in atmospheric angular momentum (Anderson and Rosen, 1983, and Risbey and Stone, 1988), convective activities and cloudiness (Yasunari, 1980), outgoing long wave radiation over the Indian-Western Pacific Oceans (Murakami *et al.*, 1986, among others) and perturbations in precipitation amount over the same area (Hartmann and Gross, 1988). In addition to atmospheric phenomena, 30-60 day fluctuations of sea level height (Enfield, 1987, and Mitchum and Lukas, 1987) and sea surface temperature (SST) (Enfield, 1987) have also been found. From these studies it is obvious that the 30-60 day oscillation is a complex process involving disturbances in both the tropical atmosphere and ocean.

Despite the multitude of observational studies, a satisfactory theoretical explanation of the 30-60 day oscillation has yet to be agreed upon. Since Gill's (1982) finding, that the phase speed of the tropical waves can be significantly reduced due to reduction of the static stability (hence the equivalent depth) of the atmosphere by latent heat release, the linear tropical wave theory (Matsuno, 1966) after being refined by the diabatic heating parameterization, has been widely applied in explanation of the 30-60 day oscillation. For example, Lau and Peng (1987) proposed the 'mobile wave CISK' mechanism and Chang and Lim (1988) developed the 'Kelvin wave CISK' theory. Although the selected or the newly generated waves in these theories were indeed amplifying as propagating eastward the phase speed of these waves was crucially dependent on the diabatic heating profile used in these models. In order to have a phase speed close to the observed one the heating profile has to have a peak in the lower troposphere. This heating profile, however, is more representative of situations for the mid-latitude than of the tropics (Reihl and Malkus, 1958).

Attempts were also made to find new modes which could be responsible for the observed 30-60 day oscillation. Anderson and Stevens (1987), for example, specified several slow poleward propagating unstable modes in their 2-D eigenvalue model which included an equatorial symmetric Hadley circulation.

Studies in which the intraseasonal oscillation was regarded as an atmospheric response to a sporadic external heating with a 30-60 day period is another category in the approach. By postulating an oscillatory heating as the forcing, many experiments with different atmospheric models were able to produce the expected low frequency oscillatory features (Yamagada and Hayashi, 1984, and Salby and Gacia, 1987). The lack of an explicit instability mechanism in this category of explanation remains questionable, however, if one views the 30-60 day oscillation as purely an intrinsic atmospheric oscillation.

The sporadic 'external' forcing may turn into an 'internal' one when the ocean and atmosphere are considered as one system. Krishnamurti *et al.* (1988) has found the observational evidence of the air-sea interaction on the time scale of 30-60 days. Emanuel (1987) and Neeling *et al.* (1987) looked at the evaporation-wind feedback effect in an ocean-atmosphere system. They showed that the low frequency oscillation can be amplified by drawing energy from the warm ocean surface through this feedback. Although the existence of the oscillation does not depend on the evaporation-wind feedback (Neeling *et al.*, 1987) their studies certainly provided a different perspective for understanding this problem.

In this study, we propose a new theory explaining the origin of low frequency oscillations in the tropics. In our models both the lower atmosphere and upper ocean layers are included and are treated as a fully coupled system. Based on the model results, we suggest that the observed 30-60 day oscillations in the tropical troposphere and in the ocean are the manifestation of the cloud-radiation, atmosphere-ocean feedback processes, and that their realization depends on the hydrologic cycle in this system.

In the next section, the basic physical mechanism for the 30-60 day oscillation in terms of the hydrologic cycle is presented. Sections 3, 4 and 5 describe three different models and their results. Our conclusions are summarized in Section 6.

2. MECHANISM

The tropical atmosphere above the warm ocean surface is heated through the energy exchanges with the ocean. Meanwhile evaporation from the ocean moistens the lower part of

the tropical troposphere. The warmer the ocean mixed layer, the more heat and more moisture are added into this part of the atmosphere.

The removal of the accumulated 'extra' heat and moisture from the tropical atmosphere occurs through deep cumulus convection (Riehl and Malkus, 1958). This convection is crucial in the hydrologic cycle of the tropical atmosphere-ocean system. When explaining the conditional instability in the tropical atmosphere, Ooyama (1969) showed that the vertical temperature and moisture structures in the tropics possess a conditionally unstable character before the onset of convection. However, this instability is realized only when the lower troposphere is sufficiently moistened, through surface evaporation and/or large-scale convergence. This characteristic of the tropical atmosphere is important as it highlights the key role played by the moisture in the occurrence of tropical convection. In our conceptual models, presented in the next two sections, we will set a critical moisture value as the 'model atmospheric moisture tolerance' to represent this thermodynamic feature of the tropical atmosphere. This treatment principally follows the philosophy in parameterizing cumulus convection (Kuo, 1975, and Stevens and Lindzen, 1978) and is based on empirical evidence such as the observed moisture changes in synoptic scales wave disturbances (Reed and Recker, 1971).

When the conditional instability is being released, the convection not only diminishes the extra moisture in the atmosphere through precipitation but, through cloud-radiation interaction, also reduces the sea surface temperature by attenuating the solar radiation energy available at the ocean surface. The result of this is to return the extra water substance in the atmosphere back to the ocean and to reduce the sea surface temperature to its 'climatological' value.

In short, a natural cycle represented by the hydrologic process in the atmosphere-ocean system is spontaneously carried on in the tropics. Our model shows that, simply restricted by the 'moisture tolerance', such a cycle possesses an intraseasonal time scale.

3. A SIMPLE MODEL WITH FIXED SST

a) The Model

In this section we demonstrate the existence of the hydrologic cycle in a simple atmosphere-ocean system with *fixed* ocean parameters. The schematic structure of this model is given in Fig. 1. As shown in Fig. 1 only thermodynamic process are considered in this model. Our attention is to describe the accumulation of the extra water content in the atmospheric mixed layer through evaporation and the removal of this content by precipitation; horizontal convergence and divergence are neglected.

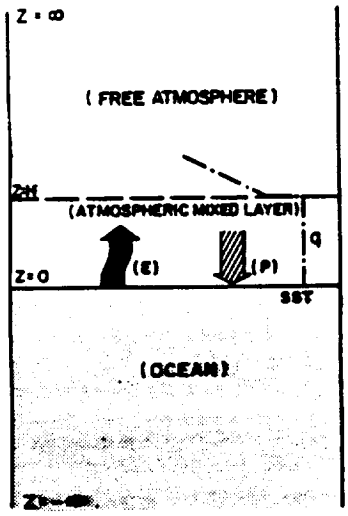

Fig. 1: Schematic structure of the model (MD1) with a fixed sea surface temperature (SST).

The temperature of the atmospheric mixed layer is characterized by a near-surface atmospheric temperature $T_a = T_s - \Delta T(^\circ C)$. Precipitation is assumed to take place when the 'atmospheric moisture tolerance' is achieved. As an initial approach we specify this critical condition as that when the mixing ratio of the atmospheric mixed layer reaches 90% of the saturation value at its temperature, T_a.

The amount of moisture evaporated in each time interval, Δt, is calculated by

$$\Delta E = \int_{\Delta t} E(t)dt\,, \tag{1}$$

where,

$$E(t) = \rho_a C_D |u_s||q_{sat}(T_s) - q_{atm}(t)| \tag{2}$$

(Neeling *et al.* 1987). In (2), ρ_a is the mean density of the atmospheric mixed layer, C_D is the surface drag coefficient and is treated as a constant of 0.001. The parameter u_s is the low level wind at 10 meters above the sea surface, $q_{sat}(T_s)$ is the saturation mixing ratio of the atmosphere at temperature T_s and $q_{atm}(t)$ is the actual mixing ratio of atmospheric mixed layer at time t. The value of q_{atm} is updated at time step $t + \Delta t$ by an increment Δq given by

$$\Delta q = \frac{1}{(\rho_a H)} \int_{\Delta t} (E(t) - P)dt\,. \tag{3}$$

Here P represents the precipitation rate and is assumed as a constant, $2.5mm/day$ (Wang, 1988) during the model's rainy period and H is the mixed layer depth.

By using a mean atmospheric moist state and the precipitation rate, the model is integrated with a one hour time interval for 1000 days.

b) Model Result and Sensitivity

Fig. 2 shows the results of two model integrations. Model parameters used in these integrations are listed in the figure caption. The displayed field, extra water content, indicates the column moisture amount above an assumed background state, which corresponds to a mixing ratio (q_{atm}) of $15g/kg$ in the atmospheric mixed layer.

An *ad hoc* parameterization of the low-level wind, intended to represent the higher winds and associated transfers between atmosphere and ocean during convection,

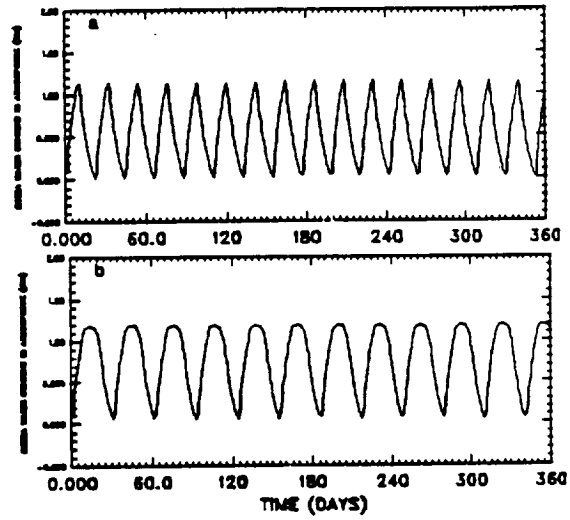

Fig. 2: Predicted hydrologic circulation in the model atmosphere–ocean system. The model low level wind, u_s, used in (a) is a constant of 2.0 m/s, and in (b) is that given in Eq. (4), with $u_b = 2\ m/s, u_m = 12\ m/s$, and $\Delta t_d = 13days$. Other model parameter values are $T_s = 28.5^\circ$C, $T_a = 28.0^\circ$C, $H_{atm} = 1500m$ and $P = 2.5mm/day$.

$$u_s(t) = \begin{cases} u_b & t \le t_c \\ u_m & t_c \le t \le t_c + \Delta t_m \\ u_m - \frac{u_m - u_b}{\Delta t_d}[t - (t_c + \Delta t_m)], & t_c + \Delta t_m \le t \le t_c + \Delta t_m + \Delta t_d, \end{cases} \quad (4)$$

is used in getting the result in Fig. 2b. In this expression u_b is the mean background wind speed and t_c is the time when the atmospheric moisture tolerance is achieved. The maximum wind speed, u_m is assumed to occur during the prescribed time interval Δt_m when deep cumulus convection is present. This time increment is prescribed to be 2 days,

From the results shown in Fig. 2 the existence of the hydrologic cycle operating in this simple atmosphere-ocean system is clearly evident. Through the processes of evaporation and precipitation, which are constrained by the moisture tolerance and its implied conditional instability, the hydrologic cycle is naturally introduced in this system. Furthermore, through a comparison of these two results, we see that the presence of this cycle is independent of the detailed structure of the low level wind. This independence suggests that the oscillation in the low level wind field may be considered a consequence of the hydrologic cycle. Since the time evolution of the heating profile in the tropical troposphere is directly related to the different phases of the hydrologic cycle, this cycle provides an external heat/energy source for the atmosphere. This source disturbs the energy state of the tropical atmosphere to which the wind and mass fields of the atmosphere then adjust. Thus this hydrologic cycle is a plausible mechanism for initiating oscillations of similar frequency in wind and mass fields in the tropical atmosphere. The influence of the varying low level wind field on the frequency of the hydrologic cycle is also noticeable in Fig. 2, although it is does not determine the existence of the cycle *per se*.

Results of model integrations with different model parameters are presented in Fig. 3. These results were obtained with the same low level winds as used to produce Fig. 2b. A significant characteristic shown in this figure, is that the period of the resultant hydrologic cycle in this system increases with increasing model SST. This result is consistent with the observation that low frequency oscillations are preferred in regions of warmest SSTs (Webster, 1987).

The model sensitivities to different low level wind speeds and values of precipitation rate are also illustrated in Fig 3.

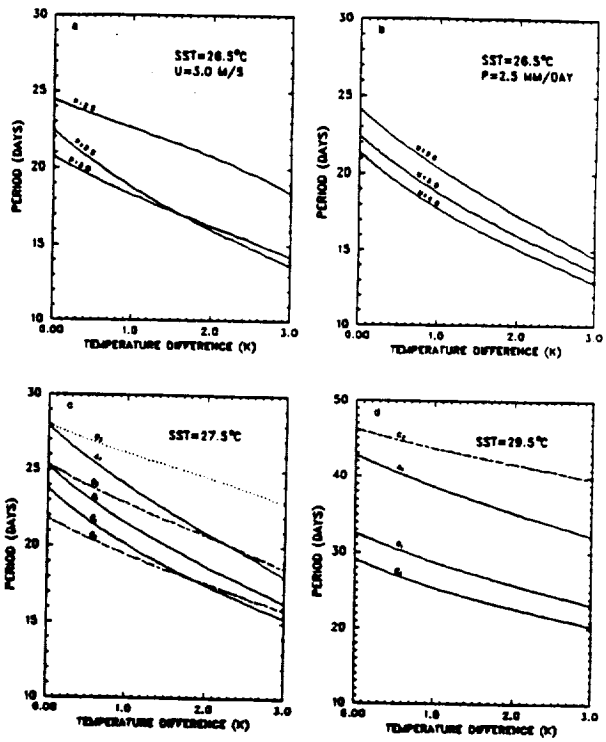

Fig. 3: Predicted period of hydrologic circulation with different model conditions. The abscissa shows the temperature difference between the ocean and the atmosphere. (a) and (b) show the model sensitivities to the changes in precipitation rate P [unit: mm/day] and the model low level wind u, [unit: m/s], respectively. In (c) and (d), the 3 groups of results, e.g. A_i, B_i and C_i are for 3 different P's used in the model, i.e. 2.5, 3.0 and 3.5 mm/day. The subscript i, from 1 to 3, stands for different low level wind conditions of 2.0, 3.0 and 4.0 m/s. Lines are not plotted in (c) and (d) when a balance between E and P is the case and therefore no oscillation occurs.

4. COUPLED INTERACTIVE ATMOSPHERE-OCEAN MIXED LAYER MODEL

The existence of the hydrologic cycle and its relationship to the low frequency oscillation in the tropical troposphere have been shown by the one-way interaction model (hereafter MD1) of Section 3. Since a fixed SST was applied in MD1, the question of how this cycle as well as its time scale is influenced by a time varying SST still remains. In this section we address some aspects of this issue.

a) The Model

The model structure and the major physical processes are schematically illustrated in Fig. 4. As in MD1, we focus on the thermodynamics of this atmosphere-ocean system and ignore any detailed dynamics. The model's ocean mixed layer process follows that in Kraus and Turner (1967), and Denman (1973)

In this model to incorporate in the model SSTs which vary in time, a detailed energy budget in the ocean mixed layer is required. As the only energy source in this budget, the input solar energy at the ocean surface needs to be included. This input further varies with presence or absence of cumulus convections through cloud-solar radiation interaction. On the other hand, the energy losses through infrared radiation (IR) from ocean surface, and sensible and latent heat exchanges with the atmosphere are also considered. Since explicit prediction of key processes, such as cloud generation and interaction of clouds with solar radiation, is beyond the scope of this mechanistic study, we parameterize their effects. To express the cloud influence on the solar radiation, for example, we assume different values of the solar irradiance at the surface under varying convective cloud cover conditions. These values are obtained from observations and theoretical studies. A similar method is also applied to represent the IR cooling process. The main reason for neglecting the detailed treatment of these processes is to avoid the uncertainties associated with complex processes involving multiple scales, some of which are poorly understood, and therefore to concentrate more on the basic physical mechanisms.

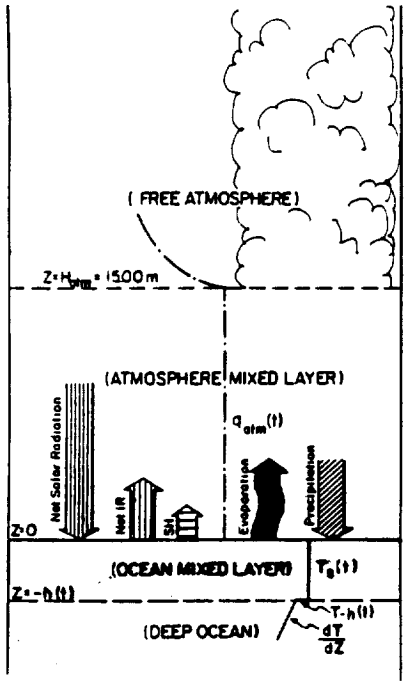

Fig. 4: Schematic structure of the fully coupled atmosphere-ocean mixed layer model (MD2).

In the model atmosphere, the process is similar to MD1. The moisture amount transferred into the model atmospheric mixed layer is calculated again using the bulk aerodynamic formula

$$E(t) = \rho_a C_D |u_s(t)| (q_{sat}[T_s(t)] - q_{atm}(t)). \qquad (5)$$

Here, $q_{sat}[T_s(t)]$ is time dependent as SST varies with time in this model. A Bowen ratio of 0.2 is used to obtain the value of the sensible heat flux required as an input to the ocean model.

The solar irradiance at the ocean surface are specified by the step function

$$R_{sw} = \begin{cases} R^n_{sw}, & \text{non-convective;} \\ R^c_{sw}, & \text{convective.} \end{cases} \qquad (6)$$

The values in (6) are based upon the satellite and observational data analyses by Gautier and Katsaros (1984), Gautier (1986) and Gautier (1988). With these values, the bulk features of the influence of deep cumulus convection on the solar radiation transfer in the atmosphere have been included. Likewise the step function for IR change is

$$R_{IR} = \begin{cases} R^n_{IR}, & \text{non-convective;} \\ R^c_{IR}, & \text{convective,} \end{cases} \qquad (7)$$

where the values for R^n_{IR} and R^c_{IR} are based on a study by Stephens *et al.* (1981).

b) Model Results

Table 1 lists some of the model experiments we conducted. The physical parameters, their values, and the model predicted quantities are included in this table.

Since only thermodynamic and turbulent mixing processes in the two mixed layers are considered, only a few of these experiments reach a steady or an equilibrium state through the period of integration. Fig. 5 shows the result from one of the experiments (experiment 1 in Table 1) in which an equilibrium state has been reached. From this figure we see that the oscillation of the extra water content in the atmospheric mixed layer still experienced when the model has varying SST. This oscillation, through the coupling and feedback with the solar radiation and hence the surface energy process, influences the processes in the ocean mixed layer (Figs. 5b,c and d). The time scale of these oscillations predicted by the model is 33 days.

As we have discussed in Section 2, in the process of the hydrologic circulation a pulsating energy disturbance is released in the convection phase. This disturbance then causes dynamic perturbations in the atmospheric momentum and mass fields (Salby and Garcia, 1987). The observed oscillation in the atmospheric relative angular momentum (Anderson and Rosen, 1983) may also be related with this pulsating energy disturbance. On the other hand, this energy disturbance, in addition to the change in the solar energy input, affects the energy budget of the ocean mixed layer. As a consequence of the hydrologic circulation in the atmosphere-ocean system, the 30-60 day oscillations therefore appear in both the tropical atmosphere and ocean.

Because the thermodynamic processes depend on SST in a highly nonlinear fashion, the results illustrated in Table 1 differ from those obtained from MD1. In Fig. 3, a higher SST in the one-way model causes a dramatic increase in the period of the model's hydrologic circulation. Results from the fully coupled model, however, are not as simple. Using 29^oC as the initial SST, the hydrologic cycle reaches a steady period of 35 days (experiment 2 in Table 1). This period is quite close to that predicted in experiment 1 where the initial SST is 28^oC. However when a colder SST is used to start the model run, the predicted result are distinctly different (Fig. 6).

Results presented in Table 1 also show the model sensitivity to other model parameters.

5. ONE-DIMENSIONAL GCM AND RESULTS

To test our hypothesis in a more complete manner different experiments have also been conducted with the one-dimensional version of the UCLA/CSU GCM (Randall and Dazlich, 1989). This 1-D model includes the full radiation and moist physics parameterization of the GCM, and is coupled to a slab of ocean of fixed depth. The slab ocean does not exchange energy with deeper ocean layers; its temperature is controlled entirely by the surface energy flux.

At this stage some very preliminary results from experiments with this 1-D GCM model have been obtained and are shown in Figs. 7 and 8. These results support the major findings from our previous conceptual models. When run with a ocean slab depth of $60m$, the model produces obvious oscillation of sea surface temperature, with amplitude 0.4^oC and a period of 60 days (Figs. 7a and 8a). This oscillation is accompanied by 60-day fluctuations of the surface energy flux, precipitation rate and cloudiness (Figs. 7b, 7c and 8b). The changes in the surface energy flux are due to changes in the absorbed solar radiation, which are controlled by the cloudiness fluctuations or model convections.

During the warming phase of the oscillation, the sea surface temperature and the convective precipitation rate gradually increase. Eventually the cloudiness increases to the point that the solar radiation absorbed by the ocean is reduced, allowing the ocean to begin cooling. This cooling is followed by a reduction in the model convective activity, which leads to a reduction in the cloudiness. The absorbed solar radiation then increases, and the model hydrologic cycle is re-initiated.

Table 1: Model Experiments and Results – Among the output quantities, τ is the predicted period of the model hydrological circulation. Σq is the maximum extra water amount accumulated in the model atmosphere before convection starts. ΔT and Δh are respectively the amplitudes of changes in the SST and depth of ocean mixed layer in a hydrological circulation. When a steady state is not reached in a model run, these quantities are given from a nominal cycle in model integration.

Physical Parameter	Experimental Value					
	1	2	3	4	5	6
$R^n_{SW}\,(W/m^2)$	250	250	250	250	250	260*
$R^e_{SW}\,(W/m^2)$	120	120	120	120	120	105*
$R^n_{LR}\,(W/m^2)$	40	40	40	40	40	40
$R^e_{LR}\,(W/m^2)$	40	40	40	40	40	40
u_s : $(u_b, u_m, \Delta t_d)$	(2, 12, 13.0)	(2, 12, 13.0)	(2, 12, 13.0)	(2, 12,11.5*)	(2, 12, 15.0*)	(2, 12, 13.0)
$P\,(mm/day)$	2.5	3.0*	2.5	2.5	2.5	2.5
$T_s(t=0)(°C)$	28.0	29.0*	26.0*	28.0	28.0	28.0
$T_{-h}(t=0)(°C)$	25.0	26.0*	23.0*	25.0	25.0	25.0
Output Quantity	Model Predicted Result					
τ (days)	33	35	the 5th: 23 the 9th: 15	the 5th: 33 the 20th: 37	the 5th: 33 the 20th: 26	31
$\Sigma q\,(cm/m^2)$	1.49	1.51	the 9th: 0.35	the 20th: 1.70	the 20th: 0.80	1.40
$\Delta T_s(°C)$	1.68	1.63	the 9th: 0.83	the 20th: 1.67	the 20th: 1.41	1.83
$\Delta h(m)$	21.85	21.39	the 9th: 13.51	the 20th: 21.48	the 20th: 19.50	24.93

*: Parameter value different from that in the controlled experiment (experiment 1).

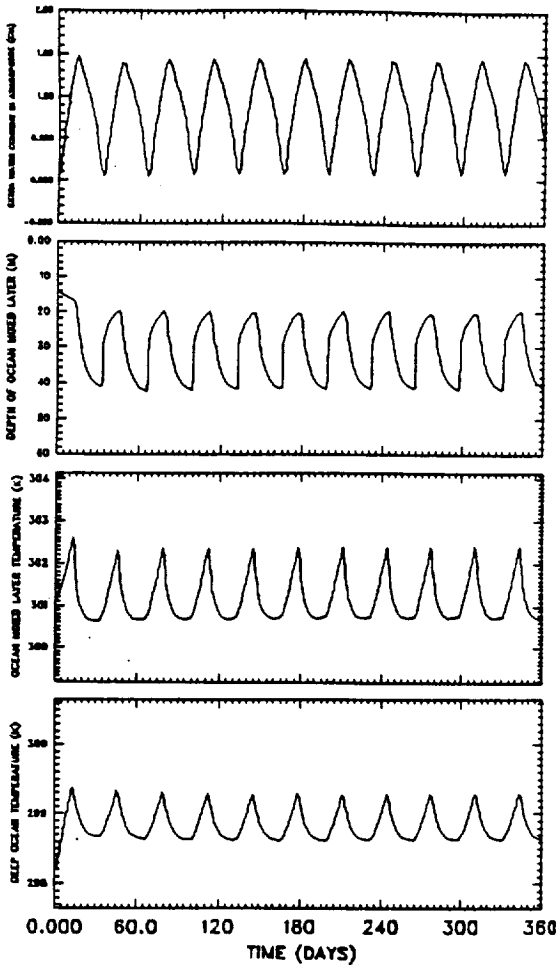

Fig. 5: Model results from experiment 1 in Table 1.

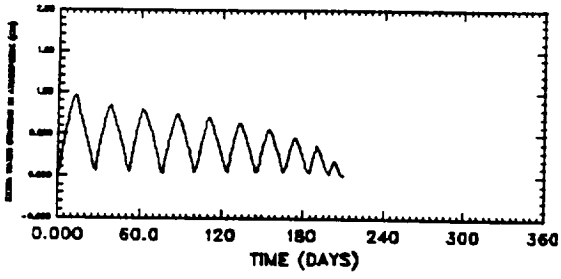

Fig. 6: Temporal variation of the extra water content in the model atmosphere from experiment 3 in Table 1.

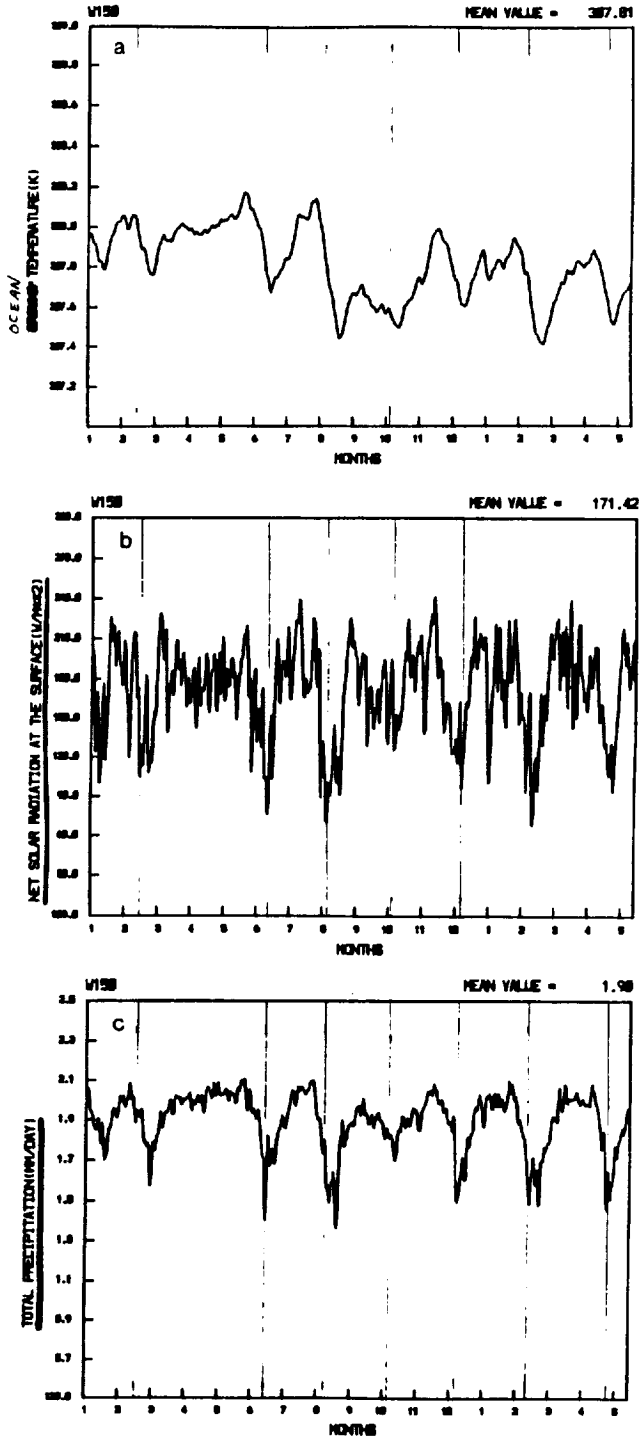

Fig. 7: Temporal variations of (a) SST, (b) solar radiation absorbed at the ocean surface, and (c) daily precipitation from the 1-D GCM.

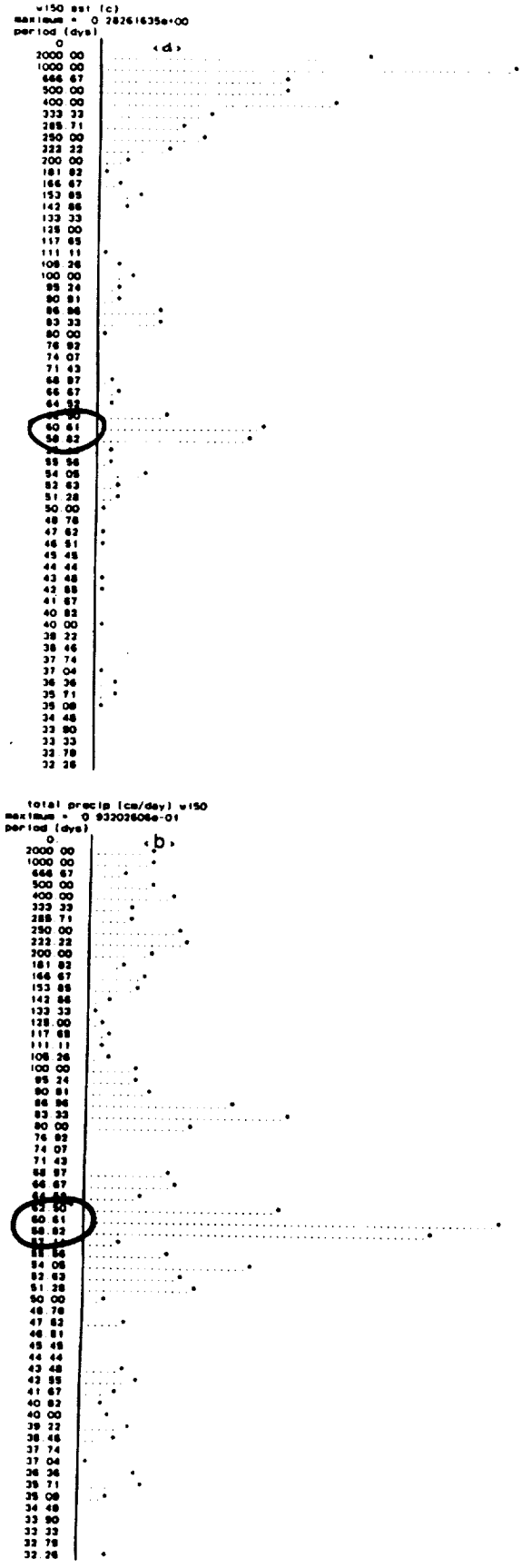

Fig. 8: Square of the amplitudes of the Fourier harmonics of (a) model SST, and (b) model precipitation. Peaks at about 60 days are outstanding.

6. CONCLUDING REMARKS

In this study we have shown that the 30-60 day oscillations in the tropical atmosphere and ocean can result from the hydrologic circulation in a coupled atmosphere-ocean system. This circulation is intrinsic to this system and is a consequence of the energy exchange and energy balance in this system.

The time scale of this circulation can be determined in a simple coupled atmosphere-ocean model when the role of moisture played in the atmosphere is incorporated in the model. By parameterizing this role in terms of the 'model atmospheric moisture tolerance' in our conceptual models we showed that the hydrologic cycle is spontaneously carried on in the tropical atmosphere-ocean system. Its existence was basically independent of the variations of the low level wind.

Our hypothesized relationship between the hydrologic circulation and the intraseasonal oscillation in the tropical atmosphere and ocean was also examined in a 1-D GCM. The model results were positive in supporting this relationship. Meanwhile, the analysis of the thermodynamic process in the 1-D GCM illustrated the mechanism we proposed.

Based on our results we conclude that the hydrologic cycle in the tropical atmosphere-ocean system is fundamental to the observed intraseasonal oscillations in the tropics. The physical restriction of the accumulation of latent heat in the lower tropical troposphere and the reduction of the source supply of energy to the tropical atmosphere-ocean system, through cloud-solar radiation interaction, are crucially important to the presence and time scale of this hydrologic cycle.

7. ACKNOWLEDGMENTS

We would like to thank Ms. Gail Cordova for preparing this manuscript and Ms. Judy Sorbie for drafting the schematic figures. This research has been supported by the National Science Foundation under grant ATM-8609731 to Colorado State University. Computations were carried out on the computers at the National Center for Atmospheric Research, which is also sponsored by the National Science Foundation.

8. REFERENCES

Anderson, J.R., and R.D. Rosen, 1983: The latitude–height structure of 40– 50 day variations in atmospheric angular momentum. *J. Atmos. Sci.*, 40, 1584–1591.

Anderson, J.R. and D.E. Stevens, 1987: The presence of linear wavelike modes in a zonally symmetric model of the tropical atmosphere. *J. Atmos. Sci.*, 44, 2115–2127.

Anderson, J.R. and D.E. Stevens, 1987: The response of the tropical atmosphere to low–frequency thermal forcing. *J. Atmos. Sci.*, 44, 676–686.

Chang, C.-P., and H. Lim, 1988: Kelvin Wave–CISK: A possible mechanism for the 30–50 day oscillations. *J. Atmos. Sci.*, 45, 1709–1720.

Denman, K.L., 1973: A time–dependent model of the upper ocean. *J. Phys. Oceanogr.*, 3, 173–184.

Emanuel, K.A., 1987: An air–sea interaction model of intraseasonal oscillations in the tropics. *J. Atmos. Sci.*, 44, 2324–2340.

Enfield, D.B., 1987: The intraseasonal oscillation in eastern Pacific sea levels: How is it forced? *J. Phys. Oceanogr.*, **17** 1860–1876.

Gautier, C., 1986: Evolution of the net surface short wave radiation over the Indian ocean during summer MONEX (1979): A satellite description. *Mon. Wea. Rev.*, **114**, 525–533.

Gautier, C. and K. Katsaros, 1984: Insoluation during STREX. Part I: Comparisons between surface measurements and satellite estimates. *J. Geophys. Res.*, **89**, 11779–11788.

Gautier, C., 1988: Surface solar radiance in the central Pacific during Tropic Heat: Comparisons between *in situ* measurements and satellite estimates. *J. Climate*, **1**, 600–608.

Gill, A.E., 1982: Studies of moisture effects in simple atmospheric models: the stable case. *Geophys. Astrophys. Fluid Dynamics*, **19**, 119–152.

Hartmann, D.L., and J.R. Gross, 1988: Seasonal variability of the 40–50 day oscillation in wind and rainfall in the tropics. *J. Atmos. Sci.*, **45**, 2680–2702.

Kraus, E.B., and J.S. Turner, 1967: A one–dimensional model of the seasonal thermocline II: The general theory and its consequences. *Tellus*, **19**, 98-106.

Krishnamurti, T.N., D.K. Oosterhof, and A.V. Mehta, 1988: Air–sea interaction on the time scale of 30–50 days. *J. Atmos. Sci.*, **45**, 1304–1322.

Kuo, H.-L., 1975: Instability theory of large–scale disturbances in the tropics. *J. Atmos. Sci.*, **32**, 2229–2245.

Lau, K.M., and L. Peng, 1987: Origin of low–frequency (intraseasonal) oscillations in the tropical atmosphere. Part I: Basic theory. *J. Atmos. Sci.*, **44**, 950–972.

Madden, R., and P.R. Julian, 1971: Detection of a 40–50 day oscillation in the zonal wind in the tropical Pacific. *J. Atmos. Sci.*, **28**, 702–708.

Madden, R., and P.R. Julian, 1972: Description of global–scale circulation cells in the tropics with a 40–50 day period. *J. Atmos. Sci.*, **29**, 1109–1123.

Matsuno, T., 1966: Quasi–geostrophic motions in the equatorial area. *J. Meteor. Soc. Japan*, **44**, 25–42.

Mitchum, G.T., and R. Lukas, 1987: The latitude–frequency structure of Pacific sea level variance. *J. Phys. Oceanogr.*, **17**, 2362–2365.

Murakami, T., L. Chen and A. Xie, 1986: Relationship among seasonal cycles, low–frequency oscillations, and transient disturbances as revealed from outgoing longwave radiation data. *Mon. Wea. Rev.*, **114**, 1456–1465.

Neeling, J.D., I.M. Held and K.H. Cook, 1987: Evaporation–wind feedback and low–frequency variability in the tropical atmosphere. *J. Atmos. Sci.*, **44**, 2341– 2348.

Ooyama, K., 1969: Numerical simulation of the life cycle of tropical cyclones. *J. Atmos. Sci.*, **26**, 3–40.

Randall, D. A. and D. Dazlich, 1989: The *CSU* general circulation model: *A user's guide*. informal manuscript.

Reed, R.J. and E.E. Recker, 1971: Structure and properties of synoptic–scale wave disturbances in the equatorial western Pacific. *J. Atmos. Sci.*, **28**, 1117–1133.

Riehl, H., and J.S. Malkus, 1958: On the heat balance in the equatorial trough zone. *Geophysica*, **6**, 3–4.

Risby, J.S., and P.H. Stone, 1988: Observations of the 30–60 day oscillation in zonal mean atmospheric angular momentum and high cloud cover. *J. Atmos. Sci.*, **45**, 2026–2038.

Salby, M.L., and R.R. Garcia, 1987: Variations induced by interference of stationary and traveling planetary waves. *J. Atmos. Sci.*, **44**, 2679–2711.

Stephens, G.L., G.G. Campbell and T.H. Vonder Haar, 1981: Earth radiation budgets. *J. Geophys. Res.*, **86**, C10, 9739–9760.

Stevens, D.E. and R.S. Lindzen, 1978: Tropical wave CISK with a moisture budget and cumulus friction. *J. Atmos. Sci.*, **35**, 940-961.

Wang, B., 1988: Dynamics of tropical low-frequency waves: An analysis of the moist Kelvin wave. *J. Atmos. Sci.*, **45**, 2051-2065.

Webster, P.J., 1987: The role of hydrological processes in ocean–atmosphere interaction. USTOGA 8, 71–100.

Yamagada, T., and and Y. Hayashi, 1984: A simple diagnostic model for the 30–50 day oscillation in the tropics. *J. Meteor. Soc. Japan*, **62**, 709–717.

Yasunari, T., 1980; A quasi–stationary appearance of 30–50 day period in the cloudiness fluctuations during the summer monsoon over India. *J. Meteor. Soc. Japan*, **58**, 225–229.

APPENDIX B

N15

RESEARCH TRIANGLE INSTITUTE

RTI Project Number: 472U-4452
November 1990

Second Year Final Report

Linear and Nonlinear Aspects of the Tropical 30-60 Day Oscillation; A Modelling Study

Prepared for

Colorado State University
Department of Atmospheric Science
Fort Collins, Colorado 80523

Attention: Dr. Graeme Stephens

Prepared by

Dr. Adel F. Hanna
Atmospheric & Marine Program
Research Triangle Institute
Post Office Box 12194
Research Triangle Park, N. C. 27709
(919) 541-6408

SUMMARY

Research Triangle Institute (RTI) is a subcontractor to Colorado State University (CSU) on the National Aeronautics and Space Administration (NASA) project "Linear and Nonlinear Aspects of the Tropical 30-60 Day Oscillation: A Modelling Study," contract number NAG5-1122. The proposed three year program started in March 1989 and will conclude in February 1992. In this integrated program, RTI has to develop a 5-level general circulation model (year 1 and 2) and design numerical experiments to analyze the model simulation of the 30-60 day oscillation (year 3). During the second year of the project (March 1990 - February 1991) RTI completed the development of the 5-level general circulation model. Specific tasks that have been accomplished during this year are:

1. Test the time difference method used for model integration;
2. Design the radiation scheme that is used in the model;
3. Develop test runs for the model simulation for the month of January (Northern Hemisphere winter).

RTI principal investigator, Dr. Adel Hanna has maintained full interaction with the co-principal investigators, Dr. Graeme Stephens, CSU and Dr. Duane Stevens, University of Hawaii (UH). Also, he has established scientific cooperation with Dr. James Hack of the National Center for Atmospheric Research (NCAR), who is responsible for developing the next generation of the Community Climate Model (CCM).

Table of Contents

List of Figures

1.0 INTRODUCTION

Modelling analyses provide an appropriate tool to understand atmospheric circulation especially on a global scale where the observational network is not dense enough to account for all the scales of atmospheric interactions. The intraseasonal (30-60 day) oscillation has received a great deal of attention due to its possible impact on global climate change as an intrinsic mode of the atmospheric interannual variability. Both observational and modelling studies of the intraseasonal oscillation have proven to be useful in identifying the origin of its structure. The oscillation is mainly driven by nonlinear wave interaction of the Rossby and Kelvin waves in the atmosphere. These waves are excited by the latent heat release associated with intense convective systems over the tropical oceans. On the other hand the latter is influenced by the sea-surface temperature pattern.

This research project is an integrated program to study the linear and nonlinear aspects of the 30-60 day oscillation. The nonlinear dynamics are investigated through the analysis of a five level primitive equation global climate model. The model is of medium complexity structure to understand and isolate specific components of the atmospheric circulation. However it includes the forcing mechanisms and physics to stimulate the large scale atmospheric circulation and seasonal cycle through interactions of orographic forcing, radiative heating, convective and nonconvective release of latent heat. The development of the model in both the finite difference and spectral forms gives the opportunity to study the interactions between different wave numbers and also the effect of spectral truncation on model simulation. For example, one of the questions of basic interest to this study is the relationship between zonal asymmetrics (especially wave number 1) and zonally symmetric mode (wave number 0) in producing energetics necessary for maintaining the oscillation.

This report represents a description of the 5-level general circulation model. It also includes a description of the projected experiment using the model.

2.0 SYSTEM OF EQUATIONS

The 5-level primitive equation model has been developed. The atmospheric model is global using sigma ($=p/p_s$) as the vertical coordinate. The horizontal model resolution is spectral using spherical harmonics rhomboidal truncation at wave number 15. The prognostic variables are the stream function (Ψ), the velocity potential (χ), surface pressure (p_s), temperature (T), and the mixing ratio (q). The stream function (ψ) and velocity potential (χ) are expressed in Laplacian forms (vorticity- ζ, and divergence - δ). Diagnostic variables are the geopotential height (Φ), and the vertical velocity ($\dot{\sigma}$). The following system of equations represents the basic equations for the 5-level atmospheric model (see for example, Bourke, 1974; Haltiner and Williams, 1980).

$$\frac{\partial}{\partial t}\zeta = -\alpha\,(A,B) \tag{2.1}$$

$$\frac{\partial}{\partial t}\,\delta = \alpha\,(B,-A) - \nabla^2\,(E + \Phi' + RT_o\,l_s) \tag{2.2}$$

$$\frac{\partial T'}{\partial t} = -\,\alpha\,(UT', VT') + T'\,\delta + \dot{\sigma}\left(\frac{RT}{\sigma c_p} - \frac{\partial T}{\partial \sigma}\right) + \frac{RT}{c_p}\left(G - \overline{G} - \overline{\delta}\right) + \frac{\dot{Q}}{c_p} + Di_T \tag{2.3}$$

$$\frac{\partial l_s}{\partial t} = -\left(\overline{\delta} + \overline{G}\right) \tag{2.4}$$

$$\frac{\partial q}{\partial t} = -\,\alpha\,(Uq, Vq) + q\delta - \dot{\sigma}\frac{\partial q}{\partial \sigma} + M + Di_q \tag{2.5}$$

$$\dot{\sigma} = \left(\overline{\delta} + \overline{G}\right)\sigma - \int_0^{\sigma} (\delta + G)\,d\sigma \tag{2.6}$$

$$\frac{\partial \Phi}{\partial \sigma} = \frac{-RT}{\sigma} \tag{2.7}$$

where

$$\sigma = \frac{P}{p_s}, \tag{2.8}$$

$$l_s = \ln p_s, \tag{2.9}$$

$$U = u\cos\phi, \quad V = v\cos\phi, \tag{2.10}$$

$$G = \frac{U}{a\cos^2\phi}\frac{\partial l_s}{\partial \lambda} + \frac{V}{a\cos\phi}\frac{\partial l_s}{\partial \phi} \tag{2.11}$$

$$\alpha(A,B) = \frac{1}{a\cos^2\phi}\frac{\partial A}{\partial \lambda} + \frac{1}{a\cos\phi}\frac{\partial B}{\partial \phi}, \tag{2.12}$$

$$A = (\zeta + f)\,U + \dot{\sigma}\frac{\partial V}{\partial \sigma} + \frac{RT'}{a}\cos\phi\frac{\partial l_s}{\partial \phi} - \frac{g}{p_s}\frac{\partial \tau_y}{\partial \sigma}, \tag{2.13}$$

$$B = (\zeta + f)\,V - \dot{\sigma}\frac{\partial U}{\partial \sigma} - \frac{RT'}{a}\frac{\partial l_s}{\partial \lambda} + \frac{g}{p_s}\frac{\partial \tau_x}{\partial \sigma}, \tag{2.14}$$

$$E = \left(U^2 + V^2\right) / \left(2\cos^2\phi\right). \qquad 2.15$$

The zonal velocity, u, and the meridional velocity, v, are calculated using the stream function and velocity potential. The diabatic heating rate, $\dot{Q}$, and moisture source, M, are calculated using surface (land and ocean) and atmospheric fluxes. Other parameters in the above system of equations are: E - the Kinetic energy; f - the coriolis parameter; ϕ - the latitude angle; Cp - the specific heat; R - the gas constant; τ_x and τ_y - the horizontal stresses; g - the acceleration of gravity; a - the radius of the earth; and Di - the diffusion of appropriate parameters. The overbar presents the vertical integration through the depth of the model atmosphere, or from the top of the model atmosphere (σ=0) to surface σ=1. The prime presents the deviation from the horizontal average defined by the subscript 0. The temperature (T') and geopotential (ϕ') fields are expressed in the form of a departure from the horizontal average in order to apply a semi-implicit time-differencing scheme.

3.0 HORIZONTAL TRUNCATION: SPECTRAL METHOD

The horizontal representation of the dependent variables is in terms of a truncated series using spherical harmonics as basis functions. Nonlinear terms are transformed to the spectral space using the full transform method. The variables are expanded in the form

$$\zeta = \sum_{m=-M}^{M} \sum_{n=|m|}^{|m|+J} \zeta_n^m \; Y_n^m \; (\lambda,\mu) \qquad 3.1$$

$$\delta = \sum_{m=-M}^{M} \sum_{n=|m|}^{|m|+J} \delta_n^m \; Y_n^m \qquad 3.2$$

$$T = \sum_{m=-M}^{M} \sum_{n=|m|}^{|m|+J} T_n^m \; Y_n^m \qquad 3.3$$

$$l_s = \sum_{m=-M}^{M} \sum_{n=|m|}^{|m|+J} (l_s)_n^m \; Y_n^m \qquad 3.4$$

$$q = \sum_{M=-M}^{M} \sum_{n=|m|}^{|m|+J} q_n^m \, Y_n^m \qquad 3.5$$

$$U = \sum_{m=-M}^{M} \sum_{n=|m|}^{|m|+J} U_n^m \, Y_n^m \qquad 3.6$$

$$V = \sum_{m=-M}^{M} \sum_{n=|m|}^{|m|+J} V_n^m \, Y_n^m \qquad 3.7$$

$$\Phi = \sum_{m=-M}^{M} \sum_{n=|m|}^{|m|+J} \Phi_n^m \, Y_n^m \qquad 3.8$$

$$G = \sum_{m=-M}^{M} \sum_{n=|m|}^{|m|+J} G_n^m \, Y_n^m \qquad 3.9$$

$$\alpha = \sum_{m=-M}^{M} \sum_{n=|m|}^{|m|+J} \alpha_n^m \, Y_n^m \qquad 3.10$$

$$E = \sum_{m=-M}^{M} \sum_{n=|m|}^{|m|+J} E_n^m \, Y_n^m \qquad 3.11$$

where $(\,)_n^m$ identify the harmonic coefficients, λ is longitude, μ is the sine of latitude, m is the zonal wave number, n - |m| is a meridional wave number, M is the highest zonal wave number retained in the truncated series, and J is the highest value of n - |m| retained in the truncated series. Y_n^m are spherical harmonic function defined by

$$Y_n^m = P_n^m \, (\mu) \, e^{im\lambda}, \qquad 3.12$$

where P_n^m are the associated legendre functions of the first kind.

The horizontal truncation using the spectral method gives the model flexible efficiency in terms of using different zonal wave numbers to test different horizontal resolutions and the interaction between the basic flow and certain wave numbers. In the current program we assume

rhomboidal truncation at wave number 15, with 40 Gaussian latitudes and 64 longitude grid points at each latitude.

The rotated zonal wind U and meridional wind V components, are diagnosed from the stream function and velocity potential harmonics using the forms;

$$U_n^m = (n-1)\,\rho_n^m\,\psi_{n-1}^m - (n+2)\,\rho_{n+1}^m\,\psi_{n+1}^m + i\,m\,\chi_n^m, \qquad 3.13$$

$$V_n^m = -(n-1)\,\rho_n^m\,\chi_{n-1}^m + (n+2)\,\rho_{n+1}^m\,\chi_{n+1}^m + i\,m\,\psi_n^m \qquad 3.14$$

where

$$\rho_n^m = \sqrt{\frac{n^2 - m^2}{(4n^2 - 1)}}$$

4.0 VERTICAL FINITE DIFFERENCE AND INTEGRATION

In the vertical, the variables are staggered in σ in such a way to calculate vertical derivatives and the vertical velocity, $\dot{\sigma}$ between layers (Figure 1). Levels 1 to 5 are located at layer midpoints.

Vertical advection terms of momentum, temperature, and moisture at level k is calculated using the form

$$\left(\dot{\sigma}\frac{\partial U}{\partial \sigma}\right)_k = \frac{\sigma_{k+1} - \sigma_k}{2\Delta\sigma_k}\,\dot{\sigma}_{k+\frac{1}{2}}\left[\frac{U_{k+1} - U_k}{\sigma_{\kappa+1} - \sigma_\kappa}\right] + \qquad 4.1$$

$$\frac{\sigma_k - \sigma_{k-1}}{2\Delta\sigma_k}\,\dot{\sigma}_{k-\frac{1}{2}}\left[\frac{U_k - U_{k-1}}{\sigma_k - \sigma_{k-1}}\right]$$

where,

$$\Delta\sigma_k = \sigma_{k+\frac{1}{2}} - \sigma_{k-\frac{1}{2}}\,. \qquad 4.2$$

The vertical velocity is zero at the top and surface levels of the model's atmosphere,

$$\dot{\sigma}_{\frac{1}{2}} = \dot{\sigma}_{K+\frac{1}{2}} = 0. \qquad 4.3$$

In Finite difference form, the vertical velocity $\dot{\sigma}$ (equation 2.6) is given by

$$\dot{\sigma}_{k+\frac{1}{2}} = \sigma_{k+\frac{1}{2}} \sum_{j=1}^{K} \left(\delta_j + V_j \bullet \nabla \ln P_s\right) \Delta\sigma_j - \sum_{j=1}^{k} \left(\delta_j + V_j \nabla \ln P_s\right) \Delta\sigma_j \quad 1 \le k \le K - 1 \qquad 4.4$$

where K is the number of levels (K=5), and

$$\delta_j = \left(\nabla^2 \chi\right)_j \qquad 4.5$$

5.0 PARAMETERIZATION OF PHYSICAL PROCESSES

The diabatic heating rate, $\dot{Q}$, is a composite of the radiative heating, latent heating, and surface heat fluxes as boundary interchange between the surface (ocean and land) and the atmosphere.

The surface heat and moisture fluxes are calculated using a bulk aerodynamic formula. The surface sensible heat flux (Q_s) is given by:

$$Q_s = \rho_s C_p C_d | V_s | \left(T_g - T_5\right) \qquad 5.1$$

where T_5 is the air temperature at level 5, ρ_s is the density of air, $| V_5 |$ is the windspeed, and C_d is the drag coefficient. Ground temperature T_g over land is determined from the surface energy balance, whereas on the ocean T_g is specified from climatological values.

The evaporation from the surface to the lower layer of the atmospheric model is given by:

$$E_v = \rho_s C_d | V_5 | GW \left[q_s(T_g) - h_s q_s(T_5)\right], \qquad 5.2$$

where h_S is a measure of the relative humidity in the lower layer, q_S is the saturation mixing ratio and GW is a wetness parameter that is equal to unity on water surface.

The amount of latent heat lost from the surface due to evaporation is given by:

$$Q_e = L E_v \ , \qquad 5.3$$

where L is the latent heat of condensation.

5.1 LARGE-SCALE CONDENSATION AND CONVECTIVE ADJUSTMENT

The convective adjustment method used in the model follows the algorithm developed by Manabe et al., (1965). Each level is tested for supersaturation and hydrostatic stability. Excess moisture in layers which are stable and supersaturated is condensed as large-scale precipitation with release of latent heat in the layer. Supersaturated and convectively unstable

layers are adjusted in such a way to conserve moist static energy through the release of latent heat and the vertical transfer of heat and moisture to the successive layers aloft. The procedure and tests for convective adjustments are explained in the following;

a) Large-scale condensation only

$$r \geq 1 \qquad \frac{\partial T}{\partial \sigma} \leq P_s \gamma_m$$

$$q+\delta q = q_s(T+\delta T, \sigma) \tag{5.4}$$

$$c_p \delta T + L\delta q = 0$$

b) Moist convection and large-scale condensation

$$r \geq 1 \qquad \frac{\partial T}{\partial \sigma} > P_s \gamma_m$$

$$\frac{\partial \theta_e}{\partial \sigma}(T+\delta T, q+\delta q, \sigma) = 0, \tag{5.5}$$

$$q + \delta q = q_s(T+\delta T, \sigma)\ , \tag{5.6}$$

$$\int_0^1 \left(c_p \delta T + L\delta q\right) d\sigma = 0. \tag{5.7}$$

where r is the relative humidity, γ_m is the moist adiabatic lapse rate, δq, and δT are the adjustments to water vapor mixing ratio, and temperature respectively.

The atmospheric moisture, in the model, is described in terms of the water vapor mixing ratio, q, (Equation 2.5). In physical space, this quantity is non-negative by definition. However, when using the spectral method the finite truncation in wave-number space generates negative values when transformed back to physical space. This misrepresentation is known in Fourier analysis as Gibbs phenomenon. Various formulations of the moisture equation using other required positive variables, such as the relative humidity, are also having the same problem of transformed negative values in the physical space. To overcome this problem, some spectral models are using the vertical borrowing method to augment the negative values to zeros. However, if there is no available moisture in the upper levels of the model, these negative values are simply increased to zeros. This procedure causes a spurious source of water vapor that affects the model's global moisture budget. Royer (1986) has suggested a method based on horizontal, borrowing in such a way to maintain the conservation of the global moisture. The horizontal and vertical moisture borrowing methods are used in the 5-level model simulation.

5.2 SOLAR RADIATION

The calculation of radiative energy of the model is similar to the one described by Hanna and Stevens (1984). The incoming solar radiation at the top of the model's atmosphere is calculated as a function of daily mean zenith angle (Wetherald and Manabe, 1972). The albedo of the atmosphere r_a, is calculated, taking into consideration the observed zonal mean amount of clouds.

The solar radiation absorbed by the atmosphere, S_r, is given by:

$$S_r = x\,(1 - r_a)\,S, \tag{5.8}$$

where x is the absorptivity of the atmosphere, and S is the incoming of solar radiation at the top of the atmosphere.

The net solar radiation absorbed by the earth's surface (land or ocean) is given by:

$$S_s = (1 - x)\,(1 - r_a)(1 - r_s)\,S, \tag{5.9}$$

where r_s is the albedo of the earth's surface. Over the oceans, r_s is assigned to .1, while over the continent, it is assumed to be a value between .1 and .8, depending on the type of surface (Gates, 1975).

5.3 LONG-WAVE RADIATION

The calculation scheme of the longwave radiation cooling rates of the atmosphere uses empirical longwave radiative emissivities calculated from climatological monthly mean humidities, cloudiness, and cooling rates and the model simulated temperature (Corby et al., 1977).

The net flux of longwave radiation in the atmosphere is given by:

$$c\left(\frac{\partial T}{\partial t}\right)_{Lw} = -\varepsilon B T^4, \tag{5.10}$$

where c is the heat capacity of the atmospheric layer, B is the Stefan Boltzmann constant and ε is the longwave emissivity.

The longwave emissivities at each level are calculated using climatological zonal mean 850-mb relative humidities for the simulated month (season). The zonal mean 850-mb relative humidities (q_{850}) are specified at Gaussian latitudes. Empirical relations are used to calculate the longwave emissivities at different levels. The following represent the emissivities, at the model five levels, used for the January simulation:

$$\varepsilon_1 = .132$$

$$\varepsilon_2 = .17 + .0075\, q_{850}(\phi),$$

$$\varepsilon_3 = .171 + .0027\, q_{850}(\phi),$$

$$\varepsilon_4 = .198 - .0042\, q_{850}(\phi),$$

$$\varepsilon_5 = .147 - .0032\, q_{850}(\phi).$$

At the surface,

$$\varepsilon_g(\phi) = .4 - .08\left(q_{850}^{(\phi)}\right)^{\frac{1}{2}}\left(1 - c_1\right),$$

where c_1 is the cloud amount taken to be = .5. The sum of effective emissivities for the model's atmosphere is given by

$$S(\phi) = .974 - .004\, q_{850}(\phi).$$

A correction factor is applied to coefficients ε_k (k = 1 to 5) so that

$$\sum_{k=1}^{5} \varepsilon_k(\phi) = S(\phi) - \varepsilon_g(\phi).$$

The net flux of longwave radiation at the earth's surface is given by:

$$L_0 = -\varepsilon_g B T_g^4 \qquad 5.11$$

where ε_g is the surface longwave emissivity. Over open ocean, the surface temperature is specified as climatological values. Over land, snow, and sea ice, the surface energy is computed assuming thermal surface-energy balance (Holloway and Manabe, 1971).

$$-\varepsilon_g B T_g^4 + S_s - Q_s - Q_e + Q_{ice} = 0 \qquad 5.12$$

The term Q_{ice} represents the heat conduction into and out of pack ice and is defined as

$$Q_{ice} = \begin{cases} c^1 l^{-1} (T_g - T_{gw}) & \text{over pack ice} \\ 0 & \text{over all other surfaces} \end{cases}, \qquad 5.13$$

where c^1 is the thermal conductivity of ice $\left(\approx 2.092\ \text{wm}^{-1}\ \text{k}^{-1}\right)$, I is the ice thickness (≈2m), and T_{gw} = 271.2°K is the temperature of sea water below the pack ice. The implicit equation (5.12) for T_g is solved by the Newton-Raphson interactive procedure (see Hanna and Stevens, 1984).

6.0 TIME DIFFERENCE METHOD

The system of primitive equations that describes the model include the fast-moving gravity waves; which imposes a certain limitation on the time step used in numerical integration to maintain computational stability if a centerd time method is used. For this reason the fast moving gravity waves are treated semi-implicitly. Assume a general prognostic equation of the form

$$\frac{\partial Z}{\partial t} = F_G(Z) + \Gamma(Z) + F_S(Z) \qquad 6.1$$

where F_G is the vertical diffusion fluxes,
F_S is linear horizontal diffusion calculated in spectral space,
Γ is all the remaining terms.

The three step time method is applied using the following equations (Williamson et al. 1987) with each identified by its "TIME" stage in accordance with the flow diagram (Figure 2).

TIME 1: $$Z^{n+1} = \bar{Z}^{n-1} + 2\Delta t F_G^{\,m}\left(Z^{*n+1}\right) \qquad 6.2$$

TIME 2: $$Z^{**n+1} = Z^{*n+1} + 2\Delta t\,\Gamma\left(\bar{Z}^{n-1}, Z^{n}, Z^{*n+1}, Z^{**n+1}\right) \qquad 6.3$$

TIME 3: $$Z^{***n+1} = Z^{**n+1} + 2\Delta t F_s\left(Z^{***n+1}\right) \qquad 6.4$$

The bar defines a time filter

$$\bar{Z}^{n} = Z^{n} + \alpha\left(Z^{n-1} - 2Z^{n} + Z^{n+1}\right) \qquad 6.5$$

where $\alpha = .06$

7.0 MODEL STRUCTURE AND PROGRAM DESCRIPTION:

The Fortran code of the model consists of about 4,000 statements that execute forty-two functions and subroutines. The code is designed to run on the VAX/VMS at RTI. However, the code is designed also to be used on the CRAY computer series. The simulation is designed for the month of January (Northern Hemisphere winter) where the climatological values of sea-surface temperature and 850-mb relative humidities are used to calculate surface fluxes and long-wave radiation emissivities needed to integrate the model. We categorize the model subroutines into four groups:

1). Preparation Subprograms;
2). Transform Subprograms;
3). Model Physics Subprograms;
4). Time Integration Subprograms

(1) PREPARATION SUBPROGRAMS

DATAG;
Initializes data that include thermodynamic constants in SI units
LGNDRE; AS; ORDLEG; GAUSSG; GAUSSV
calculate the Gaussian latitudes and weights and the associated legendre polynomial and tendencies using a rhomboidal truncation of wave number 15.

INTROROG;
Interpolates 1° latitude x 1° longitude orography into 64 x 40 grid points that describes the finite difference horizontal resolution.

INITIAL;
Reads the necessary data (sea-surface temperature and Orography, data sets) and prepares initial values to start the time integration.

AMATRX;
Calculates a matrix for solving K simultaneous equations for coefficients with given wave numbers.

(2). TRANSFORM SUBPROGRAMS

FAST; REALFT, FOUR1
Perform fast Fourier transform.

TR1;
Transforms specific variable from physical space to spectral space.

TR2;
Transforms specific variable from spectral space to grid point space.

RM1;
Calculates the Fourier components using the spectral coefficients and the Associated legendre polynomials.

RM2;
Calculates meridional derivatives using spectral coefficients and Associated legendre polynomial tendencies.

GUASS;
Calculates the spectral coefficients.

MMTRC; MTRCMX;
Perform matrix multiplication.

TR22;
Calculates the meridional derivative in grid point space using the harmonic coefficients.

(3). MODEL PHYSICS SUBPROGRAMS

RADIATION;
Calculates the longwave emissivities at the surface and the 5-level of model Atmospheres.

REGR;
Calculates second order regression coefficients of a series.

INTRPL;
Interpolates the zonal mean values at 5° latitudes into Gaussian latitudes.

EMSIT;
Uses the climatological 850-mb relative humidities to calculate emissivities at the surface and the 5-levels of the model atmosphere.

SOLAR;
Calculates surface and atmospheric solar radiation using a daily mean zenith angle.

SURFTMP;
Solves the thermal balance equation at the surface to calculate surface temperature and surface fluxes.

CONVECT;
Calculates the convective adjustment.

MADADJ;
Performs the moist convective adjustment at a column of the 5-level model.

CONVAD;
Starts the convective adjustment scheme.

CONDAD;
Adjusts temperatures and mixing ratio of supersaturated levels with stable lapse rate below and above

SMEQAD
Called by MADADJ for the moist adjustment of temperature and mxing ratio

MQADJ.
Removes negative values of mixing ratio at a grid point using horizontal and vertical borrowing method.

ESTABL;
Calculates saturation vapor pressure

(4) TIME INTEGRATION SUBPROGRAMS

T22;
Calculates explicit components of vertical temperature advection to apply the semi-implicit scheme

RNUNV;
Calculates the nonlinear dynamical terms

PREPARE;
Calculates the hydrostatic geopotential at the five levels.

VERTAD;
Calculates the vertical advection

SIGDOT;
Calculates the vertical velocities

TIME 1:
Calculates the time-split vertical diffusion

TIME 2:
Calculates the semi-implicit time scheme

TIME 3:
Calculates the horizontal diffusion

POTENG;
Calculates the global potential energy and kinetic energy of the model's atmosphere

8.0 FY1991 WORK PLAN

A 5-year simulation of the model's atmosphere will be established. The intraseasonal component will be isolated through the following operations:

1. Remove the climatological annual cycle by subtracting the 5-year mean value for each parameter.

2. Transform the filtered data, for each year, to the Fourier space and remove the seasonal cycles (first and second harmonics).

3. Additionally (to the above low-pass filter) retain only amplitudes that have 30-60 day periods.

4. Transform the truncated series to the physical space.

Besides analyzing the differences in the intraseasonal variability between the different case studies (for example different sea-surface temperature patterns), we are interested in investigating the detailed relation between the thermal and dynamical patterns within each case. Excitation of the intraseasonal mode during El Nino episodes has been confirmed by many diagnostic studies using satellite data (e.g. Hanna and Crissman, 1991). The thermal heating in the model's tropospheric column is a composite of the contributions of latent heat released during condensation of water vapor, radiational heating and the surface energy fluxes. At the same time, the tropical upper level divergence is, in part, a dynamical consequence to such thermal forcing. The model simulations will provide a continuous and comprehensive (in time and space) presentation of the thermal and dynamical fields. It is then possible to investigate, for example, how the upper level divergence

correlates with the tropospheric heating pattern within an intraseasonal time scale, and what are the spatial characteristics of the phase and amplitude of each parameter.

The interaction of the intraseasonal oscillation with the local circulation and its effect on the medium and long-range weather forecast is not clear. To gain more insight into this problem, it is important to identify the development of the large-scale circulation associated with the low-frequency oscillation. The time filtering procedure described above will be used to extract the variability related to the low frequency oscillation of the temperature and geopotential height fields at the upper and lower levels of the model's atmosphere. The Empirical Orthogonal Function (EOF) analysis of the filtered fields will be applied for tropical and midlatitude zones. The eigen modes and eigen coefficients will be used to study the amplitude and phase of the time series. A reconstructed time series with the first few eigen modes can be compared with the monthly or seasonal statistics of a particular field. For example, Chen (1987) has used the EOF analyses to show that the first eigen mode of the filtered 200-mb temperatures is essential to form the warm center over the Tibet-India region and the cold center over the North Pacific during the Northern Hemisphere summer (1979). The low order eigen modes explain the largest variances of the time series. In this sense, if the reconstructed series using the first few eigen modes did not resemble the variance revealed by the infiltered time series that will lead to the conclusion that the variability at this time scale is not significant component of the large scale circulation.

The modelling analyses will be linked and compared to analyses derived from satellite data such as the ISCCP-C1 data. Studies have identified the intraseasonal oscillation in the tropical OLR data, (Lau and Chan, 1985) and IR cloud temperature (Hanna and Crissman 1991).

9.0 REFERENCES

Bourke, W., 1974: A multilevel spectral model. I. formulation and hemispheric integrations. *Mon. Wea. Rev.*, 102, pp. 687-701.

Chen, T. C., 1987: 30-50 day oscillation of 200-mb temperature and 850-mb height during the 1979 northern summer. *Monthly Weather Review*.

Corby, G. A., A. Gilchrist, and P. R. Rowntree, 1977: United Kingdom Meteorological Office five-level general circulation model. *Methods Comput. Phys.*, 17, pp. 67-110.

Gates, W. L., 1975: The January global climate simulated by a two-level general circulation model: A comparison with observations. *J. Atmos. Sci.*, 32, pp. 449-477.

Haltiner, G. J., and R. T. Williams, 1980: Numerical prediction and dynamic meteorology. John Wiley & Sons, Inc., 477 pp.

Hanna, A. F., and B. W. Crissman, 1991: Subseasonal variability of the cloud pattern over the tropical Pacific during the summer of 1983. 19th Conference on Hurricane and Tropical Meteorology.

Hanna, A. F., and D. E. Stevens, 1984: A global low-order spectral model designed for climate sensitivity studies. Atmospheric Science Paper No. 378, Colorado State University, Fort Collins, CO, 41 pp.

Hanna, A. F., D. E. Stevens, and E. R. Reiter, 1984: Short-term climatic fluctuations forced by thermal anomalies. *J. Atmos. Sci.*, 41, pp. 122-141.

Holloway, J. L., Jr., and S. Manabe, 1971: Simulation of climate by a global general circulation model. *Mon. Wea. Rev.* 99, 335-370.

Lau, K. M., and P. H. Chan, 1985: Aspects of the 40-50 day oscillation during the northern winter as inferred from outgoing longwave radiation. *Mon.Wea. Rev.*, 113, pp. 1889-1909.

Manabe, S., J. Smagorinsky, and R. F. Sticker, 1965: Simulated climatology of a general circulation model with a hydrologic cycle. *Mon. Wea. Rev.*, 93, pp. 769-798.

Royer, J. F., 1986: Correction of negative mixing ratios in spectral models by global horizontal borrowing. *Mon. Wea. Rev.*, 114, pp. 1408-1410.

Wetherald, R. T., and S. Manabe, 1972: Response of the joint ocean-atmosphere model to the seasonal variation of solar radiation. *Mon. Wea. Rev.*, 100, pp. 42-59.

Williamson, D. L., J. T. Kiehl, V. Ramanathan, R. Dickinson, and J. Hack, 1987: Description of NCAR Community Climate Model (CCMI): NCAR TN-285+STR, 112 pp.

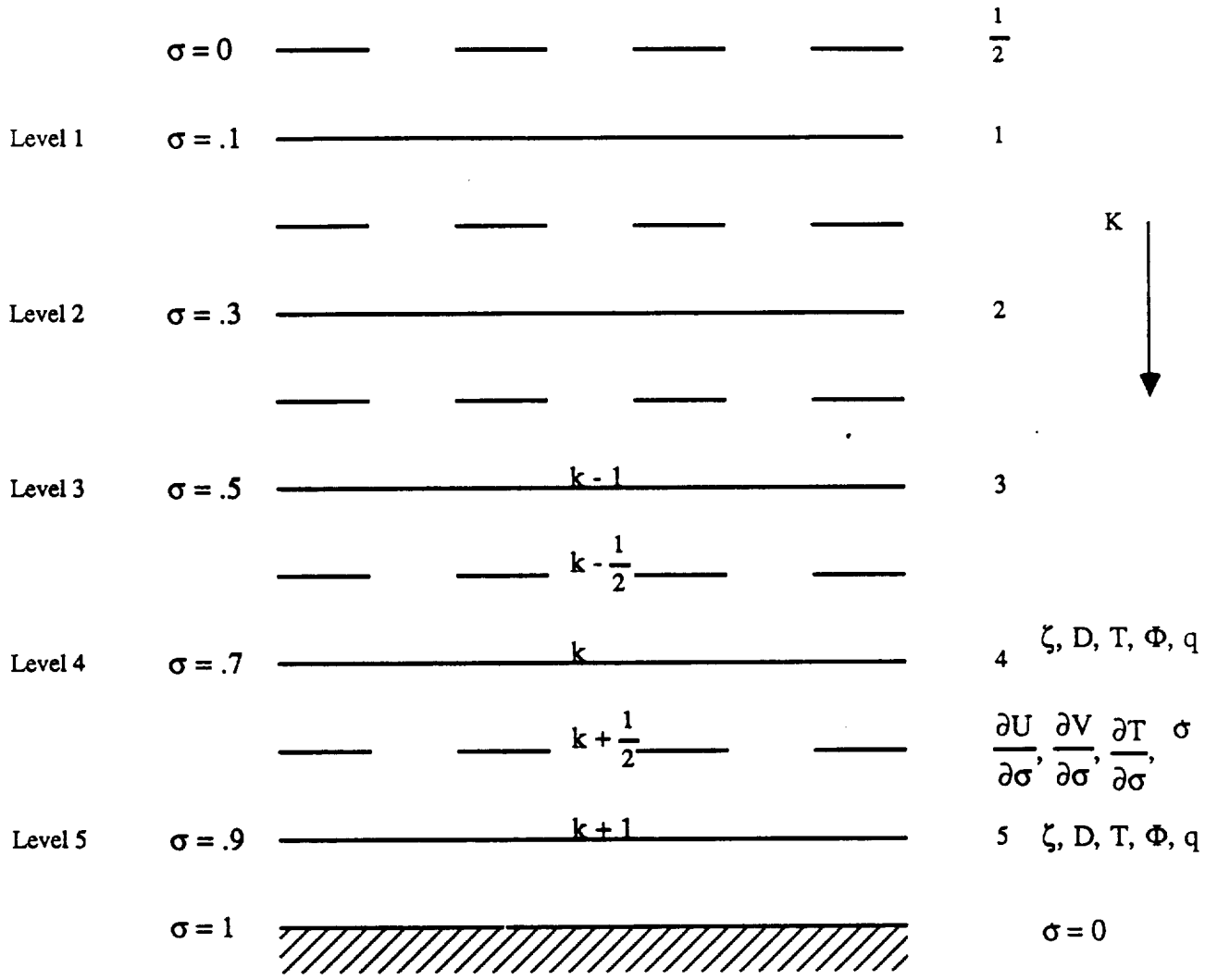

Figure 1: . Schematic representation of the vertical structure of the 5-level atmospheric model ($\zeta = \nabla^2 \psi$, and $D = \nabla^2 \chi$). Half levels are represented by dashed lines.

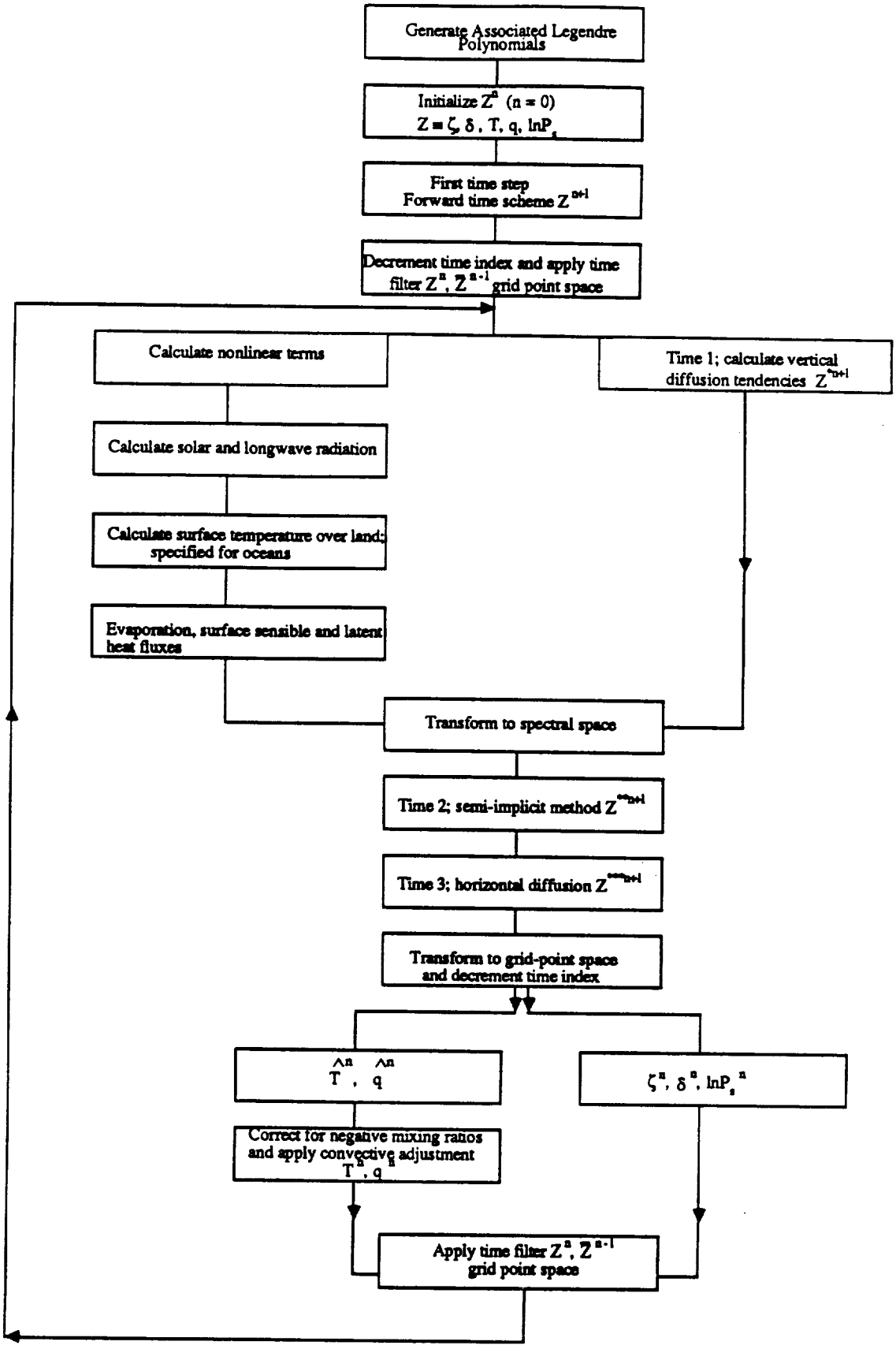

Figure 2: A schematic representation of the sequence of operations for implementing one time step of the model.